

**Effects of Surface Charge Density of Membranes on the Irreversible
Electroporation Induced Rate Constant of Pore Formation of Vesicles**

by

Urbi Shyamolima Orchi

MASTER OF SCIENCE IN PHYSICS


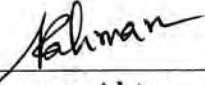


Department of Physics

BANGLADESH UNIVERSITY OF ENGINEERING AND TECHNOLOGY

June, 2021

The thesis titled “Effects of Surface Charge Density of Membranes on the Irreversible Electroporation Induced Rate Constant of Pore Formation of Vesicles” Submitted by Urbi Shyamolima Orchi, Roll No. 1018142513F, Session: October/2018, has been accepted as satisfactory in partial fulfillment of the requirement for the degree of MASTER OF SCIENCE IN PHYSICS on 19 June, 2021.

BOARD OF EXAMINERS

- 
1. **Dr. Mohammad Abu Sayem Karal** Chairman
(Supervisor)
Associate Professor
Department of Physics, BUET, Dhaka-1000
- 
2. **Dr. Md. Rafi Uddin** Member
Professor and Head (Ex-officio)
Department of Physics, BUET, Dhaka-1000
- 
3. **Dr. Nasreen Akter** Member
Professor
Department of Physics, BUET, Dhaka-1000
- 
4. **Dr. Muhammad Rakibul Islam** Member
Associate Professor
Department of Physics, BUET, Dhaka-1000
- 
5. **Dr. Alamgir Kabir** Member
Associate Professor (External)
Department of Physics
University of Dhaka, Dhaka-1000

CANDIDATE'S DECLARATION

It is hereby declared that this thesis or any part of it has not been submitted elsewhere for the award of any degree or diploma.

Urbi Shyamolima

Urbi Shyamolima Orchi

***DEDICATED TO MY BELOVED
PARENTS AND TEACHERS***

Acknowledgements

I would like to take this opportunity to thank everyone who made this work possible.

First of all, I would like to convey my utmost appreciation to my supervisor Dr. Mohammad Abu Sayem Karal, Associate Professor, Department of Physics, Bangladesh University of Engineering and Technology (BUET), Dhaka for choosing me to be a part of his multidisciplinary research group and giving me this great chance to research furthermore. For the past two years, his constant encouragement inspired me to be a better researcher and hard working person. It was a great experience to be a part of his research team.

It is my great honor to convey my gratitude to Professor Dr. Md. Rafi Uddin, Head, Department of Physics, BUET for his great support to move through the academic course during this degree program. I would like to express my profound appreciation to Professor Dr. Jiban Podder, Professor Dr. Md. Feroz Alam Khan, Professor Dr. A. K. M. Akther Hossain, Professor Dr. Md. Mostak Hossain, Professor Dr. Afia Begum, Professor Dr. Md. Forhad Mina, Professor Dr. Nasreen Akter, and Professor Dr. Mohammed Abdul Basith for their considerate suggestions in my research proposal which was submitted in CASR, BUET. I am thankful to all other respected teachers of the Department of Physics for their kind co-operation.

I wish to acknowledge Md. Towhiduzzaman, Md. Kabir Ahmed, Marzuk Ahmed, Shareef Ahammed, Nadia Akter Mokta, Taufika Nasrin, Sabrina Sharmin and Malay Kumar Sarkar for their continuous encouragement in Biophysics Research Laboratory, Department of Physics, BUET.

I am also thankful to the authority of Department of Physics, BUET for providing me the logistic supports for this thesis work. Sincere acknowledgement to the CASR, BUET for granting funds to carry out this research. Great appreciation to the Ministry of Science and Technology of Bangladesh for providing me the National Science and Technology Fellowship (NST) for the year 2019-2020 to accomplish the research effortlessly.

Finally, I would like to express my appreciation to my beloved parents and family members who always supported me and encouraged me in my work and inspired me to do my best.

Urbi Shyamolima Orchi

Abstract

In this study, the effects of surface charge density of membranes on the irreversible electroporation (IRE)-induced rate constant of pore formation in the membranes of giant unilamellar vesicles (GUVs) was investigated. GUVs were synthesized by a mixture of anionic lipid dioleoylphosphatidylglycerol (DOPG) and neutral lipid dioleoylphosphatidylcholine (DOPC) in a physiological buffer (10 mM PIPES, pH 7.0, 150 mM NaCl and 1 mM EGTA) using the natural swelling method. The IRE signal (pulsating direct current) of frequency 1.1 kHz was applied through the gold coated electrode system. By changing the DOPG mole fraction X of values 0.10, 0.20, 0.40 and 0.60, the corresponding surface charge densities of membranes were determined. For all values of X , the rate constant increased with the increase of constant electric tension due to IRE signal. The rate constant found higher at lower tension due to the increase of X . From the fitting of tension-dependent rate constant data, the line tensions were found 10.1 ± 0.1 , 11.2 ± 0.3 , 12.1 ± 0.1 and 13.1 ± 0.3 pN for $X = 0.10, 0.20, 0.40$ and 0.60 , respectively. The influence of X on the critical tension of electroporation in GUVs was also investigated. The critical tension decreased from 9.0 ± 0.3 to 6.0 ± 0.2 mN/m with the increase of X from 0 to 0.60 in GUVs. The theoretical equation was fitted to the X dependent normalized critical tension and the binding constant of lipid-ion interaction was obtained 0.75 M^{-1} . The decreased in energy barrier for the formation of a prepore, due to the increased of X , was the main factor explaining the decreased of critical tension and increased of rate constant of pore formation in GUVs.

Contents

Abstract	vi
Contents	vii
List of Figures	x
List of Tables	xvii
List of Abbreviations	xix
CHAPTER 1: INTRODUCTION	1
1.1 Preface	1
1.2 Objective of the Study	5
1.3 Outline of the Thesis	5
CHAPTER 2: LITERATURE REVIEW AND THEORETICAL ASPECTS	6
2.1 Literature Review	6
2.2 Cell Membrane Physiology	14
2.3 Lipid and Lipid Bilayer Structure	16
2.4 Model Membrane	18
2.5 Vesicles	19
2.6 Vesicles and its Classification	20
2.7 Phospholipids	21
2.8 Membrane Electrical Model and Equation	22
2.8.1 The mechanism of charges of surfaces in liquid	22
2.8.2 Charged surfaces in water without added electrolyte	23
2.8.3 The Poisson-Boltzmann (PB) equation	24
2.8.4 Charged surface in electrolyte solution	25
2.8.5 The Grahame equation	27
2.8.6 Surface charge of isolated surfaces	27

2.8.7 Debye length	28
CHAPTER 3: MATERIALS AND METHODS	
3.1 Chemicals and Regents	29
3.2 Synthesis of Lipid Membranes of GUVs	30
3.3 Preperation of Sample	31
3.4 Purification Method of Lipid Membrane	32
3.5 Observations of Lipid Membrane of GUVs	34
3.5.1 Suspension of GUVs in microchamber	34
3.5.2 Microscopy	34
3.6 Description of the IRE Technique	35
CHAPTER 4: RESULTS AND DISCUSSION	
4.1 Pore Formation in 20%DOPG/80%DOPC-GUVs at 5.75 mN/m	38
4.2 Probability of Pore Formation in 20%DOPG/80%DOPC-GUVs at 5.75 mN/m	39
4.3 Rate Constant Pore Formation in 20%DOPG/80%DOPC-GUVs at 5.75 mN/m	41
4.4 Pore Formation in 20%DOPG/80%DOPC-GUVs at 6.5 mN/m	42
4.5 Probability of Pore Formation in 20%DOPG/80%DOPC-GUVs at 6.5 mN/m	43
4.6 Rate Constant Pore Formation in 20%DOPG/80%DOPC-GUVs at 6.5 mN/m	45
4.7 Pore Formation in 20%DOPG/80%DOPC-GUVs at 7.25 mN/m	46
4.8 Probability of Pore Formation in 20%DOPG/80%DOPC-GUVs at 7.25 mN/m	47
4.9 Rate Constant Pore Formation in 20%DOPG/80%DOPC-GUVs at 7.25 mN/m	48
4.10 Theoretical Aspect of the Probability of Pore Formation and the Rate Constant of Pore Formation	49
4.11 Dependence of $P_{\text{pore}}(60 \text{ s})$ on σ_c for 20%DOPG/80%DOPC-GUVs	50
4.12 Dependence of Rate Constant of Pore Formation on σ_c for 20%DOPG/80%DOPC-GUVs	51

4.13 Pore Formation in 60%DOPG/40%DOPC-GUVs at 4.5 mN/m	53
4.14 Probability of Pore Formation in 60%DOPG/40%DOPC-GUVs at 4.5 mN/m	54
4.15 Rate Constant Pore Formation in 60%DOPG/40%DOPC-GUVs at 4.5 mN/m	56
4.16 Pore Formation in 60%DOPG/40%DOPC-GUVs at 5.5 mN/m	57
4.17 Probability of Pore Formation in 60%DOPG/40%DOPC-GUVs at 5.5 mN/m	58
4.18 Rate Constant Pore Formation in 60%DOPG/40%DOPC-GUVs at 5.5 mN/m	59
4.19 Pore Formation in 60%DOPG/40%DOPC-GUVs at 6.0 mN/m	60
4.20 Probability of Pore Formation in 60%DOPG/40%DOPC-GUVs at 6.0 mN/m	61
4.21 Rate Constant Pore Formation in 60%DOPG/40%DOPC-GUVs at 6.0 mN/m	62
4.22 Dependence of $P_{\text{pore}}(60 \text{ s})$ on σ_c for 60%DOPG/40%DOPC-GUVs	63
4.23 Dependence of Rate Constant of Pore Formation on σ_c for 60%DOPG/40%DOPC-GUVs	64
4.24 Dependence of $P_{\text{pore}}(60 \text{ s})$ on σ_c at Various DOPG/DOPC- GUVs	65
4.25 Dependence of Rate Constant on σ_c for Various Surface Charge Density	66
4.26 Determination of Critical Tension by Changing Mole Fraction and Its Theoretical Aspects	68
4.27 Theoretical Aspect of Critical Tension	72
CHAPTER 5: CONCLUSIONS	
Conclusions	76
References	80
Appendix	91

List of Figures

Fig. 2.1 Lipid membrane behavior with DC electric field through IRE (i) Bursting of charged (POPC:POPG , 1:1) vesicles subjected to electric pulses. The time after the beginning of the pulse is marked on each image (ii) Vesicle deformation to DC pulses in the presence and absence of salt and gold particles. The direction of the field is indicated by the arrow on the left and the scale bar corresponds to 15 μm . 6

Fig. 2.2 Treatment planning and surgical protocol for irreversible electroporation ablation in the pig liver. IRE pulse parameters are bipolar electroporation, 2.5 kV pulses applied in a train of eight 100 microsecond pulses separated by 100 milliseconds. Four electrodes 18 gage stainless steel electrodes, 1.5 cm distance between probes. (A) Results of mathematical analysis showing constant electrical field magnitude isolines during the application on an electroporation pulse between two electrodes. The numbers on the figures indicate the magnitude of the electrical field in increments of 100 V/cm starting from 100 V/cm (outer isoline). The power delivered during each pulse is 1.2 J per cm depth of electrode. (B) Results of mathematical analysis show constant electrical field magnitude isolines due to the superposition of the application of the IRE pulses between the four pairs of IRE electrodes. The numbers on the figures indicate the magnitude of the electrical field in increments of 100 V/cm starting from 600 V/cm (outer isoline). Experiments have shown that 600 V/cm induces irreversible electroporation in liver. (C) Photograph of application of electroporation probes with ultrasound, (D) insertion of a set of four electrodes. 7

Fig. 2.3 Determination of appropriate electrical parameters for an effective tumor treatment by IRE – experiments with immunocompetent mice. Panels are identified by letters corresponding to the parameters, except for panel A (tumor growth in untreated mice followed as controls of treatment conditions B and C), panel D (control of E and F), panel G (control of H and I) and panel J (control of K and L). 8

Fig. 2.4 Degree of deformation (a/b) induced on one vesicle when applying different square-wave pulses: (A) 1 kV/cm, (B) 2 kV/cm, and (C) 3 kV/cm. For each pulse strength, the applied pulses were of duration $t_p = 50$ ms (\square), 100 ms (\blacksquare), 150 ms (\triangle), 200 ms (\circ), 250 ms (\bullet), and 300 ms (\star). The image acquisition rate was 30,000 fps. Time $t = 0$ was set as the beginning of the pulse. The insets show the maximum value of the deformation (a/b) max as a function of pulse duration, t_p , for each pulse strength.

Arrows indicate the tense-free poration limit ($V_p > V_c$). The time interval between applying consecutive pulses was generally 5 min. The images on each graph correspond to the maximal elongation for the pulse of duration $t_p = 150$ ms. The scale bar indicates 15 μ m. The electrode's polarity is indicated with a plus and a minus sign on the second snapshot. 9

Fig. 2.5 Measured critical stresses for anionic vesicles in 1 mM electrolyte. Triangles, diamonds, and squares correspond to POPG/POPC in TMA-Cl, POPG/POPC in KCl, and POPA/POPC in KCl, respectively. 10

Fig. 2.6 Tension dependence of k_p for GUVs of DOPG and DOPC mixture for different values of fraction X of DOPG and different salt concentrations C . Average values and standard errors of k_p for each tension were determined for three independent experiments using 20 GUVs for each experiment. The solid lines show the best-fit theoretical curves with $D_r = 165$ nm^2/s and $a = 0.45$. (a) Effect of salt concentration at constant X ($= 0.40$). $C = 12$ mM (\circ), 162 mM (\bullet), and 312 mM (\square). The curves are shown for $C = 162$ mM ($\Gamma = 11.4$ pN), and 312 mM ($\Gamma = 10.5$ pN). (b) Effect of surface charge density at constant C ($= 162$ mM). 100% DOPC (\blacksquare), 10% DOPG/90% DOPC (\square), 40% DOPG/60% DOPC (\bullet), and 70% DOPG/30% DOPC (\circ). The best-fit curves are shown for $X = 0$ ($\Gamma = 10.5$ pN), 0.10 ($\Gamma = 10.4$ pN), and 0.40 ($\Gamma = 11.4$ pN). The data for 100% DOPC GUVs and 40% DOPG/60% DOPC at $C = 162$ mM. 11

Fig. 2.7 Effect of constant tension on pore formation in single GUVs. (A) Time course of the fraction of intact 40% DOPG/60% DOPC GUVs without rupture among all of the examined GUVs, $P_{\text{intact}}(t)$, in the presence of tension. σ : (\circ) 5.0, (\square) 7.0 mN/m. The number of examined single GUVs was 20 in each experiment. (B) Dependence of k_p on tension. (\blacksquare) 40% DOPG/60% DOPC-GUV and (\square) DOPC-GUV. Average values and the standard error in k_p for each tension were determined among three independent experiments using 20 GUVs for 40% DOPG/60% DOPC membranes and 16–20 GUVs for DOPC membranes for each experiment. Scale bars show standard errors. The solid lines show the best fits in accordance with the theoretical curves corresponding to eq 2.20 using $\Gamma = 7.0$ pN and $D_r = 1.2$ nm^2/s for 40% DOPG/60% DOPC-GUV and $\Gamma = 10.5$ pN and $D_r = 165$ nm^2/s for DOPC-GUV. (C) Dependence of P_{pore} (360 s) in 40% DOPG/60% DOPC-GUV on tension. Scale bars show standard errors. 12

Fig. 2.8 Tension-dependent average k_p for 40%DOPG/60%DOPC-GUVs (square) and 10%DOPG/90%DOPC-GUVs (circle). The solid line shows the best-fitting theoretical curve corresponding to with $A_F = 1.9 \times 10^8 \text{ m}^2\text{s}^{-1}\text{J}^{-1}$ and $\Gamma = 12.1 \text{ pN}$ for 40%DOPG/60%DOPC-GUVs and $A_F = 4.2 \times 10^6 \text{ m}^2\text{s}^{-1}\text{J}^{-1}$ and $\Gamma = 10.1 \text{ pN}$ for 10%DOPG/90%DOPC-GUVs. 13

Fig. 2.9 A detailed diagram of the cell membrane. 14

Fig. 2.10 The parts of a phospholipid molecule. This example is phosphatidylcholine, represented (A) schematically, (B) by a formula, (C) as a space-filling model, and (D) as a symbol. 16

Fig. 2.11 packing arrangement of lipid molecules in water environment (A) Wedge shaped lipid molecules form micelles (above) whereas cylinder shaped lipid molecules (below) form bilayers (B) a lipid micelle and lipid bilayer seen in cross section. 17

Fig. 2.12 Model membrane representing the same complexity as a mimic of bio membrane. 19

Fig. 2.13 Vesicle (i) multilamellar (ii) Unilamellar 20

Fig. 2.14 Different types of vesicles. 21

Fig. 2.15 Schematic diagram of lipid bilayer. 22

Fig. 2.16 Ions bound to a surface are not rigidly bound but can exchange with other ions in solution; their lifetime on a surface can be as short as 10^{-9} s (1 ns) or as long as many hours. 23

Fig. 2.17 Two negatively charged surfaces of surface charge density σ separated a distance D in water. The only ions in the space between them are the counterions that have dissociated from the surfaces. The counterion density profile ρ_x and electrostatic potential ψ_x are shown schematically in the lower part of the figure. The “contact” values are ρ_s , ψ_s and $E_S = -(d\psi/dx)_s$. 25

Fig. 2.18 Near a negatively charged surface there is a growth of counterions (ions of contrasting charge to the surface coions) and a reduction of coions, shown graphically here for a 1:1 electrolyte, where ρ_∞ is the electrolyte concentration in the bulk or “reservoir” at $x = \infty$. Counterions can adsorb to the surface in the dehydrated, partially hydrated, or fully hydrated state. The OHP is the plane beyond which the ions obey the

Poisson-Boltzmann equation. This plane is usually farther out than the van der Waals plane.	26
Fig. 3.1 Block diagram (a) and schematic diagram (b) showing steps of natural swelling method.	31
Fig. 3.2 Set-up of membrane filtering method.	33
Fig. 3.3 (a) Phase Contrast image and (b) Fluorescence GUVs Images.	34
Fig. 3.4 Block diagram of IRE technique.	35
Fig. 3.5 Schematic diagram of gold coated electrode system for IRE (a) and Slots of gold coated electrode system for IRE (b).	35
Fig. 3.6 Experimental design for the formation of pores in GUVs in IRE technique. (A) An application of E induces a modification of the transmembrane potential of GUVs. The IRE signal is shown in the inset. (B) A single intact GUV, (C) Ruptured GUV. White bar in (B, C) corresponds to a length of 15 μm .	37
Fig. 4.1 Pore formation of (a) 1 st (b) 2 nd (c) 3 rd (d) 4 th and (e) 5 th single 20%DOPG/60%DOPC- GUVs at 5.75 mN/m. The scale bar corresponds to a length of 16 μm .	38
Fig. 4.2 Stochastic pore formation for 20%DOPG/80%DOPC- GUVs at 5.75 mN/m for (a) 1 st independent experiment and (b) 2 nd independent experiment.	41
Fig. 4.3 The time course of P_{intact} for 20%DOPG/80%DOPC-GUVs at 5.75 mN/m for (a) 1 st independent experiment (b) 2 nd independent experiment. The solid line in (a) and (b) is the theoretical fitting equation (4.1).	42
Fig. 4.4 Pore formation of (a) 1 st (b) 2 nd (c) 3 rd (d) 4 th and (e) 5 th single 20%DOPG/80%DOPC-GUVs at 6.5 mN/m. The scale bar corresponds to a length of 15 μm .	43
Fig. 4.5 Stochastic pore formation for 20%DOPG/80%DOPC-GUVs at 6.5 mN/m for (a) 1 st independent experiment and (b) 2 nd independent experiment.	44
Fig. 4.6 The time course of P_{intact} for 20%DOPG/80%DOPC-GUVs at 6.5 mN/m for (a) 1 st independent experiment (b) 2 nd independent experiment. The solid line in (a) and (b) is the theoretical fitting equation (4.1).	44

Fig. 4.7 Pore formation of (a) 1st (b) 2nd (c) 3rd (d) 4th and (e) 5th single 20%DOPG/80%DOPC-GUVs at 7.25 mN/m. Here, the scale bar corresponds to a length of 15 μm . 45

Fig. 4.8 Stochastic pore formation for 20%DOPG/80%DOPC-GUVs at 7.25 mN/m for (a) 1st independent experiment and (b) 2nd independent experiment. 48

Fig. 4.9 The time course of P_{intact} at 7.25 mN/m for (a) 1st independent experiment (b) 2nd independent experiment. The solid line in (a) and (b) is the theoretical fitting equation (4.1). 48

Fig. 4.10 The fitted curve for P_{pore} and σ_c at 20%DOPG/80%DOPC for $C = 162$ mM. The solid lines show the best fitted theoretical curves corresponding to equation (4.6) with k_p as used in Fig. 4.11 according to equation (4.5). 51

Fig. 4.11 The tension dependent k_p for 20%DOPG/80%DOPC-GUVs. The solid lines show the best fitted theoretical curves corresponding to equation (4.5). 52

Fig. 4.12 Pore formation of (a) 1st (b) 2nd (c) 3rd (d) 4th and (e) 5th single 60%DOPG/40%DOPC-GUVs at 4.5 mN/m. Here, the scale bar corresponds to a length of 15 μm . 53

Fig. 4.13 Stochastic pore formation for 60%DOPG/40%DOPC-GUVs at 4.5 mN/m for (a) 1st independent experiment and (b) 2nd independent experiment. 56

Fig. 4.14 The time course of P_{intact} for 60%DOPG/40%DOPC-GUVs at 4.5 mN/m for (a) 1st independent experiment (b) 2nd independent experiment. The solid line in (a) and (b) is the theoretical fitting equation (4.1). 56

Fig. 4.15 Pore formation of (a) 1st (b) 2nd (c) 3rd (d) 4th and (e) 5th single 60%DOPG/40%DOPC -GUVs at at 5.5 mN/m. Here, the scale bar corresponds to a length of 15 μm . 57

Fig. 4.16 Stochastic pore formation in 60%DOPG/40%DOPC-GUVs at 5.5 mN/m for (a) 1st independent experiment and (b) 2nd independent experiment. 59

Fig. 4.17 The time course of P_{intact} in 60%DOPG/40%DOPC-GUVs at 5.5 mN/m for (a) 1st independent experiment (b) 2nd independent experiment. The solid line in (a) and (b) is the theoretical fitting equation (4.1). 59

Fig. 4.18 Pore formation of (a) 1st (b) 2nd (c) 3rd (d) 4th and (e) 5th single 60%DOPG/40%DOPC-GUVs at 6.0 mN/m. Here, the scale bar corresponds to a length of 15 μm . 60

Fig. 4.19 Stochastic pore formation for 60%DOPG/40%DOPC-GUVs at 6.0 mN/m for (a) 1st independent experiment and (b) 2nd independent experiment. 62

Fig. 4.20 The time course of P_{intact} at 6.0 mN/m for (a) 1st independent experiment (b) 2nd independent experiment. The solid line in (a) and (b) is the theoretical fitting equation (4.1). 62

Fig. 4.21 The fitted curve of P_{pore} and σ_c for 60%DOPG/40%DOPC-GUVs. The solid lines show the best fitted theoretical curves corresponding to equation (4.6) with k_p as used in Fig. 4.22 according to equation (4.5). 64

Fig. 4.22 The tension dependent k_p for 60%DOPG/40%DOPC-GUVs. The solid lines show the best fitted theoretical curves corresponding to equation (4.5). 65

Fig. 4.23 Dependence of P_{pore} (60 s) on σ_c for various surface charge density for $X = 0.60$ (Δ), 0.40 (\square), 0.20 (\diamond) and 0.10 (\circ) at $C = 162$ mM. The average values and standard deviations of the P_{pore} (60 s) are obtained using 3 independent experiments, each with 15-24 GUVs, for each value of σ_c . The solid lines show the best fitted theoretical curves corresponding to equation (4.6) with k_p as used in Fig. 4.24 according to equation (4.5). 66

Fig. 4.24 The tension dependent k_p for different surface charge densities. The σ_c dependent k_p for $X = 0.60$ (Δ), 0.40 (\square), 0.20 (\diamond) and 0.10 (\circ) at $C = 162$ mM. Average values and standard deviations of k_p for each tension are determined for 3 independent experiments, each with 18-24 GUVs, for each value of σ_c . The solid lines show the best fitted theoretical curves corresponding to equation (4.5). 67

Fig. 4.25 Phase contrast images of pore formation in a ‘single GUV’, the time of pore/without pore formation of several single GUVs and the dependence of probability of pore formation in GUVs on σ_c at different X . (a) Phase contrast images of pore formation of a ‘single 40%DOPG/60%DOPC-GUV’ using $\sigma_c = 5$ mN/m. The field direction is shown with an arrow in the left side. The numbers above in each image show the time in seconds after the application of σ_c due to E . White bar corresponds to the length of 15 μm . (b) Dependence of P_{pore} (60 s) on σ_c for $X = 0.60$ (Δ), 0.40 (\square), 0.20

(\diamond), 0.10 (\circ) and 0.0 (∇) at $C = 162$ mM. The average values and standard deviations of P_{pore} (60 s) are obtained using 3 independent experiments, each with 15-24 GUVs, for each value of σ_c . 69

Fig. 4.26 The X dependence (a) bar chart of the critical tension of electroporation and (b) the normalized critical tension of electroporation in GUVs. The solid red line of (b) shows the best fitting theoretical curve of equation (4.12) to the experimental data. 71

Fig. 4.27 Prepore free energy profile (Eq. 9) for different values of X using $\sigma_c = 7.5$ mN/m and $\Gamma = 11.2$ pN. 75

List of Tables

Table. 4.1 Time of pore formation for several 20%DOPG/80%DOPC-GUVs at tension 5.75 mN/m for two independent experiments.	40
Table. 4.2 Rate constant of two independent experiment for 20%DOPG/80%DOPC-GUVs at tension 5.75 mN/m.	42
Table. 4.3 Time of pore formation for several 20%DOPG/80%DOPC-GUVs at tension 6.5 mN/m for two independent experiments.	44
Table. 4.4 Rate constant of two independent experiments at tension 6.5 mN/m for 20%DOPG/80%DOPC-GUVs.	46
Table. 4.5 Time of pore formation for several 20%DOPG/80%DOPC-GUVs at tension 7.25 mN/m for two independent experiments.	47
Table. 4.6 Rate constant of two independent experiments at tension 7.25 mN/m for 20%DOPG/80%DOPC-GUVs.	49
Table. 4.7 The dependence of P_{pore} on σ_c using $X = 0.20$.	51
Table. 4.8 The σ_c dependent k_p values using $X = 0.20$.	52
Table. 4.9 Time of pore formation for several 60%DOPG/40%DOPC-GUVs at tension 4.5 mN/m for two independent experiments.	55
Table. 4.10 Rate constant of two independent experiments at tension 4.5 mN/m for 60%DOPG/40%DOPC-GUVs.	57
Table. 4.11 Time of pore formation for several 60%DOPG/40%DOPC-GUVs at tension 5.5 mN/m for two independent experiments.	58
Table. 4.12 Rate constant of two independent experiments at tension 5.5 mN/m for 60%DOPG/40%DOPC-GUVs.	60
Table. 4.13 Time of pore formation for several 60%DOPG/40%DOPC-GUVs at tension 6.0 mN/m for two independent experiments.	61
Table. 4.14 The value of rate constant for two independent experiments at tension 6.0 mN/m for 60%DOPG/40%DOPC-GUVs.	63
Table. 4.15 The dependence of P_{pore} on σ_c using $X = 0.60$.	63

Table. 4.16 The σ_c dependent k_p values using $X = 0.60$	64
Table. 4.17 Surface charge dependent average k_p at various σ_c	67
Table. 4.18 Surface charge dependent average Γ .	68
Table. 4.19 The dependence of P_{pore} on σ_c using $X = 0.40$	70
Table. 4.20 The critical tensions for various surface charge density.	71

List of Symbols and Abbreviation

MD	-	Molecular Dynamics
IRE	-	Irreversible Electroporation
GUV	-	Giant Unilamellar Vesicle
MOSFET	-	Metal Oxide Semiconductor Field Effect Transistor
DOPC	-	1,2-dioleoyl- <i>sn</i> -glycero-3-phosphocholine
DOPG	-	1,2-dioleoyl- <i>sn</i> -glycero-3-phospho-(1- <i>rac</i> -glycerol)
EGTA	-	Ethyleneglycol- <i>N,N,N',N'</i> -tetraacetic Acid
BSA	-	Bovine Serum Albumin
PIPES	-	1,4-Piperazinediethanesulfonic Acid
DNA	-	Deoxyribonucleic Acid
RNA	-	Ribonucleic Acid
UI	-	User Interface
PU	-	Power Unit
ATP	-	Adenosine Triphosphate

CHAPTER: 1

INTRODUCTION

1.1 Preface

Surface charge density of the membranes of cells/vesicles plays important role in numerous biophysical and biochemical phenomena, for example, the binding of proteins to cell membranes, structural alterations of membranes and membrane strength [1-3]. Irreversible electroporation (IRE) is a promising method for the cancel cells and tissue ablation. IRE appeals much consideration to the researchers because this method contains localized disruption of cells/vesicles membranes by short, high-frequency electric pulses, and has been used in the past for cancel cell, tissue ablation, and treatment for specific diseases [4-5]. Furthermore, the IRE can be used for non-thermal food and water preservation, essentially causing permanent destruction of microorganism [6-7].

Currently, lipid membranes of giant unilamellar vesicles (GUVs) of size 10 μm or more have been used as a model cell membrane for investigating the formation of pores in the membranes using mechanical tension [8-9], electrical tension [10-12], nanoparticles [13] and peptides [14-15]. GUVs have been used for studying the formation of pores in the membranes since the static and dynamic nature of vesicles can be detected using optical microscope [14-15]. The size distribution of self-assembled vesicles and the molecular transport through the nano-pores have also been studied using GUVs [12, 13, 15].

So, the study on pore formation in the membranes of vesicles using electroporation technique is rapidly growing by advantage of its possible applications in biology, biotechnology and medicine [16-17]. The pore formation in vesicles under applied lateral tension or electrical stress has been described by a theoretical model. The waiting time of pore formation follows a nonmonotonous function of lateral tension whereas the waiting time decreases monotonously under electrical stress [18]. In case of molecular dynamics (MD) simulations, there exists a linear dependency of the activation energy for the formation of pores under applied electric field [19]. Besides, the electropore life cycle describes the pore initiation, construction and resealing. For instance, the pore annihilation time is much longer than the pore creation time [20].

Meanwhile, MD simulations show the formation of water channels across the membranes in the presence of applied electric field, which suggest the evidence of lateral stress due to the electric field [21]. The metastability of hydrophilic pore owing to compensating positive and negative curvature effects at the pore edge has been investigated by MD simulations as well [22]. Furthermore, the constant-current measurements of planar membrane exhibit the constant-intensity current flow through the bilayer membranes generated fluctuating pores in their structure [23].

Therefore, it has been considered that electric field pulses induce lateral tension for the formation of pores in the membranes of vesicles [10, 24-25]. The lateral tension induces a prepore of radius, r , in the membranes [26-27]. If $r < r_c$ (r_c is critical radius), prepore closes quickly, and if $r \geq r_c$, prepore transforms into a transmembrane pore. The rupture of vesicles occurs when r goes to infinite within a very short time (~ 1 s). If r reaches to r_c stochastically, pore formation occurs stochastically, whose analysis provided the rate constant of pore formation in vesicles [27]. The use of viscous solvent allowed the direct visualization of the fast dynamics of pore creation and pore annihilation in vesicles which was stretched by intense optical illumination [28-29]. Using micropipette aspiration technique, the rupture of vesicles has been investigated under dynamic applied tension in which loading rates were applied [30-32]. The kinetics of constant mechanical tension-induced pore formation in the membranes of vesicles has been investigated by the micropipette aspiration technique [27]. The investigation of rate constant in these processes accounts for the rate of transition between relevant vesicle states along with the mechanism of pore formation. The mechanical stability of membranes due to electrostatic effects has been investigated using micropipette aspiration experiment [14, 33]

It is well known that plasma membranes of mammalian cells generally consist of 10–20% anionic lipid [34], whereas bacterial membranes contain about 80% [35-36]. Since most biological membranes are enriched in anionic lipid and hence charged in aqueous solution, the investigation of critical tension for electroporation in membranes has drawn considerable attention. The repulsive force of the charge-charge interactions overpowers membrane cohesive forces, and the cell becomes ruptured due to the pore formation in their membranes.

The critical tension of rupture formation in GUVs was acquired by the area compressibility modulus measurement [33], though the critical value of tension depends on the experimental technique. As for example, the critical tension of pore formation decreased significantly with the decrease of the rate of applied tension [30-31]. It was studied the rupture of black lipid membranes (BLMs) by short electric voltage pulses and found the almost same breakdown voltages of anionic phosphatidylserine membrane and neutral phosphatidylcholine membrane [37-38]. Therefore, it is necessary to research using spherical lipid vesicles such as GUVs that are structurally more relevant to cellular membranes than BLMs [37].

For cells under the influence of an electric field, many phenomena can be manifested depending on the characteristics of the field. For weak electric field intensities that are considered to be noninvasive, cells may undergo deformation, rotation or movement caused by electrophoretic and dielectric forces, which are based on the interaction of the cell membrane charges with the electric field and the dielectric polarization of the cell membrane, respectively [18]. These effects are widely exploited in many applications, for instance, with suspended cell membranes, they can be used for cell shorting or for guiding cells in microfluidic systems among others [18]. There are many other effects such as cellular reorientation in the presence of an electric field, tissue repair, cell membrane differentiation, etc. [19-20].

Immunohistochemistry study of the immune effector cells infiltrating the LPB tumors before, 2 h and 6 after the treatment of the tumors by irreversible electroporation [31]. The authors conclude that the mechanism of necrosis occurs independent of the immune system and may therefore be a suitable treatment option for immunocompromised patients [32]. Recently showed that IRE can serve as an independent and new method to ablate substantial volumes of tissue [33]. Complete ablation of the targeted liver tissue was achieved by exposing the tissue to electric pulses with parameters that do not induce thermal damage [34] but irreversibly permeate the cells and induce necrosis. Another recent study evaluated the long-term effects of IRE in a large animal model [34]. The results demonstrated that IRE has the potential to ablate large volumes of tissues.

However, the mechanism of pore formation in membrane of the cells of these investigations is not clear and more study is necessary. Therefore, we will synthesis the

model membrane (thickness 4 nm) in the form of GUVs of sizes $\geq 10 \mu\text{m}$. Here, an electric field (pulsed) is applied to the GUVs, after a short delay, transmembrane voltages is induced on the membranes. More specifically, it was observed how the model membranes respond to high electric fields when applied with nanosecond durations [12].

IRE is a minimally invasive non thermal tumors ablation technique where a series of short pulses with high frequency electrical energy is applied for destabilizing the cell membranes [39-40]. It has been hypothesized that such ablation is occurred due to the rupturing of the cells by IRE [4-6]. Artificially synthesized lipid membranes of vesicles have been considered as a mimic of bio membranes of cells and therefore GUVs have been used as alternative tool of cells for the rupturing of vesicles [8-9].

In addition, the kinetics of mechanical tension-induced pore formation was investigated by micropipette aspiration technique [11]. To elucidate the mechanism of IRE-induced rupturing of vesicles, it is important to investigate the kinetics of pore formation by varying the surface charge density of membranes. The kinetics constant of rupturing gives the information on the rate of transition from intact vesicles to ruptured vesicles [14]. Here, the effects of surface charge density on the electrically-induced rate constant of rupture formation of GUVs was investigated.

As we mentioned above IRE has been prominently used for the ablation of tumor and cancer cell, therefore it is significant to study the kinetics of pore formation of GUVs by changing the surface charge density of membrane under constant electrical stress. Moreover, it is also essential to explore the critical tension of electroporation in anionic lipid vesicles under constant electrical stress, which has been measured by studying the probability of pore formation in vesicles. Basically, it is the minimum tension required for the 100% pore formation in GUVs. Here the lateral electrical tension in the membranes has been induced by the electric field pulses (pulsating DC) of frequency 1.1 kHz. It was varied the surface charge density of membranes and investigated the rate constant of pore formation and the critical tension of pore formation under constant electric field due to IRE signal. of vesicles. The mechanism behind the pore formation with changing the surface charge density of membranes is revealed.

1.2 Objective of the Study

The objectives of the study are as follows:

- (i) Synthesis of lipid membranes of GUVs by the natural swelling method.
- (ii) Purification of GUV using membrane filtering method.
- (iii) Investigation of pore formation in the membranes of GUVs using IRE technique for various surface charge density of membranes.
- (iv) Statistical analysis of pore formation for obtaining the probability of pore formation and the rate constant of pore formation.
- (v) Estimation of line tension from the fitting of tension dependent rate constant of pore formation.
- (vi) Investigation of the critical tension of electroporation in anionic lipid vesicles under constant electrical stress.

1.3 Outline of the Thesis

There are five chapters in this thesis paper.

In the first chapter, the basic introduction for IRE and pore formation in membranes of cells/vesicles are discussed. The objective of the present study as well as the importance of this investigation is summarized.

In chapter two, the previous research works are discussed. Here, the properties of cell membrane, models of cell membrane and classical theory of IRE technique are discussed.

In chapter three, the used materials and reagents along with the experimental method of applying IRE signal in GUVs are presented.

The most significant chapter of the thesis is chapter four in which the results are discussed. The effects of the change of surface charge density on IRE is discussed in this chapter. The results of critical tension by changing the surface charge density of vesicles is also discussed.

Finally, in chapter five, the conclusions are discussed.

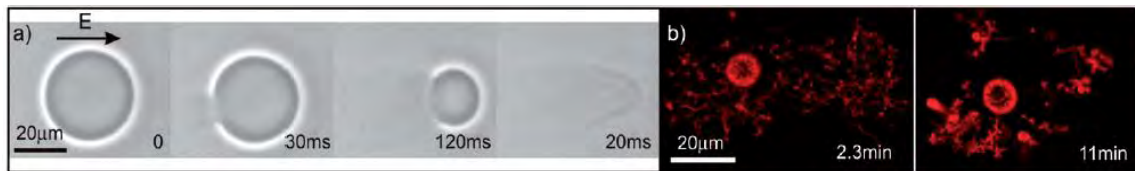
CHAPTER 2

LITERATURE REVIEW AND THEORATICAL ASPECTS

2.1 Literature Review

Dimova *et al.* in 2009 [41] investigated the effects of electric field in Giant Unilamellar Vesicles (GUVs). They applied nanosecond AC pulses to these vesicles and observed the effects such as poration, fusion and deformation. They also concluded from their investigations that vesicles response to electric field can be exploited to evaluate the mechanical properties of membranes. They reported that GUVs can be very useful in understanding the complex behavior of cells in electric field. Fig. 2.1 shows the poration and deformation of GUVs after applying electric field.

(i)



(ii)

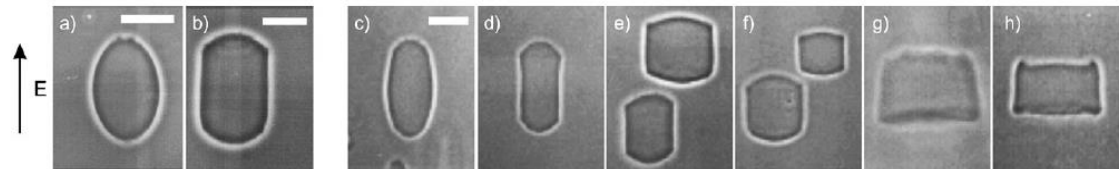


Fig. 2.1 Lipid membrane behavior with DC electric field through IRE (i) Bursting of charged (POPC : POPG, 1 : 1) vesicles subjected to electric pulses. The time after the beginning of the pulse is marked on each image (ii) Vesicle deformation to DC pulses in the presence and absence of salt and gold particles. The direction of the field is indicated by the arrow on the left and the scale bar corresponds to 15 μm [41].

Rubinsky *et al.* in 2007 [42] investigated the effects of IRE on pig liver. The goal of the study was to test IRE tissue ablation methodology in the pig liver, provided the first experience results on long term histopathology of IRE ablated tissue, and discussed the clinical implications of the findings. They observed cell ablation to the margin of the treated lesion with several cells thickness resolution. There appears to be complete ablation to the margin of blood vessels without compromising the functionality of the

blood vessels, which suggests that IRE is a promising method for treatment of tumors near blood vessels (a significant challenge with current ablation methods). Fig. 2.2 shows the treatment planning and surgical protocol for irreversible electroporation ablation in pig liver.

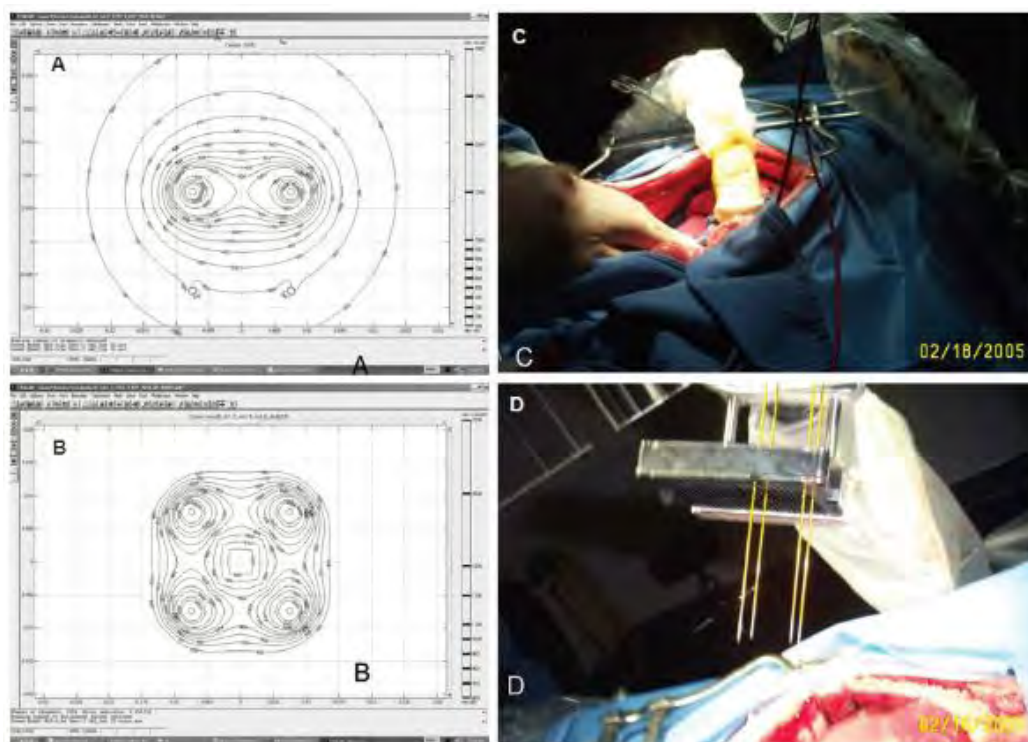


Fig. 2.2 Treatment planning and surgical protocol for irreversible electroporation ablation in the pig liver. IRE pulse parameters are bipolar electroporation, 2.5 kV pulses applied in a train of eight 100 microsecond pulses separated by 100 milliseconds. Four electrodes 18 gage stainless steel electrodes, 1.5 cm distance between probes. (A) Results of mathematical analysis showing constant electrical field magnitude isolines during the application on an electroporation pulse between two electrodes. The numbers on the figures indicate the magnitude of the electrical field in increments of 100 V/cm starting from 100 V/cm (outer isoline). The power delivered during each pulse is 1.2 J per cm depth of electrode. (B) Results of mathematical analysis show constant electrical field magnitude isolines due to the superposition of the application of the IRE pulses between the four pairs of IRE electrodes. The numbers on the figures indicate the magnitude of the electrical field in increments of 100 V/cm starting from 600 V/cm (outer isoline). Experiments have shown that 600 V/cm induces irreversible electroporation in liver. (C) Photograph of application of electroporation probes with ultrasound, (D) insertion of a set of four electrodes [42].

Minimally invasive tissue ablation has become of central importance in the modern surgery armamentarium.

Al-Sakere *et al.* [43] reported the first effective use of irreversible electroporation for the insignificantly invasive treatment of aggressive cutaneous tumors implanted in mice. The results were obtained by using a procedure that contained of 80 pulses of 100 μ s at 0.3 Hz (an interval of 3.3 seconds between pulses) with a field magnitude of 2500 V/cm. With this protocol complete regression was achieved in 12 out of 13 treated tumors and no thermal effects were induced which is shown in Fig. 2.3.

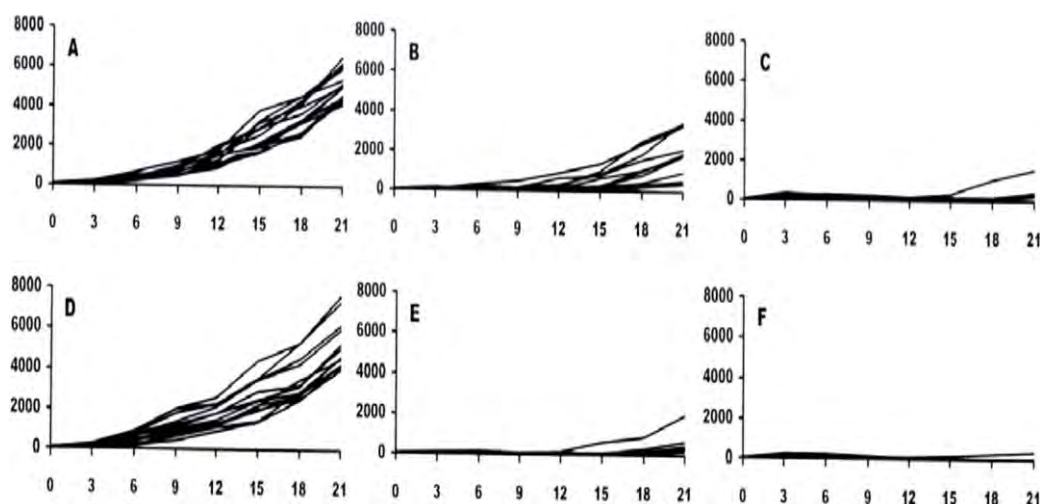


Fig. 2.3 Determination of appropriate electrical parameters for an effective tumor treatment by IRE – experiments with immunocompetent mice. Panels are identified by letters corresponding to the parameters, except for panel A (tumor growth in untreated mice followed as controls of treatment conditions B and C), panel D (control of E and F), panel G (control of H and I) and panel J (control of K and L) [43].

Riske and Dimova *et al.* [44] had investigated the deformation and poration of giant unilamellar vesicles exposed to electric pulses. They applied square-wave pulses of different strengths and durations to egg-PC giant unilamellar vesicles to study vesicle electrodeformation and electroporation. To facilitate the classification of the shape deformation, the vesicles chosen were either spherical (no visible thermal fluctuations) or quasispherical (detectable thermal fluctuations). In the former case, the membrane could have nonzero initial tension, so $\sigma_0 > 0$, although in the second instance it is reasonable to assume that the membrane was tension-free, i.e., $\sigma_0 \sim 0$. In Fig. 2.4, arrows in the insets indicate the position of the tense-free poration limit V_c . Stars mark experiments for which macropores were observed. For all conditions above V_c

macropores were detected as expected. However, in three subthreshold pulses ($V > V_c$), marked with numbers in the insets of Fig. 2.4, macroporation was also detected. Apparently, the vesicle has gotten the poration edge because of some initial tension. The reported results on the deformation and relaxation of giant unilamellar vesicles are the first to show the shape response of a giant lipid vesicle to an electric pulse at high time resolution.

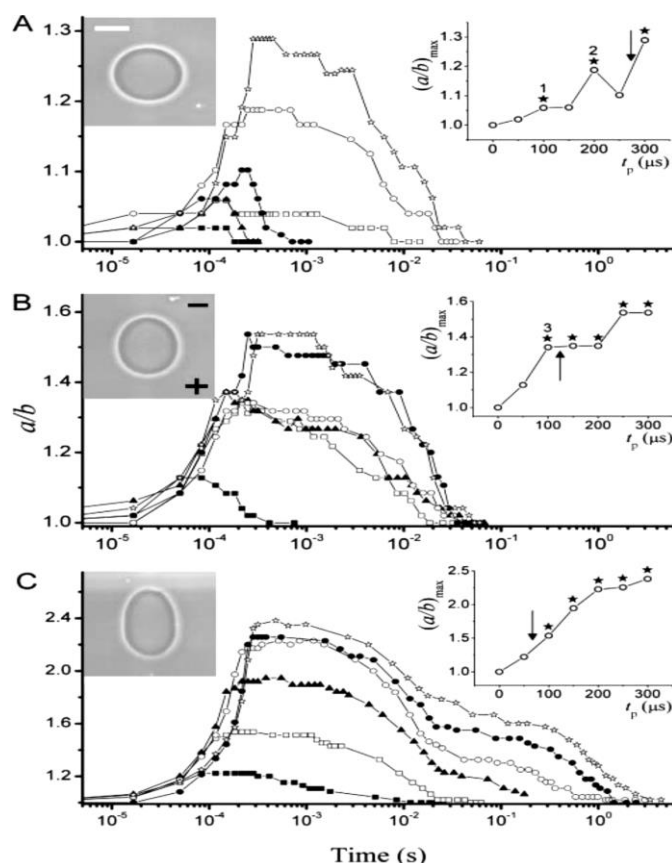


Fig. 2.4 Degree of deformation (a/b) induced on one vesicle when applying different square-wave pulses: (A) 1 kV/cm, (B) 2 kV/cm, and (C) 3 kV/cm. For each pulse strength, the applied pulses were of duration $t_p = 50$ ms (\blacksquare), 100 ms (\square), 150 ms (\blacktriangle), 200 ms (\circ), 250 ms (\bullet), and 300 ms (\star). The image acquisition rate was 30,000 fps. Time $t = 0$ was set as the beginning of the pulse. The insets show the maximum value of the deformation $(a/b)_{\max}$ as a function of pulse duration, t_p , for each pulse strength. Arrows indicate the tense-free poration limit ($V_p > V_c$). The time interval between applying consecutive pulses was generally 5 min. The images on each graph correspond to the maximal elongation for the pulse of duration $t_p = 150$ ms. The scale bar indicates 15 μm . The electrode's polarity is indicated with a plus and a minus sign on the second snapshot [44].

Shoemaker *et al.* [45] used the micropipette aspiration technique to characterize the elastic moduli and critical tensions of lipid vesicles with varying surface charge. Charge was induced by doping neutral phosphatidylcholine vesicles with anionic lipids phosphatidylglycerol and phosphatidic acid. Measurements were taken in potassium chloride (moderate ion-lipid binding) and tetramethylammonium chloride (low ion-lipid binding) solutions. They showed that inclusion of anionic lipid did not appreciably alter the areal dilation elasticity of lipid vesicles. However, the tension required for vesicle rupture decreased with increasing anionic lipid fraction and was a function of electrolyte composition. Using vesicles with 30% charged (i.e., unbound) anionic lipid, they measured critical tension reductions of 75%, demonstrating the important role of electrostatic interactions in membrane stability. Using the micropipette aspiration technique, they have shown that anionic lipids do not alter the elasticity of lipid vesicles but substantially reduce their mechanical stability. The Fig. 2.5 shows the relation of critical tension and % of anionic lipid in different buffers.

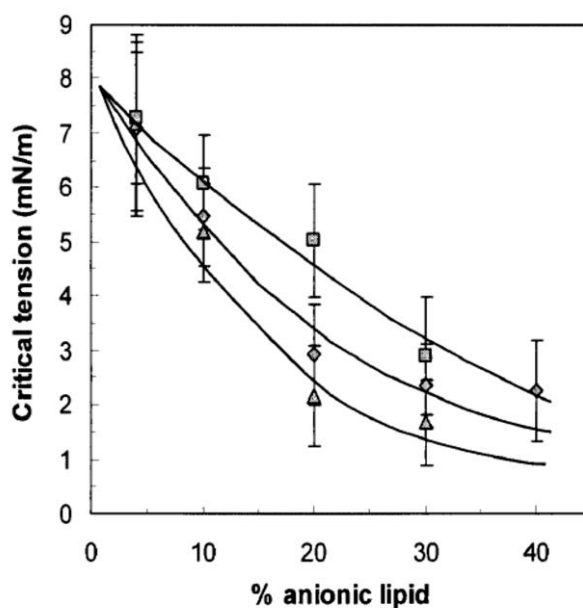


Fig. 2.5 Measured critical stresses for anionic vesicles in 1 mM electrolyte. Triangles, diamonds, and squares correspond to POPG/POPC in TMA-Cl, POPG/POPC in KCl, and POPA/POPC in KCl, respectively [45].

Karal *et al.* [46] investigated further into the effects of electrostatic interactions on rate constant (k_p) for tension induced pore formation in GUVs. They changed the salt concentration of buffer solution as well as the composition of lipid membranes. They obtained the results that with the decrease of salt concentration increased the rate

constant and increase in surface charge density increase the rate constant. They Fig. 2.6 shows the obtained data for change in surface charge density from the study.

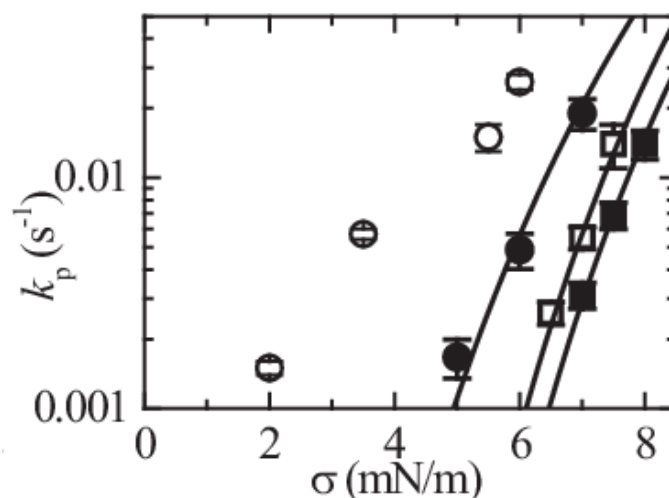


Fig. 2.6 Tension dependence of k_p for GUVs of DOPG and DOPC mixture for different values of fraction X of DOPG. Average values and standard errors of k_p for each tension were determined for three independent experiments using 20 GUVs for each experiment. The solid lines show the best-fit theoretical curves with $D_r = 165 \text{ nm}^2/\text{s}$ and $a = 0.45$. Effect of surface charge density at constant C ($=162 \text{ mM}$). 100% DOPC (\blacksquare), 10% DOPG/90% DOPC (\square), 40% DOPG/60% DOPC (\circ), and 70% DOPG/30% DOPC (\bullet). The best-fit curves are shown for $X = 0$ ($\Gamma = 10.5 \text{ pN}$), 0.10 ($\Gamma = 10.4 \text{ pN}$), and 0.40 ($\Gamma = 11.4 \text{ pN}$). The data for 100% DOPC GUVs and 40% DOPG/60% DOPC-GUVs at $C = 162 \text{ mM}$. [46].

Levadny *et al.* [47] studied the effects of tension induced by micropipette aspiration on giant unilamellar vesicles (GUVs) composed of dioleoylphosphatidylglycerol (DOPG) and dioleoylphosphatidylcholine (DOPC). They investigated the time course of the fraction of intact GUVs among all of the GUVs under constant tension σ and obtained the rate constants of pore formation $k_p(\sigma)$. In fig. 2.7 (B), the tension dependent results of rate constant is seen. They concluded from their results that the rate constant k_p for 40% DOPG/60% DOPC increases with the increase of tension. The probability of pore formation Fig. 2.7 (C) also increases with tension. The curves were fitted to this theoretical equation:

$$\tau = \left(\frac{1}{D_r} \right) \int_0^{r_b} \exp[U(r)/k_B T] \left\{ \int_0^r \exp[-U(z)/k_B T] dz \right\} dr \quad (2.1)$$

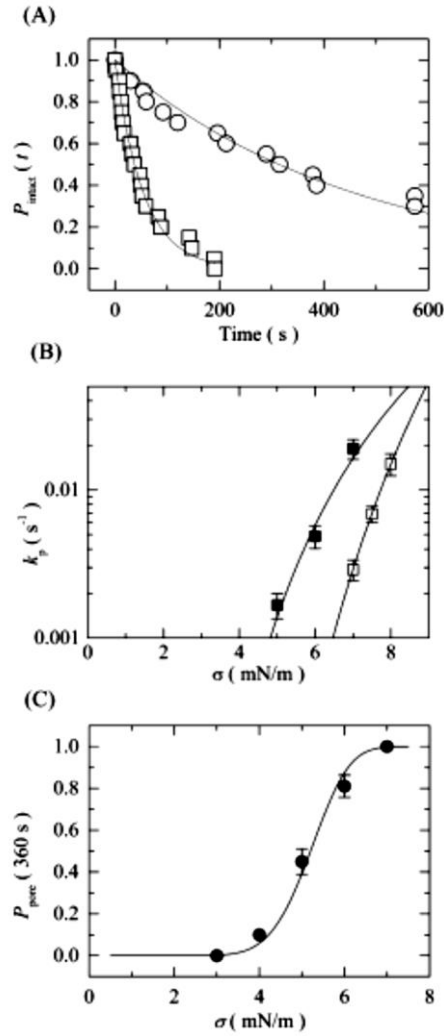


Fig. 2.7 Effect of constant tension on pore formation in single GUVs. (A) Time course of the fraction of intact 40% DOPG/60% DOPC GUVs without rupture among all of the examined GUVs, $P_{\text{intact}}(t)$, in the presence of tension. σ : (\circ) 5.0, (\square) 7.0 mN/m. The number of examined single GUVs was 20 in each experiment. (B) Dependence of k_p on tension. (\blacksquare) 40% DOPG/60% DOPC-GUV and (\square) DOPC-GUV. Average values and the standard error in k_p for each tension were determined among three independent experiments using 20 GUVs for 40% DOPG/60% DOPC membranes and 16–20 GUVs for DOPC membranes for each experiment. Error bars show standard errors. The solid lines show the best fits in accordance with the theoretical curves corresponding to eq 2.1 using $\Gamma = 7.0$ pN and $D_r = 1.2 \text{ nm}^2/\text{s}$ for 40% DOPG/60% DOPC-GUV and $\Gamma = 10.5$ pN and $D_r = 165 \text{ nm}^2/\text{s}$ for DOPC-GUV. (C) Dependence of $P_{\text{pore}}(360 \text{ s})$ in 40% DOPG/60% DOPC-GUV on tension. Scale bars show standard errors [47].

Ahmed *et al.* [48] investigated the kinetics of irreversible pore formation under constant electrical tension in GUVs. The GUVs were prepared by a combination of dioleoylphosphatidylglycerol (DOPG) and dioleoylphosphatidylcholine (DOPC) using the natural swelling method. An IRE signal of frequency 1.1 kHz is applied to the GUVs through a gold-coated electrode system. Stochastic pore formation is observed for several ‘single GUVs’ at a particular constant tension. The time course of the fraction of intact GUVs among all the examined GUVs is fitted with a single-exponential decay function from which the rate constant of pore formation in the vesicle, k_p , is calculated. The value of k_p increases with an increase of membrane tension. An increase in the proportion of negatively charged lipids in a membrane gives a higher k_p . Theoretical equations are fitted to the tension-dependent k_p and to the probability of pore formation, which allows us to obtain the line tension of the membranes. The decrease in the energy barrier for formation of the nano-size nascent or prepore state, due to the increase in electrical tension, is the main factor explaining the increase of k_p .

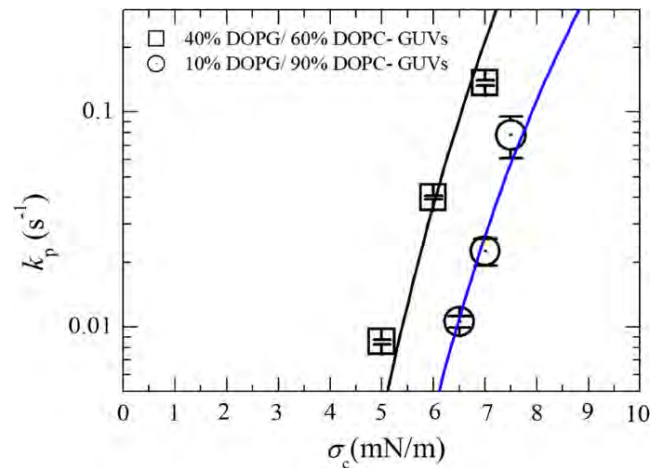


Fig. 2.8 Tension-dependent average k_p for 40% DOPG/60% DOPC-GUVs (square) and 10%DOPG/90% DOPC-GUVs (circle). The solid line shows the best-fitting theoretical curve corresponding to with $A_F = 1.9 \times 10^8 \text{ m}^2\text{s}^{-1}\text{J}^{-1}$ and $\Gamma = 12.1 \text{ pN}$ for 40% DOPG/60% DOPC-GUVs and $A_F = 4.2 \times 10^6 \text{ m}^2\text{s}^{-1}\text{J}^{-1}$ and $\Gamma = 10.1 \text{ pN}$ for 10% DOPG/90% DOPC-GUVs [48].

2.2 Cell Membrane Physiology

The cell membrane is a border that divides living cells from its environments. This displays the physiognomies of semipermeable barrier that permits some ingredients to cross more easily than the others. It is penetrable to some very trivial molecules like water, oxygen and carbon dioxide also to some other hydrophobic molecules (like amino acid, protein, DNA, RNA, ions) which have polar properties. The cell membrane contains numerous kinds of proteins which act as channels that can pass these molecules inside the membrane. The transmembrane passage of essential ions like Na^+ , K^+ , Ca^{2+} and Cl^- is largely controlled by the cell with ion pumps and exchangers. These let the cell to form up chemical and electrical gradients.

Under biological circumstances the cell keeps chemical gradients for Na^+ and K^+ through the cell membrane to enable the membrane potential that is necessary to many cellular purposes. The majority of cellular responses is controlled by the Ca^{2+} signaling method and the concentration of free Ca^{2+} in the cytoplasm is under firm control. It is preserved very small ($\sim 0.1 \mu\text{M}$) inside the cell, whereas the outside concentrations of free Ca^{2+} are multifold greater ($\sim 1.3 \text{mM}$). Great levels of intracellular ATP (Adenosine Triphosphate) entertain the different active ports that sustain these gradients and maintain the energy-dependent cellular procedures which the cell integrity.

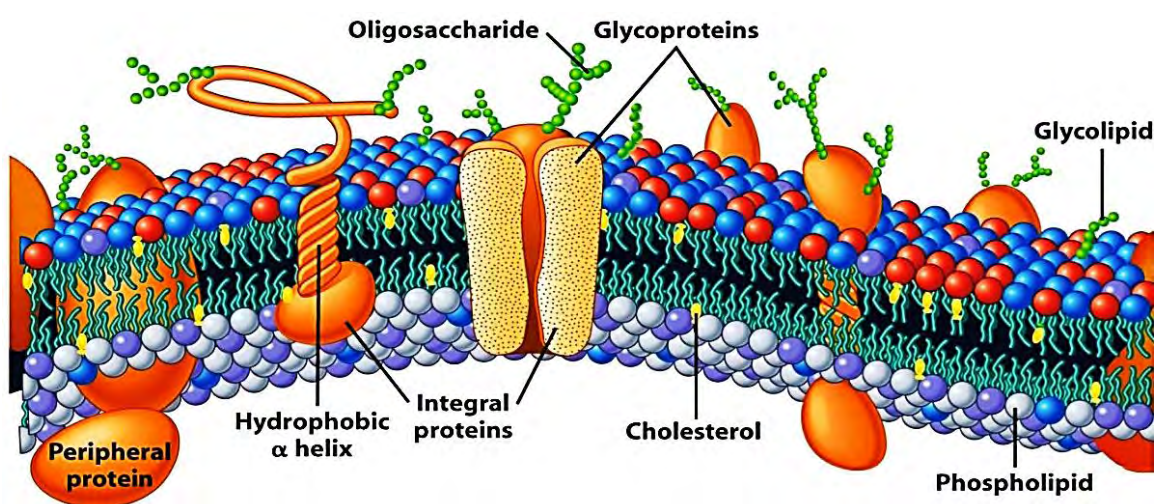


Fig. 2.9 A detailed diagram of the cell membrane [49].

Dependent on the power and/or time period electric fields are applied to a cell membrane it either temporarily (electroporation) or perpetually rises the permeability to molecules or ions by seemingly creating so titled nanopores. The interchange of

molecules and water transport over these nanopores can cause irreversibility in two methods. Primarily, the variation in ionic concentrations and loss of intracellular content can extent to the point outside which the cell cannot recover [50]. Subsequently, colloidal-osmotic swelling can lead straight to membrane rupture [51]. The swelling happens on the time period of minutes [52], so it contends with resealing of pores, which continues with approximately the similar rate. These pores in the cell membrane lead to a decaying of the Na^+ and K^+ gradients and the loss of the cell's regulator over Ca^{2+} levels because of a huge inflow of Ca^{2+} from the extracellular matrix. The cell efforts to recompense development by advancing much of its energy in the form of ATP into sustaining the transmembrane ion gradients using the Ca^{2+} , Na^+ and K^+ -ATPase's. These efforts quickly drain the cell's energy sources and this adds up to the direct loss of ATP out of the cell. Triggered by the loss of the cell membrane the production of reactive oxygen species (ROS) rises rapidly and manifoldly, leading to more membrane damage and protein denaturation. These deviations pose potential uncertainties to a cell's ability and can stimulate uncontrolled signals that lead to necrotic or apoptotic cell death. Depending on the aspects of electroporation and the time of the permeabilization the cell may be capable to recuperate before control of Ca^{2+} level is lost and reseal, or else expire.

Biological membranes are thought to be able to recuperate totally on particular circumstances. Whereas pores from electroporation form in microseconds it takes minutes to reseal them, depending on electrical factors and temperature. Variables for resealing, are the availability of sufficient ATP for the Na^+ , K^+ ATPase to recuperate membrane potential and for the Ca^{2+} ATPase to move sufficient of the free intracellular Ca^{2+} out of the cell or into the loadings of the sarcoplasmic or endoplasmic reticulum (SR or ER) or the mitochondria. If the cell succeeds to reseal the membrane and redevelop ion homeostasis, it can remain and the electroporation would be reversible.

Under the conditions where the cell does not succeed to regenerate ion homeostasis, the made pores become permanent and consequently the cell is permeabilized indeterminately. The resulting Ca^{2+} excess and the ROS formation being set in motion lead to a secondary collapse of the membrane in a vicious sequence. This sequence results in the loss and decrease of all the ATP resources, the collapse of the membrane and eventually in cell loss either via apoptosis (a controlled method requiring ATP) or by necrosis.

2.3 Lipid Bilayer Structure

Lipids are compounds that are nonpolar in nature and is only soluble in nonpolar solvents. The lipid membrane is a bilayer structure which protects the cell components inside the cells from surroundings. Lipids are basically classified into two categories which are- simple lipids and complex lipids. All of the lipids found in cell membrane are amphipathic i.e. they have a hydrophilic or polar end and hydrophobic or non-polar end. The most profuse lipid found in cell membrane are phospholipids which have a polar head group and two hydrophobic non-polar tails.

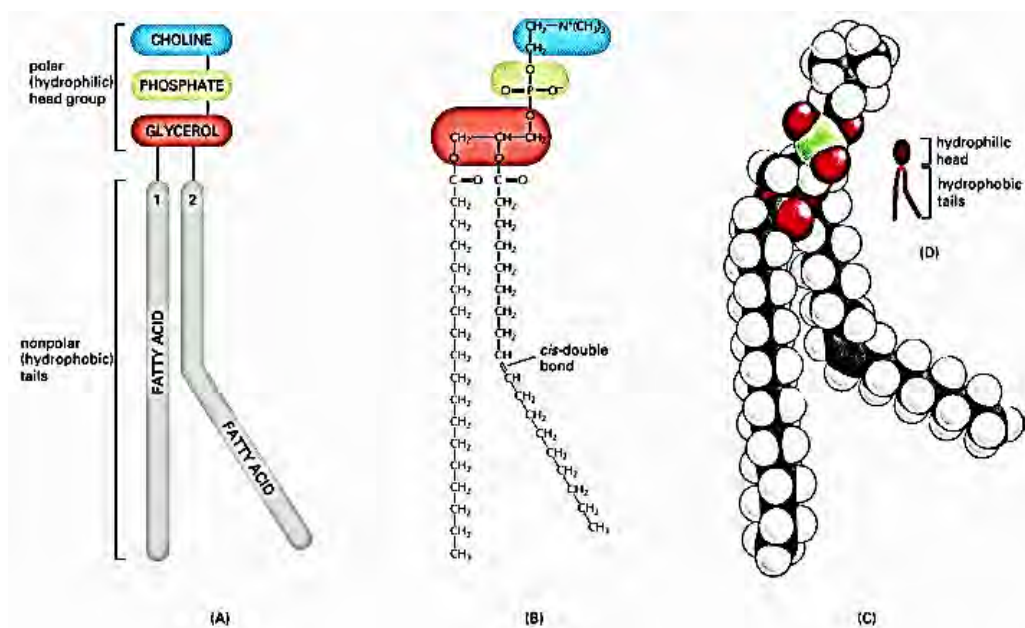


Fig. 2.10 The parts of a phospholipid molecule. This example is phosphatidylcholine, represented (A) schematically, (B) by a formula, (C) as a space-filling model, and (D) as a symbol [53].

The amphipathic nature of lipid molecules plays the most important role in their shape and forming bilayer in aqueous medium spontaneously. Hydrophilic molecules dissolve easily in water because they have charged groups or uncharged polar groups that can form either favorable electrostatic interactions with polar molecules. Hydrophobic molecules on the other hand are insoluble in water because all, or almost all, of their atoms are uncharged and nonpolar and therefore cannot form energetically favorable interactions with water molecules. If dispersed in water, they force the adjacent water molecules to reorganize into ice like cages that surround the hydrophobic molecule. Because these cage structures are more ordered than the

surrounding water, their formation increases the free energy. This free energy cost is minimized, however, if the hydrophobic molecules (or the hydrophobic portions of amphipathic molecules) cluster together so that the smallest number of water molecules is affected. For this reason, the lipid molecules tend to keep their hydrophobic tails in the inside and hydrophilic head in the outside exposed to water. Depending on this, they can form two types of shape- one is spherical micelle with tails inward or bilayer formation in which tails remain between two head groups.

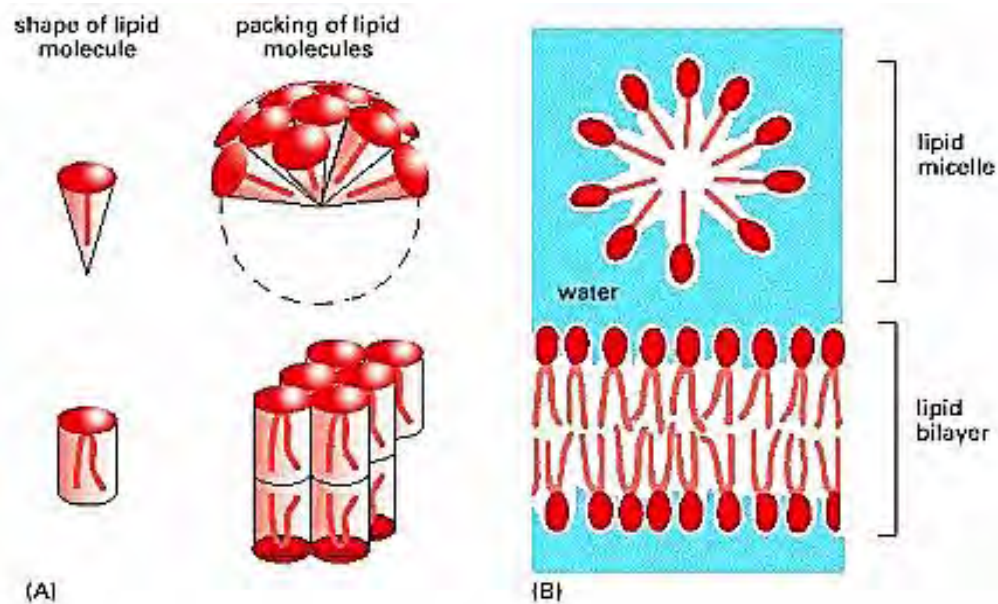


Fig. 2.11 Packing arrangement of lipid molecules in water environment (A) Wedge shaped lipid molecules form micelles (above) whereas cylinder shaped lipid molecules (below) form bilayers (B) a lipid micelle and lipid bilayer seen in cross section [54].

The fluid mosaic model of phospholipid bilayers that makes up cell membranes allow cells to exhibit semipermeable properties. The channel and gate proteins give cell membranes selective permeability to regulate the exchange between the intracellular and extracellular environments of various components, including ions. This allows the cell to maintain electrical potential gradients between these two environments, creating a potential difference across the membrane. Most mammalian cells have a small transmembrane potential of roughly 70 mV, where the external environment contains slightly more positive charge than the intracellular environment [55]. This potential gradient is maintained by proteins in the membrane. The phospholipid bilayer of cell membranes therefore results in complex electrical properties, which may be electrically

modeled by a resistor and capacitor in parallel. The capacitor represents the membrane's properties as a dielectric, where charges are capable of being built up on either side, but cannot cross, while the resistor represents the ability for some ion exchange due to occasional leakiness of the membrane or protein-facilitated ion exchange.

The distinctive electrical features of mammalian cell membranes permit one to imagine the cell as a high conductivity intracellular solution enclosed by a dielectric separating it from an outside atmosphere of additional high conductivity solution. When this system is placed in the presence of a constant or low frequency (≤ 10 kHz) external electric field, the membrane's capacitor behavior induces a polarization of the cell, similar to that of homogeneous materials, where ions move in response to the polarity of the electric field [56]. This results in the movement of negative ions, such as chlorine (Cl^-), towards the positive side of the electric field, while positive ions, such as sodium and potassium (Na^+ and K^+) are driven towards the negative side of the electric field. Within the cell, these ions are constrained by the dielectric cell membrane, resulting in an accumulation of the charged ions at each end. In contrast, the extracellular ions accumulate on the alternate corresponding charge of the cell. This method results in oppositely charged ions gathering at both side of the cell membrane, causing an electric potential gradient through the membrane.

2.4 Model Membrane

The biological membranes are an intricate structure to study. This intricacy of membrane has inspired the improvement of a large variety of simpler model systems whose size, geometry, and structure can be tailored with great meticulousness. Model membranes are predominantly suitable in studying significant membrane related phenomena. A model membrane have the key structures of a biological membrane and it can be investigated individually. They can be used in a wide variety of applications for example mechanical and physical properties of membrane in addition to the interaction of lipid molecules and proteins.

Methods of model membrane contains vesicles, sustained bilayers, and fusion membrane arrangements. These have been used to investigate problems ranging from phase properties to membrane fusion. Experimental membrane models continue to

improve in intricacy with respect to architecture, size, and structure, as do computer simulations of their properties and dynamics. Model systems and methods that have seen great advancement in the past few years are shown in Fig. 2.12 These comprise: bilayers in the form of vesicles ranging in size from tens of nanometers (small unilamellar vesicles, SUV's) to tens of microns (giant unilamellar vesicles, GUV's) that are either freestanding or tethered to supports; planar supported bilayers either interacting directly with a solid substrate or tethered to the substrate; bilayer islands wrapped by proteins; and fragments from natural cell membranes.

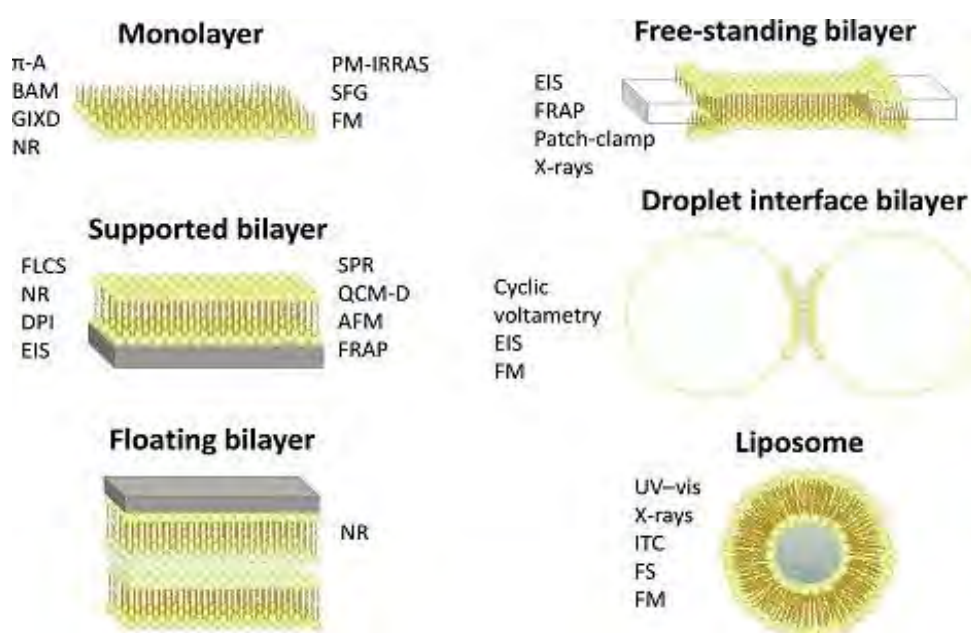


Fig. 2.12 Model membrane representing the same complexity as a mimic of bio membrane.

2.5 Vesicles

A vesicle is a small structure within a cell, consisting of fluid enclosed by a lipid bilayer. Vesicles form naturally during the processes of secretion (exocytosis), uptake (phagocytosis) and transport of materials within the cytoplasm. Alternatively, they may be prepared artificially, in which case they are called liposomes. Vesicles can fuse with the plasma membrane to release their contents outside the cell. Vesicles can also fuse with other organelles within the cell. The self-closing of flexible bilayer pages in dilute aqueous solution is determined by the removal of the actively unfavorable contact of the hydrophobic boundaries with water. According to this self-meeting process, the basic

vesicle construction is usually defined as a hollow sphere that covers an aqueous solution in the core surrounded by a bilayer membrane. With such morphology, the aqueous core of vesicle can be used for the encapsulation of therapeutic molecules such as drugs, proteins and peptides, DNA, while the membrane can integrate hydrophobic drugs. This opportunity to load both hydrophilic and hydrophobic medicines is one of the great interests of vesicles for therapeutic applications. Vesicles prepared from phospholipids are usually called liposomes and from amphiphilic copolymers, polymerases.

2.6 Vesicles and its Classification

Vesicles are defined as small spherical shaped structures that consists of fluid separated from surrounding by lipid bilayer. Vesicles store and transport materials with the cell. Since they are mainly composed of lipid bilayer, they can have completely self-contained environment different from inside the cell [57]. They are also known as liposomes.

Vesicles are classified into two main categories based on their structure. They are-

- (i) Unilamellar vesicles that have only one lipid bilayer
- (ii) Multilamellar vesicles that have more than one lipid bilayer

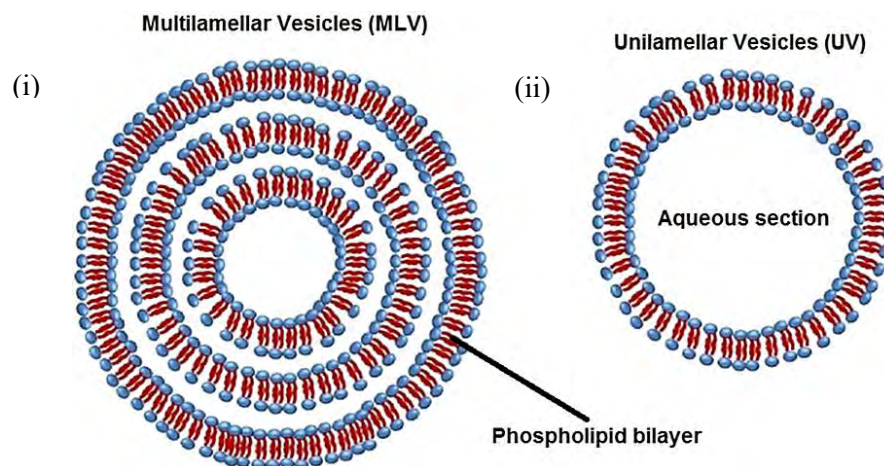


Fig. 2.13 Vesicle (i) Multilamellar (ii) Unilamellar

The unilamellar vesicles can be divided into three categories based on their size. They are-

- i. Small Unilamellar Vesicle (SUV) with size range of 20-100 nm
- ii. Large Unilamellar Vesicle (LUV) with size range of 100-1000 nm

iii. Giant Unilamellar Vesicle (GUV) with size range of 1-200 μm .

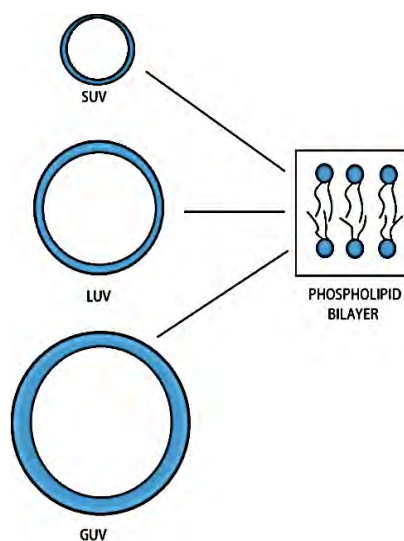


Fig. 2.14 Different types of vesicles.

Giant unilamellar vesicles (GUV's) have diameters on the order of one to ten microns and have been instrumental in determining the phase behavior of binary and ternary lipid mixtures in bilayers [58]. GUV's are typically created using well-defined mixtures of pure lipids, but still unclear is the relationship between the behavior of these model systems and actual biological membranes which are much more complex mixtures of lipids, proteins, and saccharides. GUVs are mainly used as model membrane in order to study the membrane behavior due to its similarity with bio membrane.

2.7 Phospholipids

Phospholipids are amphiphiles consist of two fatty acid tails, a glycerol unit, a phosphate group and a polar molecule. The polar head molecule and phosphate group form the hydrophilic area and describe both type of phospholipid, including zwitterionic groups with zero overall net charge at physiological pH, such as phosphatidylcholine (PC) and phosphatidylethanolamine (PE) or anionic groups with negative net charge such as phosphatidylglycerol (PG), phosphatidylserine (PS) and phosphatidylinositol (PI). The outstand ding part is a glycerol molecule esterified by two fatty acids, founding hydrophobic region that can be of different lengths (between 12- 24 carbons) and degree of saturations. Phospholipids are the main element of biological cell membranes.

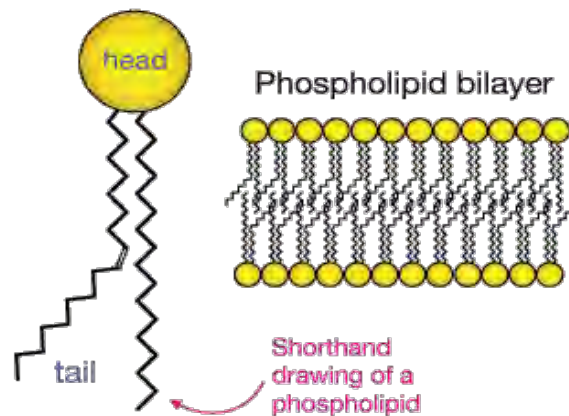


Fig. 2.15 Schematic diagram of lipid bilayer [59].

2.8 Membrane Electrical Model and Equation

2.8.1 The mechanism of charges of surfaces in liquid

Van der Waals force is a weak attractive force. When Van der Waals force works alone in any system, it attracts all the similar particles in the system and precipitates out of the solution. It doesn't happen to our body since there is also a repulsive force working due to charged particles within the water in the body. The charging of a surface in liquid can happen in three ways:

- (i) By The ionization or dissociation of surface groups which makes the surface negative.
- (ii) By the absorption of ions from a previous uncharged surface—for example, the adsorption of OH^- groups to the water-air or water-hydrocarbon interfaces that charges them negatively, or the binding of Ca^{2+} onto the zwitterionic head groups of lipid bilayer surfaces that charges them positively. The ion absorption can also happen in oppositely charge surface sites which are known as ion exchangeable surfaces.
- (iii) The exchange of ions in dissimilar surfaces very close to one another give rise to an electrostatic attraction between the now oppositely charged surfaces.

Usually two surfaces with similar charges repel each other but under certain conditions they might attract each other at small difference. Zwitterionic surfaces which is, those

surfaces categorized by surface dipoles but no net charge also interact electrostatically with each other, though here it will be found that the force is typically attractive.

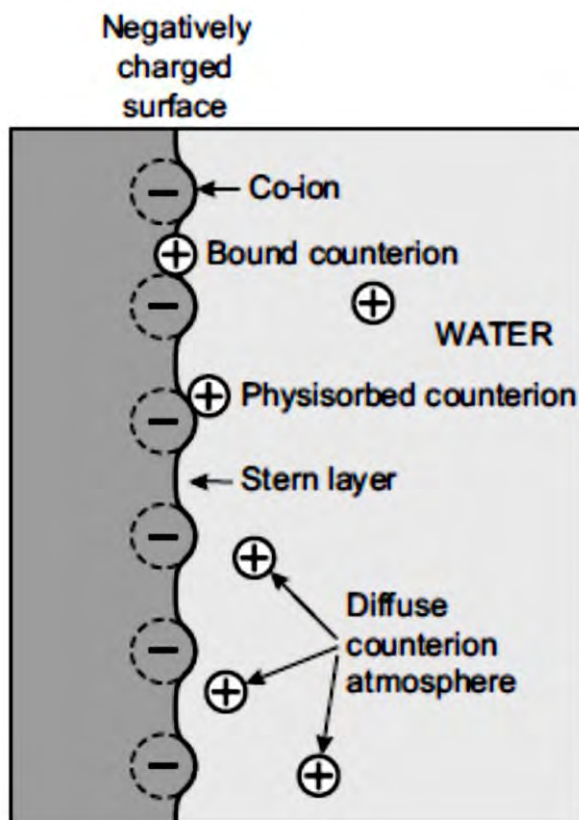


Fig. 2.16 Ions bound to a surface are not rigidly bound but can exchange with other ions in solution; their lifetime on a surface can be as short as 10^{-9} s (1 ns) or as long as many hours [60].

2.8.2 Charged surfaces in water without added electrolyte

In a pure liquid like water, the counterion distribution and force between two similarly charged planer surfaces can only occur due to ions present in the surface. These systems are often referred as “counterions only” systems and they happen when colloidal particles, clay sheets, surfactant micelles or bilayers whose surfaces comprise ionizable assemblies interrelate in pure water, and also when thick films of water build up (condense) on an ionizable surface such as glass. But first some essential equations needs to be discussed which will help to describe the counterion distribution between two charged surfaces in solution.

2.8.3 The Poisson-Boltzmann (PB) equation

When only counter ions are present in solution, the chemical potential of any ion may be described as:

$$\mu = ze\psi + kT \log \rho \quad (2.11)$$

Where, ψ is the electrostatic potential and ρ the number density of ions of valency z at any point x between two surfaces. Since only variances in potential are ever physically significant, ψ_0 is set to 0 at the midplane ($x=0$), $\rho = \rho_0$ and $(d\psi/dx)_0=0$ by equilibrium.

From the equilibrium condition that the chemical potential be unchanged throughout (i.e., for all values of x), Eq 2.11 gives us the anticipated Boltzmann distribution of counterions at any point x (the Nernst equation):

$$\rho = \rho_0 e^{-Zk\psi/kT} \quad (2.12)$$

The Poisson equation for net excess charge density at x is also required.

$$ze\rho = -\epsilon_0\epsilon (d^2\psi/dx^2) \quad (2.13)$$

Combining with the Boltzmann it gives the Poisson- Boltzmann (PB) equation.

$$d^2\psi/dx^2 = -ze\rho / \epsilon_0\epsilon = (-ze\rho_0 / \epsilon_0\epsilon) e^{-ze\psi/kT} \quad (2.14)$$

After solving the equation, the potential ψ , electric field $E = -\delta\psi/\delta x$ and counterion density ρ , is determined at any point x in the gap between the two surfaces. First these values at the surfaces themselves are determined. These numbers are frequently denoted to as the contact values: ψ_s , E_s , ρ_s , and so on.

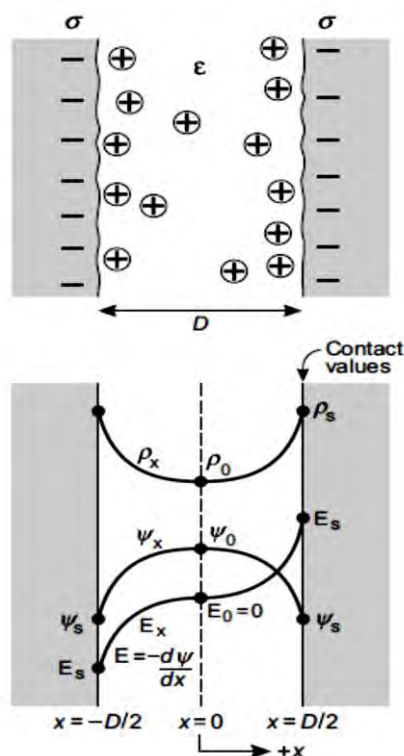


Fig. 2.17 Two negatively charged surfaces of surface charge density σ separated a distance D in water. The only ions in the space between them are the counterions that have dissociated from the surfaces. The counterion density profile ρ_x and electrostatic potential ψ_x are shown schematically in the lower part of the figure. The “contact” values are ρ_s , ψ_s and $E_s = - (d\psi/dx)_s$ [60].

2.8.4 Charged surface in electrolyte solution

The charged surface can easily interact with a solution which contains electrolyte ions. Even “pure water” at pH 7 is strictly an electrolyte solution containing 10^{-7} M of H_3O^+ and OH^- ions, which cannot always be ignored. For a charged remote surface exposed to a solvent containing no added electrolyte ions (only the counterions), the distance D and contact value ψ_0 becomes infinity. As it is seen, this unrealistic situation is removed as soon as the bulk solvent contains even the minuscule concentration of electrolyte ions. The existence of a “bulk reservoir” of electrolyte ions has a profound effect not only on the electrostatic potential but also on the forces between charged surfaces, and in the rest of this chapter we shall consider this interaction as well as the total interaction when the ever-present van der Waals force is added. But to understand the double-layer interaction between two surfaces it is necessary to first understand the ionic distribution adjacent to an isolated surface in contact with an electrolyte solution. Consider an

isolated surface, or two surfaces far apart, in an aqueous electrolyte. For convenience, we shall put $x = 0$ at the surface rather than at the midplane.

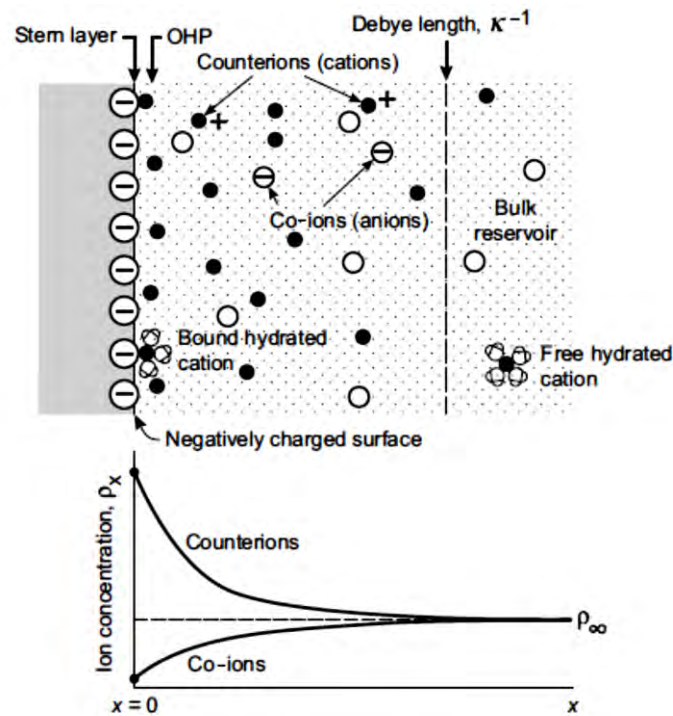


Fig. 2.18 Near a negatively charged surface there is a growth of counterions (ions of contrasting charge to the surface coions) and a reduction of coions, shown graphically here for a 1:1 electrolyte, where ρ_{∞} is the electrolyte concentration in the bulk or “reservoir” at $x = \infty$. Counterions can adsorb to the surface in the dehydrated, partially hydrated, or fully hydrated state. The OHP is the plane beyond which the ions obey the Poisson-Boltzmann equation. This plane is usually farther out than the van der Waals plane [60].

Now, all the essential equations derived in the earlier sections are related to solutions containing diverse kinds of ions i (of valency z_i) so long as this is taken into account by expressing the net charge density at any point x as $\sum_i z_i e \rho_{xi}$ and the total ionic concentration (number density) $\sum_i \rho_{xi}$. Thus, Eq. for the Boltzmann distribution of ions i at x now becomes.

$$\rho_{xi} = \rho_{\infty i} e^{-z_i e \psi / kT} \quad (2.15)$$

while at the surface, at $x = 0$, the contact values of r and j are related by

$$\rho_{0i} = \rho_{\infty i} e^{-z_i e \psi_0 / kT} \quad (2.16)$$

where, $\rho_{\infty i}$ is the ionic concentration of ions i in the bulk (at $x = \infty$) where $\psi_0 = 0$.

2.8.5 The Grahame equation

Let us now find the total concentration of ions at an isolated surface of charge density σ . This is immediately given by

$$\sum_i \rho_{oi} = \sum_i \rho_{\infty i} + \sigma^2 / 2\epsilon_0 \epsilon kT \quad (2.17)$$

Thus, for $\sigma = -0.2 \text{ Cm}^{-2}$ (corresponding to one electronic charge per 0.8 nm^2 or 80 \AA^2) at 25°C , we find $\sigma^2 / 2\epsilon_0 \epsilon kT = 7.0 \times 10^{27} \text{ m}^{-3} = 11.64 \text{ M}$. For a 1:1 electrolyte such as NaCl, the surface concentration of ions in this case is

$$[\text{Na}^+]_o + [\text{Cl}^-]_o = 11.64 + [\text{Na}^+]_\infty + [\text{Cl}^-]_\infty = 11.64 + 2[\text{Na}^+]_\infty = 11.64 + 2[\text{NaCl}] \text{ M}$$

while for a 2:1 electrolyte such as CaCl_2 ,

$$[\text{Ca}^{2+}]_o + [\text{Cl}^-]_o = 11.64 + [\text{Ca}^{2+}]_\infty + [\text{Cl}^-]_\infty = 11.64 + 3[\text{Ca}^{2+}]_\infty = 11.64 + 3[\text{CaCl}_2] \text{ M}$$

So the Grahame equation obtained is,

$$\begin{aligned} \sigma^2 &= \sqrt{\epsilon_0 \epsilon kT} \sinh(e\psi_o / 2kT) \{[\text{Na}^+]_\infty + [\text{Ca}^{2+}]_\infty (2 + e^{-e\psi_o / kT})\}^{1/2} \\ &= 0.117 \sinh(\psi_o / 51.4) \{[\text{NaCl}] + [\text{CaCl}_2]_\infty (2 + e^{-\psi_o / 25.7})\}^{1/2} \end{aligned} \quad (2.18)$$

Some effects of the Grahame equation are considered, bearing in mind that it does not predict σ or ψ_o , but just relates them.

2.8.6 Surface charge of isolated surfaces

More generally, a surface may contain both anionic (e.g., acidic) and cationic (e.g., basic) groups to which various cations and anions can bind. Such surfaces are known as amphoteric, and the competitive adsorption of ions to them can be analyzed by assigning a binding constant to each ion type, and then incorporating these into the Grahame equation. The charge density of amphoteric surfaces (e.g., protein surfaces) can be negative or positive depending on the electrolyte conditions. At the isoelectric point (iep) or point of zero charge (pzc) there are as many negative charges as positive charges so that the mean surface charge density is zero ($s = 0$), although it is important to remember that there may still be local regions of high negative or positive charge. Such discrete local charges become crucially important for determining the short-range and adhesion forces between amphoteric surfaces and biological macromolecules, and we return to consider such acid-base and protein substrate interactions in later sections.

2.8.7 Debye length

At small potential, the Grahame equation can be simplified as

$$\sigma = \epsilon_0 \epsilon \kappa \psi_0$$

$$\text{Where, } \kappa = (\sum_i \rho_{\infty i} e^2 z_i^2 / \epsilon_0 \epsilon kT)^{1/2} \text{ m}^{-1}$$

Thus, the potential becomes proportional to the surface charge density. For a capacitor whose two plates are separated by a distance $1/\kappa$, have charge densities $\pm\sigma$, and potential difference ψ_0 . This analogy with a charged capacitor gave rise to the name diffuse electric double-layer for describing the ionic atmosphere near a charged surface, whose characteristic length or “thickness” is known as the Debye length, $1/\kappa$. The magnitude of the Debye length depends solely on the properties of the solution and not on any property of the surface such as its charge or potential. For a monovalent electrolyte ($z = 1$) at 25 °C (298K) the Debye length of aqueous solutions is

$$\begin{aligned} k^{-1} &= (\epsilon_0 \epsilon kT / 2\rho_{\infty} e^2)^{1/2} = \left(\frac{8.854 \times 10^{-12} \times 78.4 \times 1.381 \times 10^{-23} \times 298}{2 \times 6.022 \times 10^{26} \times (1.602 \times 10^{-19})^2 M} \right)^{1/2} \\ &= 0.304 \times 10^{-9} / \sqrt{M} \text{ m} \end{aligned} \quad (2.19)$$

Thus,

$$1/\kappa = \begin{cases} 0.304 / \sqrt{[NaCl]} \text{ nm} \\ 0.176 / \sqrt{[CaCl_2]} \text{ nm} \\ 0.152 / \sqrt{MgSO_4} \text{ nm} \end{cases}$$

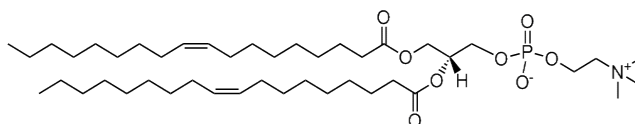
CHAPTER: 3

MATERIALS AND METHODS

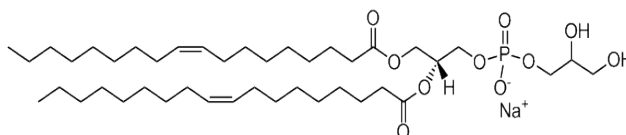
3.1 Chemicals and Regents

The chemicals and reagents used in this work are 1, 2-dioleoyl-*sn*-glycero-3-phosphotiglycerol (DOPG) and 1, 2-dioleoyl-*sn*-glycero-3-phosphocholine (DOPC) which were purchased from Avanti Polar Lipids Inc. (Alabaster, AL). Bovine serum albumin (BSA), 1, 4-Piperazinediethanesulfonic acid (PIPES), ethyleneglycol-*N,N,N',N'*-tetraacetic acid (EGTA) were purchased from Sigma-Aldrich (Germany). The structures of DOPG, DOPC and BSA is shown below.

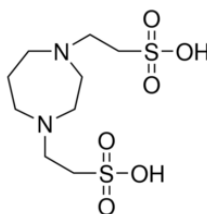
- **1, 2-dioleoyl-*sn*-glycero-3-phosphocholine (DOPC)**



- **1, 2-dioleoyl-*sn*-glycero-3-phosphotiglycerol (DOPG)**



- **Bovine serum albumin (BSA)**



- **Ethyleneglycol-*N,N,N',N'*-tetraacetic acid (EGTA)**
- **1,4-Piperazinediethanesulfonic acid (PIPES)**
- **Glucose**
- **Sucrose**
- **Calcein**

3.2 Synthesis of Lipid Membranes of GUVs

Giant unilamellar vesicles (GUVs) are very suitable for studying membrane actions as they are a mimic of biological cell [61-62]. Examples of using GUVs as simple model structures for separating certain physicochemical properties of biological membranes contain lipid domain construction [63-65], mechanical and rheological properties of the entire vesicle [66] or of the membrane [67,61,63], lipid dynamics, membrane development [68–71], membrane adhesion [72–76], wetting phenomena [77-78], budding and fission [79–83], and membrane fusion [84-88]. Giant vesicles are also a much applied tool to study the response of membranes to external perturbations like hydrodynamic flows [89], locally applied forces [90], micromanipulation [91], and electric fields [92-93]. The two most widespread methods for the development of giant vesicles are natural swelling or gentle hydration, introduced by Reeves and Dowben [94] and electroswellling, introduced by Angelova and Dimitrov [95]. A mixture of DOPG and DOPC lipids were used to synthesize the GUVs by the natural swelling method. The natural swelling method is described briefly in the following. A mixture of 1 mM DOPG and DOPC (total volume 200 μ L) was taken into a glass vial and dried with a mild flow of nitrogen gas to yield a slim, homogeneous lipid film. The residual chloroform in the film was removed by placing the vial in a vacuum desiccator for overnight. A quantity of 20 μ L MilliQ water was added into the glass vial and then pre-hydrated for 8 min at 45 $^{\circ}$ C [58]. After pre-hydration, celcein suspension was added to the sample. The celcein suspension was prepared with 1mL buffer containing 0.10M sucrose and the sample was incubated for 3.5 h at 37 $^{\circ}$ C [58] to produce a GUVs suspension. Celcein solution was prepared beforehand of a total 15 mL containing 9.34 mg celcein and 1.5 mL of 0.10 M pipes and 1.5 mL of 0.10 M sucrose which act as external solution. Membrane filtering method was used for obtaining the purified GUVs. An amount of 300 μ L purified GUVs suspensions were transferred into a U-shaped hand-made microchamber which was coated with 0.10% (w/v) BSA, dissolved in buffer containing 0.10 M glucose. The GUVs were observed using an inverted phase contrast microscope (Olympus IX-73, Japan) with a 20 \times objective at 25 ± 1 $^{\circ}$ C. The GUV images were recorded at 25 fps using a digital camera (Model: DP22, Olympus) connected to the microscope. The following block diagram and schematic diagram shows synthesis of GUVs using natural swelling method.

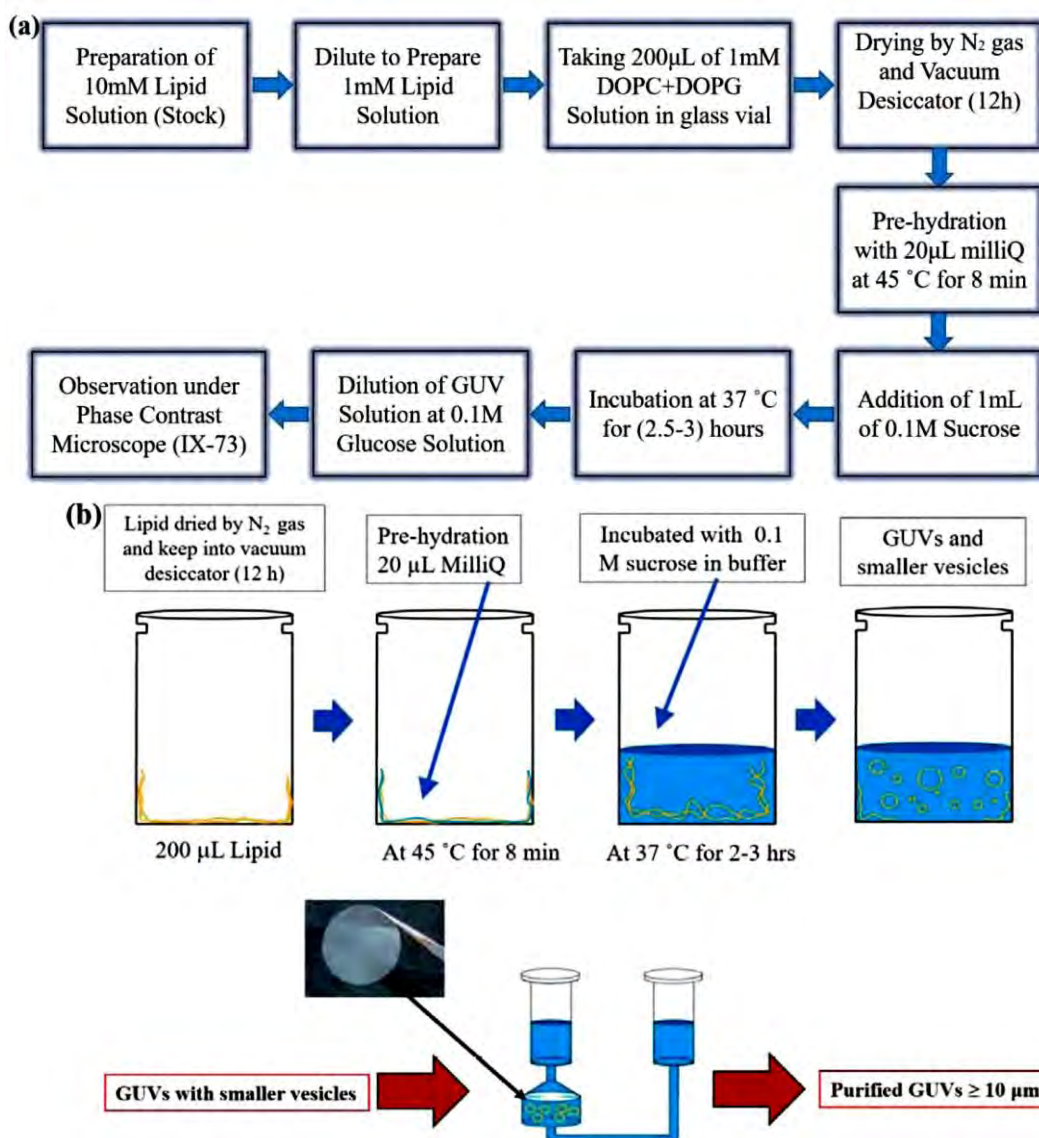


Fig. 3.1 Block diagram (a) and schematic diagram (b) showing steps of natural swelling method [96].

3.3 Preparation of Sample

Firstly, we took 80 µL DOPG and 120 µL DOPC (concentration of DOPG and DOPC was 1 mM) in chloroform into a 4.5 mL glass vial. In order to remove the residual chloroform in the lipid film in the glass vial, it was placed in a vacuum desiccator overnight (12 h). 20 µL MilliQ water was added in the fine dried lipid film into the glass vial and then lipid film was pre-hydrated by sinking the glass vial in a water fill beaker at 45 °C for 8 min. After pre-hydration, 1 mL of buffer (10 mM PIPES, pH 7.0, 150 mM NaCl and 1 mM EGTA) containing 0.10 M sucrose was added to the sample

and it was incubated for 2.5 to 3 hrs at 37 °C to produce GUVs suspension. After incubating the GUVs suspension in vial for 2.5 to 3 hrs, it was taken out. Then the GUVs suspension was taken in a 1.5mL Eppendorf tube using 1000 μ L micropipette. Eppendorf tube was carefully put on the centrifuge head such that the balance was maintained. The sample in Eppendorf tube was centrifuged at 13,000 \times g for 20 min at 20 °C using a refrigerated centrifuge (NF 800R, NUVE, Turkey).

We prepared four samples as follows:

- (i) 10%DOPG/90%DOPC (% indicates mole %) [DOPG mole fraction $X = 0.10$]
- (ii) 20%DOPG/80%DOPC [$X = 0.20$]
- (iii) 40%DOPG/60%DOPC [$X = 0.40$]
- (iv) 60%DOPG/40%DOPC [$X = 0.60$]

The surface charge density of membranes is defined $\Omega = eX/A$, where e is the electronic charge ($= -1.6 \times 10^{-19}$ C) and A is the area of lipid molecule ($= 72.5 \text{ \AA}^2/\text{molecule}$). Therefore, the surface charge densities of samples (i), (ii), (iii) and (iv) were -0.022, -0.044, -0.088, -0.1324 C/m², respectively.

3.4 Purification Method of Lipid Membrane

After incubation, the GUVs suspension was centrifuged at 13,000 RCF for 20 min at 20 °C using a refrigerated centrifuge (NF 800R, NUVE, Turkey) and then the supernatant containing GUVs was filtered through a 10 μ m diameter pores nuclepore polycarbonate membrane (Whatman® Nuclepore™ Track-Etched Membranes, UK) clamped in a polypropylene filter holder (Swinnex, $\phi = 25$ mm, Millipore Co., Billerica, MA). The organization of the purification system is illustrated in Fig. 3.2. The upper end of the filter holder was connected with a 10 mL plastic (polypropylene) syringe 2 (JMI Syringes and Medical Devices Ltd. Bangladesh) and the lower end was connected with a tube containing three different types of polypropylene fittings (Luer fittings VRFE6, VRFC6, VRSC6; AS-ONE, Japan) having inner diameter 3 mm as shown in Fig. 3.2. In this case, the tube contains a total number of 11 fittings instead of 9 that was used in the membrane filtering method. The other end of the tube was connected to syringe 1 having the same volume of 10 mL. The GUVs suspension in buffer containing 0.1 M glucose was added to syringe 1 where the flowing of buffer was

continuously controlled due to the double headed peristaltic pump (CPPSP2, Shenchen, China) through a plastic tube of inner diameter 3 mm (JMI Syringes and Medical Devices Ltd. Bangladesh). Before starting the flow of buffer from beaker to syringe 1, the air bubbles were carefully removed from the polypropylene tube and filter holder. The direction of the flow of buffer at the filter was from the bottom to the top, shown in Fig. 3.2, so the smaller vesicles passed through the filter into the upper syringe (syringe 2). After filtering for a definite time, the addition of buffer containing 0.1 M glucose to syringe 1 was stopped, and then the buffer inside syringe 2 was removed by the pump at the same flow rate. Lastly, the suspension in the tube and the filter holder was collected and used as a purified GUV suspension.

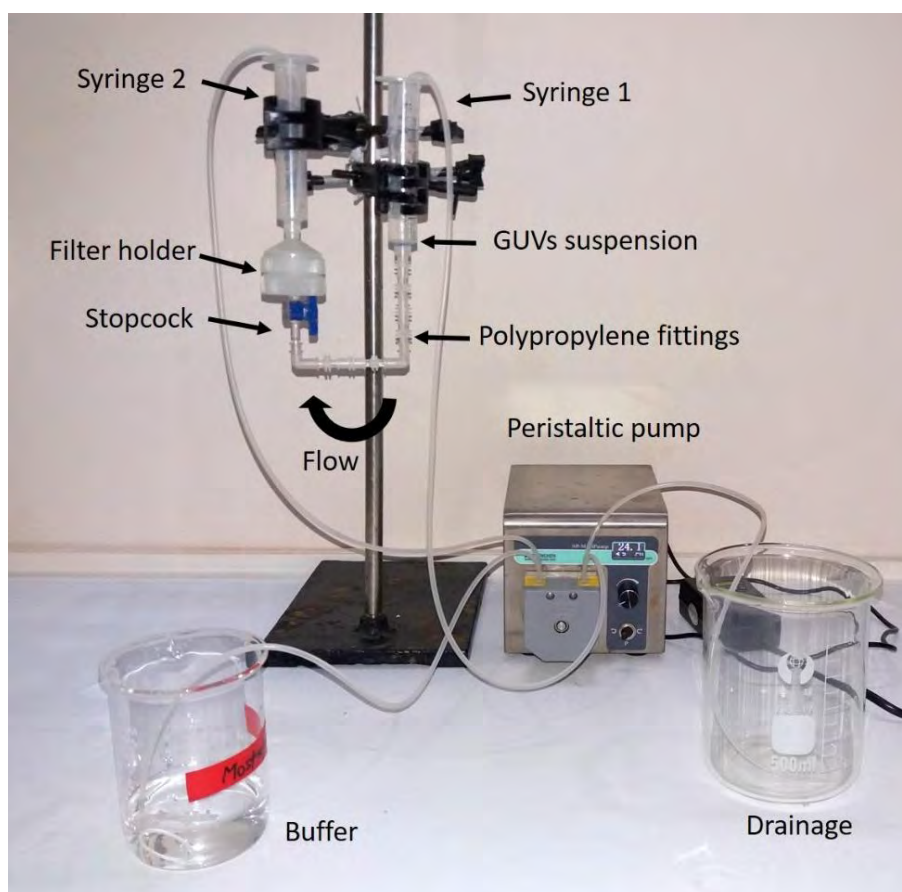


Fig. 3.2 Set-up of membrane filtering method.

3.5 Observations of Lipid Membrane of GUVs

3.5.1 Suspension of GUVs in microchamber

A handmade microchamber was made on a glass slide by inserting a U-shaped silicone rubber spacer between the cover slip and the glass slide. After the purification, 300 μL GUVs suspension was taken into this microchamber. In order to stop the strong interaction between the glass surface and GUVs, the inside of the microchamber was coated with 0.10% (w/v) BSA dissolved in the buffer containing 0.1 M glucose.

3.5.2 Microscopy

In order to view monochrome and translucent specimens and live cells, phase contrast microscopy is most appropriate. This technique utilizes the variance between light rays propagating straight from the light source and light rays refracted by the specimen when light passes through it to enhance bright/dark dissimilarity to images of transparent models. A phase-contrast objective and a condenser for observations are fitted with the microscope. Samples could be made to look dark against a bright background (positive contrast) or bright against a dark background (negative contrast). The borders of images are surrounded by a characteristic bright “halo.” The GUVs were observed using an inverted phase contrast microscope (Olympus IX-73, Japan) with a 20 \times objective at 25 ± 1 $^{\circ}\text{C}$ and the images were recorded using a digital camera (Model: DP22, Olympus) shown in fig. 3.3.

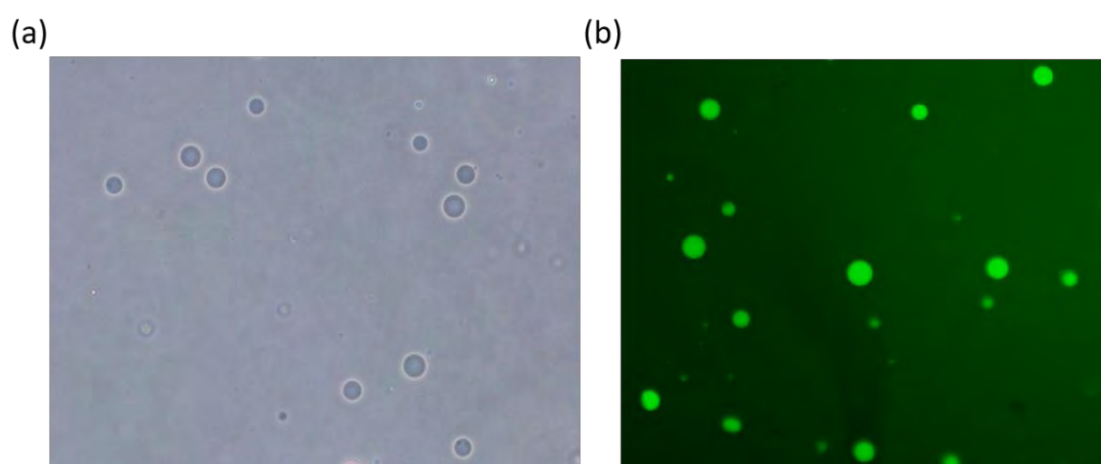


Fig. 3.3 (a) Phase Contrast image and (b) Fluorescence GUVs Images.

3.6 Description of the IRE Technique

The IRE method used in the present study is shown in the block diagram. At first the input of 220V AC in a single-phase transformer provided a flexible lesser output of 0

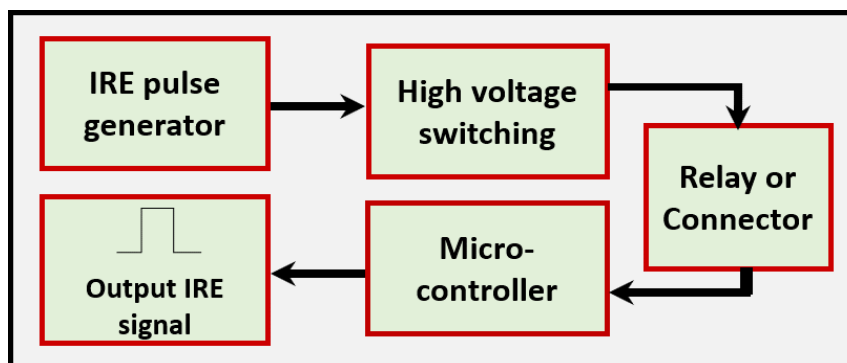


Fig. 3.4 Block diagram of IRE technique

to 800 V AC with lowest current of 5 A. A full wave rectifier was used to alter the AC output into DC. The square wave pulses of 1.1 kHz essential for the experiment were provided through a switching circuit based on MOSFET. The microcontroller-based IRE signal is applied to the GUVs through a gold coated electrode of length 17.0 mm and width 2.54 mm (Model: SH-17P-25.5, Hellotronics).

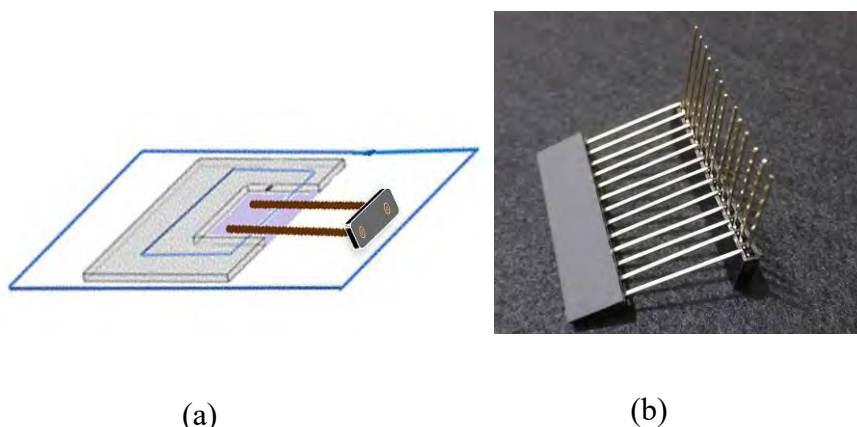


Fig. 3.5 Schematic diagram of gold coated electrode system for IRE (a) and Slots of gold coated electrode system for IRE (b).

It is well known that lipid membranes are impermeable to ions. Applying electric field, E , polarizes the free charges of buffer in which the accumulation time of free charges can be measured using the Maxwell–Wagner equation [97]. Free charges accumulation increases the membrane potential, V_m , which induces the membranes to stretch. Due to

the stretching of membranes a lateral electrical tension, σ_c , is induced in the membranes of GUVs which can be calculated by the following Maxwell stress tensor [98-100].

$$\sigma_c = \varepsilon_m \varepsilon_0 \left(\frac{h}{2h_e^2} \right) V_m^2 \quad (3.1)$$

Where, ε_m is the membrane permittivity (~ 4.5) [101-102], ε_0 is the permittivity of free space, h is the thickness of membrane (~ 4 nm) [103] and h_e is the membrane dielectric thickness (~ 2.8 nm) [104-105], we consider the uniform field on the GUVs as for simplicity. The induced V_m at each membrane point is defined by the Schwan's equation as follows [102-103].

$$V_m = 1.5RE |\cos \theta| \left(1 - e^{-t/\tau_{\text{charg}}} \right) \quad (3.2)$$

where θ is the angle between the radius of GUV R (from GUV center to evaluation point) and E and τ_{charg} is the charging time of membranes. If $\theta = 0^\circ$, the equation (2) can be simplified as follows by considering $\tau_{\text{charg}} \approx 0$.

$$V_m = 1.5RE \quad (3.3)$$

Therefore, equation (3.1) can be simplified as follows [102].

$$\sigma_c = 22.86R^2 E^2 [\text{mN/m}] \quad (3.4)$$

Equation (3.4) shows that σ_c can be defined as a function of E for a GUV with R . In the case of a GUV with $R = 10 \mu\text{m}$ and $E = 553 \text{ V/cm}$, $V_m = 0.8 \text{ V}$. For a particular value of R , σ_c can be considered constant for the value of E . A number of constant electrical tensions are used by choosing the appropriate value of E in this study. The value of uncertainty to apply the constant electrical tension on GUVs was very insignificant, it was $\sim 4\%$ to that of applied tension.

Constant electrical tension was applied in GUVs while doing this experiment. In this method, firstly the E was kept constant at $\sim 340 \text{ V/cm}$ and a 'single GUV' was focused that stayed sandwiched between the electrodes as shown in Fig. 3.6. Then the value of E amplified quickly (5-8 s) to reach a precise value and this value of E was held constant for maximum 60 s (i.e. for a exact time). The time at which the GUV started to rupture

is defined as the time of pore formation which has a time resolution of ~ 1 s. The value of σ_c is premeditated using equation (3.4).

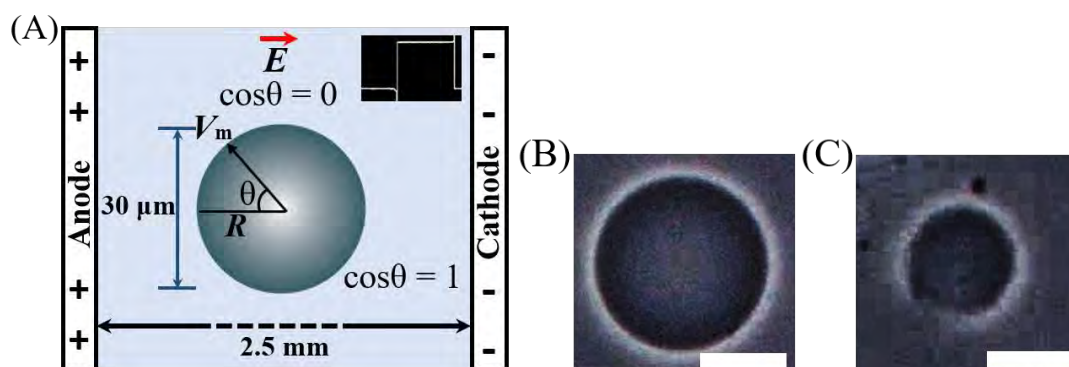


Fig. 3.6 Experimental design for the formation of pores in GUVs in IRE technique. (A) An application of E induces a modification of the transmembrane potential of GUVs. The IRE signal is shown in the inset. (B) A single intact GUV, (C) Ruptured GUV. White bar in (B, C) corresponds to a length of 15 μm . [105].

CHAPTER 4

RESULTS AND DISCUSSION

4.1 Pore Formation in 20%DOPG/80%DOPC-GUVs at 5.75 mN/m

At first, the electroporation in 20%DOPG/80%DOPC-GUVs was taken into consideration. The tension of the membrane, σ_c of a value of 5.75 mN/m was applied for 60s on a ‘single GUV’ and the effect of this tension was observed. During observation for some time, it was apparent that the GUV was broken suddenly as shown in Fig. 4.1 (a).

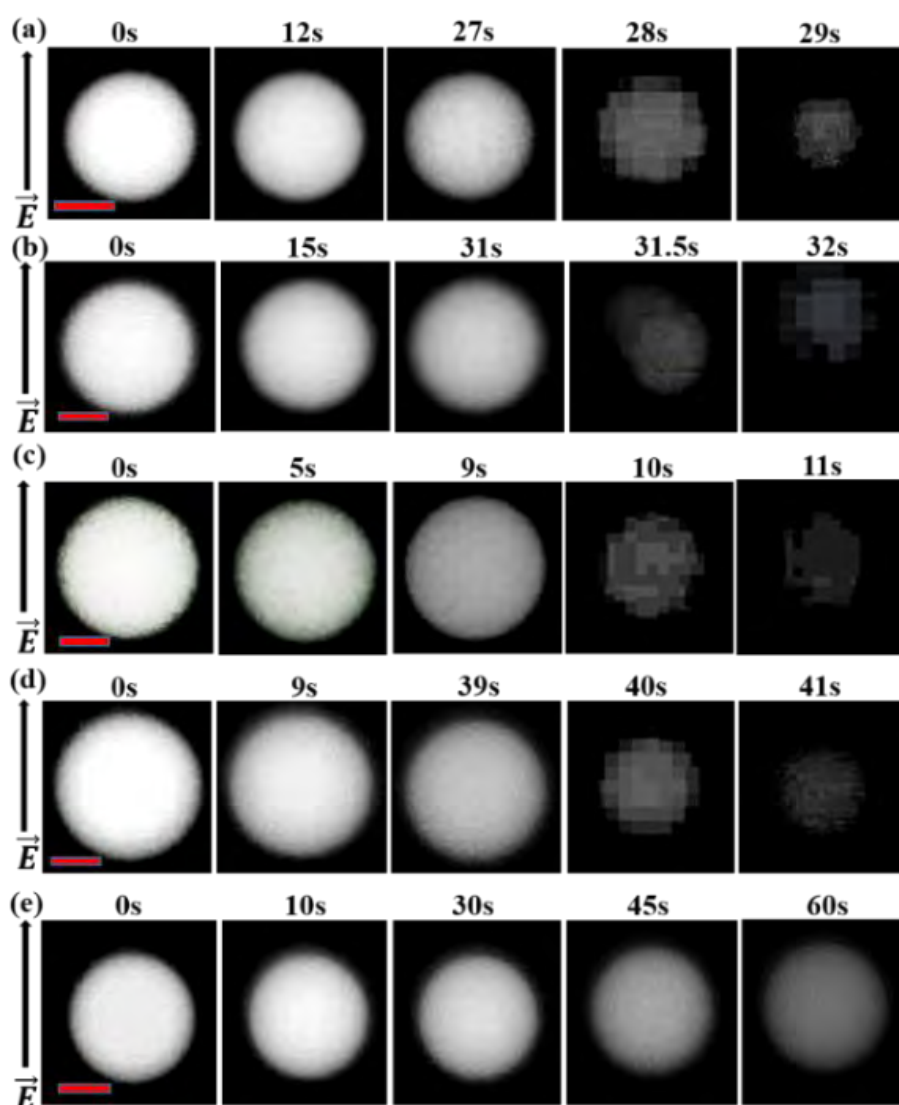


Fig. 4.1 Pore formation of (a) 1st (b) 2nd (c) 3rd (d) 4th and (e) 5th single 20%DOPG/80%DOPC- GUVs at 5.75 mN/m. The scale bar corresponds to a length of 16 μm .

The contrast in the image of GUV before and after applying electrical tension can be seen in Fig.4.1 (a) at 0s. Before applying the tension, the GUV was completely intact and had a spherical shape. It can be observed from the Fig. 4.1 (a) that the GUV was intact with spherical shape until time = 27s in the presence of σ_c . The GUV was completely intact until time 27s in the presence of electrical tension. But at time 28s the GUV started to rupture and at time 29s the GUV completely loses its spherical shape and permanently vanishes. In this observation the calcine was inside the GUVs. So, the GUV wasn't observed after it was completely destroyed.

We observed the 2nd 20%DOPG/80%DOPC GUV and investigated the similar phenomena as shown in Fig.4.1 (b). It was intact till 31s. At 31.5s it was suddenly ruptured. Then completely loses its shape by 32s. After this the GUV can't be seen because all the internal solution has leaked out. The 3rd GUV was also ruptured. In this case the GUV ruptured very quickly after applying the tension. At 0s the GUV was intact. It was intact till 9s. At 10s the GUV started to lose its shape. At 11s the GUV vanished completely. The 4th 20%DOPG/80%DOPC GUVs was ruptured at 40s in presence of 5.75 mN/m tension (Fig.4.1 (d)). In case of the 5th GUV, it didn't rupture (Fig. 4.1 (e)).

4.2 Probability of Pore Formation in 20%DOPG/80%DOPC-GUVs at 5.75 mN/m

At first, the pore formation in the membranes of many single 20%DOPG/80%DOPC-GUVs at tension 5.75 mN/m was investigated. From the observed result, it was obvious that although the value of tension was constant at 5.75 mN/m for 17 single GUVs, but pore formation occurred at different time. The fraction of pore formation in GUVs among all of the examined GUVs at a given tension is defined as $P_{\text{pore}}(t) = 1 - P_{\text{intact}}(t)$ which provided the probability of pore formation at that constant tension. As an example, for the first independent experiment 17 single GUV were observed at tension 5.75 mN/m in which 4 GUVs were intact, so $P_{\text{pore}}(t) = 1 - 4/17 = 0.76$ and the second independent experiment 17 single GUV were observed at tension 5.75 mN/m in which 6 GUVs were intact $P_{\text{pore}}(t) = 1 - 6/17 = 0.64$. The time of pore formation for several 20%DOPG/80%DOPC-GUVs at tension 5.75 mN/m for two independent experiments are shown in table. 4.1.

Table. 4.1: Time of pore formation for several 20%DOPG/80%DOPC-GUVs at tension 5.75 mN/m for two independent experiments.

First independent experiment			Second independent experiment		
GUV-label number (n)	Times of pore formation (s)	P_{pore} (60s)	GUV-label number	Times of pore formation (s)	P_{pore} (60s)
1	36	0.76	1	42	0.64
2	50		2	Intact	
3	4		3	Intact	
4	Intact		4	12	
5	7		5	4	
6	54		6	56	
7	18		7	Intact	
8	52		8	52	
9	24		9	30	
10	Intact		10	58	
11	Intact		11	52	
12	22		12	57	
13	58		13	59	
14	36		14	55	
15	Intact		15	Intact	
16	45		16	Intact	
17	49		17	Intact	

The GUV rupture is observed when the radius of nano-sized pore increases rapidly to infinity. The time of pore formation is found from the initiation time of rupture. When a specific value of tension, σ_c is taken into consideration, it was observed that the many ‘single GUVs’ form pore stochastically. From this information it was concluded that, even during constant tension the GUVs shows pore formation at different times. For different values of σ_c it is observed that the pore formation of many ‘single GUVs’ have the stochastics characteristics. It can be explained more clearly by the graphs shown below. Fig.4.2 (a) and (b) show the pore formation of 17 GUVs each at tension 5.75 mN/m for two independent experiments.

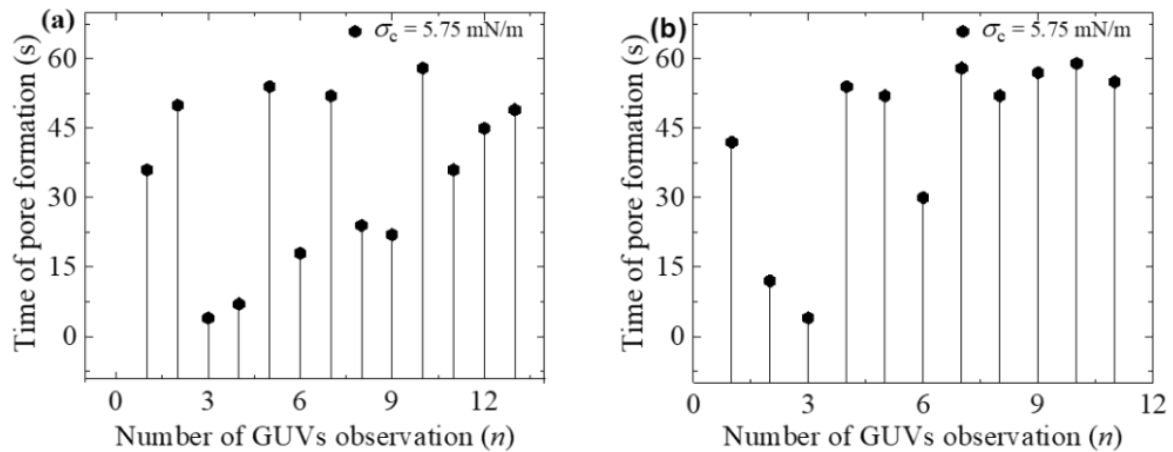


Fig. 4.2 Stochastic pore formation for 20%DOPG/80%DOPC- GUVs at 5.75 mN/m for (a) 1st independent experiment and (b) 2nd independent experiment.

4.3 Rate Constant Pore Formation in 20%DOPG/80%DOPC-GUVs at 5.75 mN/m

In order to determine the rate constant of pore formation in the membranes of vesicles, firstly the time course of the fraction of intact GUVs without pore formation among all of the examined GUVs, $P_{\text{intact}}(t)$, is determined. It is basically indicating the fraction of GUVs that are still intact after time " t " and is defined as $P_{\text{intact}}(t) = 1 - P_{\text{pore}}(t)$, where $P_{\text{pore}}(t)$ is the probability of pore formation. If 18 single GUVs are measured at $\sigma_c = 5.75$ mN/m in which 9 GUVs are formed pore, $P_{\text{intact}}(t) = 1 - P_{\text{pore}}(t) = 1 - 9/18 = 0.5$. The $P_{\text{intact}}(t)$ vs time graph is well fitted by the following single-exponential decay function (Fig. 4.3):

$$P_{\text{intact}}(t) = \exp(-k_p t) \quad (4.1)$$

where, k_p is the rate constant of pore formation in the membranes of GUVs and t is the period of time for applying the electric pulses in GUVs (tension was ongoing at $t = 0$). It is the rate of transition from the intact state to the pore state of vesicles in the presence of electrical tension.

In Fig.4.3 (a) and (b) the time dependent P_{intact} graph for two independent experiments are shown where the solid lines indicate the theoretical fitting of equation 4.1. From this curve the value of rate constant can be determined. The value of rate constant for two independent experiments are shown in table. 4.2.

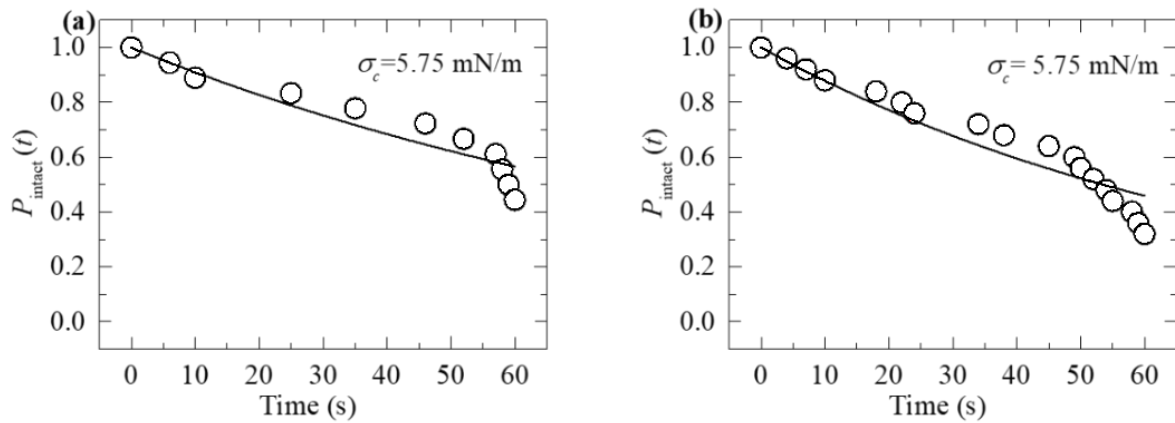


Fig 4.3 The time course of P_{intact} for 20%DOPG/80%DOPC-GUVs at 5.75 mN/m for (a) 1st independent experiment (b) 2nd independent experiment. The solid line in (a) and (b) is the theoretical fitting equation (4.1).

Table. 4.2: Rate constant of two independent experiment for 20%DOPG/80%DOPC-GUVs at tension 5.75 mN/m.

Rate constant, k_p (s^{-1})		
1 st independent experiment	2 nd independent experiment	Average
1.01×10^{-2}	1.29×10^{-2}	$(1.1 \pm 0.2) \times 10^{-2}$

4.4 Pore Formation in 20%DOPG/80%DOPC-GUVs at 6.5 mN/m

Again, the electroporation in 20%DOPG/80%DOPC-GUVs was taken into consideration for tension 6.5mN/m. The first GUV observed for 6.5mN/m tension is shown in Fig.4.4 (a). After applying tension σ_c of a value of 6.5 mN/m for 60s on this GUV, the properties of this tension were detected. After seeing for some time, it was evident that the GUV was ruptured as shown in Fig.4.4 (a). The contrast in the image of GUV before and after applying electrical tension can be seen in Fig.4.4 (a) at 0s. Before applying the tension, the GUV was completely intact and had a spherical shape. As it can be observed from the Fig.4.4 (a) that the GUV was intact with spherical shape until time = 25 s in the existence of σ_c . But at time 26s the GUV started to rupture and at time 27s the GUV fully loses its spherical shape and completely disappears. The red bar indicates the radius of the GUV.

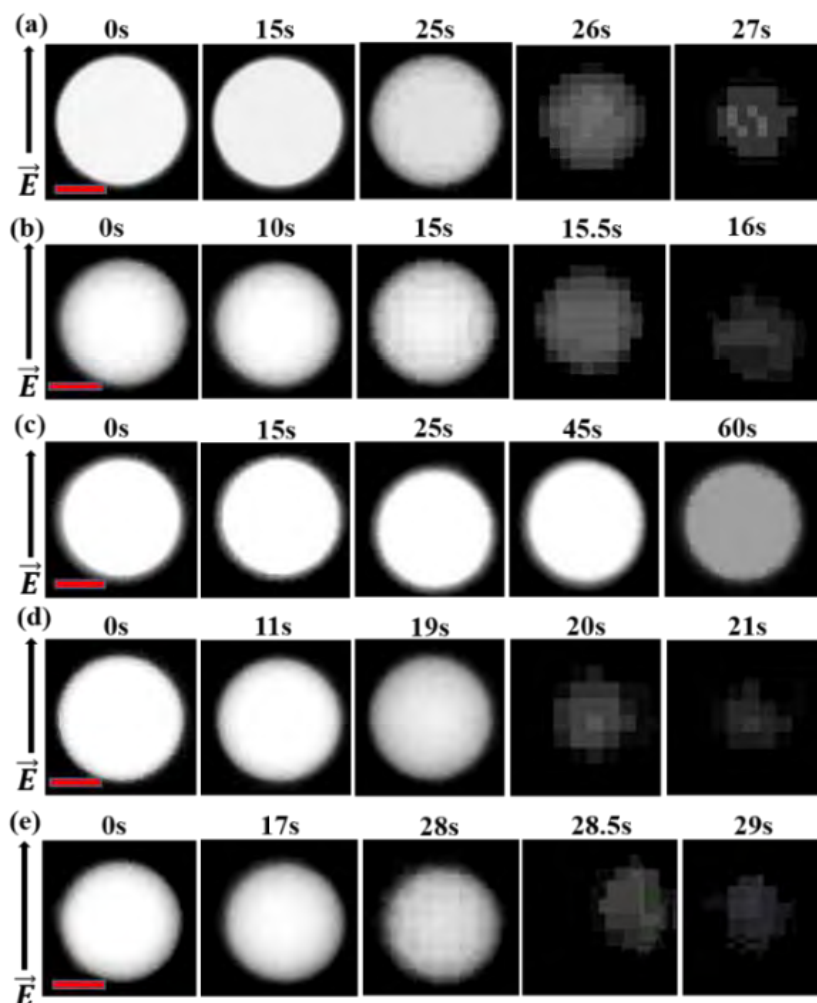


Fig. 4.4 Pore formation of (a) 1st (b) 2nd (c) 3rd (d) 4th and (e) 5th single 20%DOPG/80%DOPC-GUVs at 6.5 mN/m. The scale bar corresponds to a length of 15 μm .

In the similar way, the pore formation for 2nd, 3rd, 4th and 5th GUV are observed which is shown in Fig.4.4 (b-e). Among which the 3rd GUV didn't rupture. The 2nd, 4th and 5th GUV ruptured at 16s, 21s and 29s respectively.

4.5 Probability of Pore Formation in 20%DOPG/80%DOPC-GUVs at 6.5 mN/m

As described in section 4.2, pore formation in the membranes of many single 20%DOPG/80%DOPC-GUVs at tension 6.5 mN/m has been investigated. By using the expression as $P_{\text{intact}}(t) = 1 - P_{\text{pore}}(t)$, which indicates the probability of pore formation, the value of the $P_{\text{pore}}(t)$ for two independent experiments are found. For example, for the first independent experiment 18 single GUV were observed at tension 6.5 mN/m in which 12

GUVs were ruptured so the $P_{\text{pore}}(t) = 1-6/18 = 0.72$ and the second independent experiment 18 single GUV were observed at tension 6.5 mN/m in which 13 GUVs were pored so $P_{\text{pore}}(t) = 1-5/18 = 0.78$. The Time of pore formation for several 20%DOPG/80%DOPC-GUVs at tension 6.5 mN/m for two independent experiments is shown in table. 4.3.

Table. 4.3: Time of pore formation for several 20%DOPG/80%DOPC-GUVs at tension 6.5 mN/m for two independent experiments.

First independent experiment			Second independent experiment		
GUV-label number (n)	Times of pore formation (s)	P_{pore} (60s)	GUV-label number (n)	Times of pore formation (s)	P_{pore} (60s)
1	25	0.72	1	27	0.78
2	Intact		2	Intact	
3	19		3	17	
4	17		4	40	
5	40		5	21	
6	Intact		6	Intact	
7	22		7	10	
8	21		8	6	
9	Intact		9	Intact	
10	10		10	15	
11	8		11	35	
12	15		12	Intact	
13	Intact		13	12	
14	35		14	43	
15	Intact		15	3	
16	30		16	Intact	
17	44		17	31	
18	Intact		18	33	

In Fig.4.5 (a) and (b) the pore formation of 18 GUVs for constant tension 6.5 mN/m shown for two independent experiments. Here the concentration of DOPG/DOPC is 20%DOPG/80%DOPC at salt concentration 162 mM.

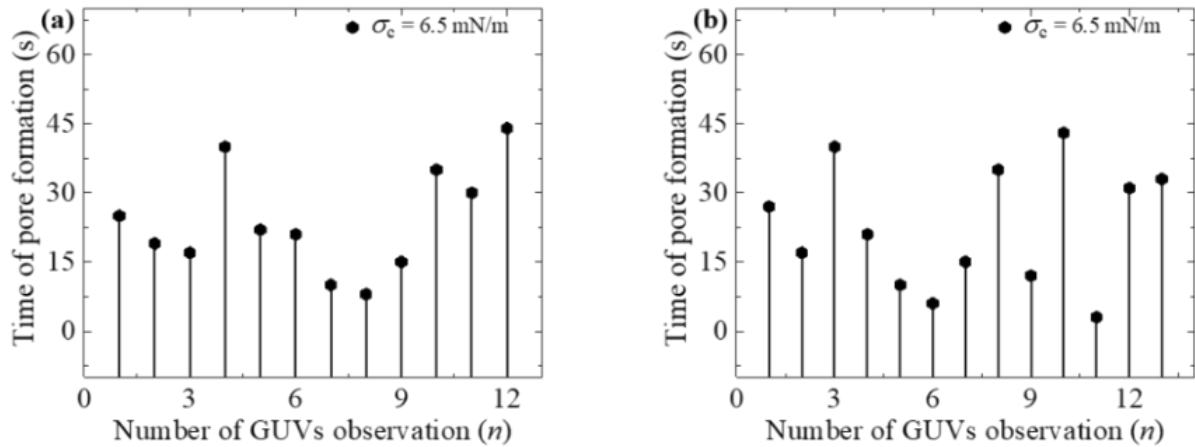


Fig. 4.5 Stochastic pore formation for 20%DOPG/80%DOPC-GUVs at 6.5mN/m for (a) 1st independent experiment and (b) 2nd independent experiment.

4.6 Rate Constant Pore Formation in 20%DOPG/80%DOPC-GUVs at 6.5 mN/m

By using equation 4.1 the rate constant, k_p can be determined for 6.5 mN/m in $C=162$ mM for 20%DOPG/80%DOPC-GUVs. The time course fraction of intact GUVs for two independent experiment is shown in Fig. 4.6. The rate constant for two independent experiment is shown in table. 4.4.

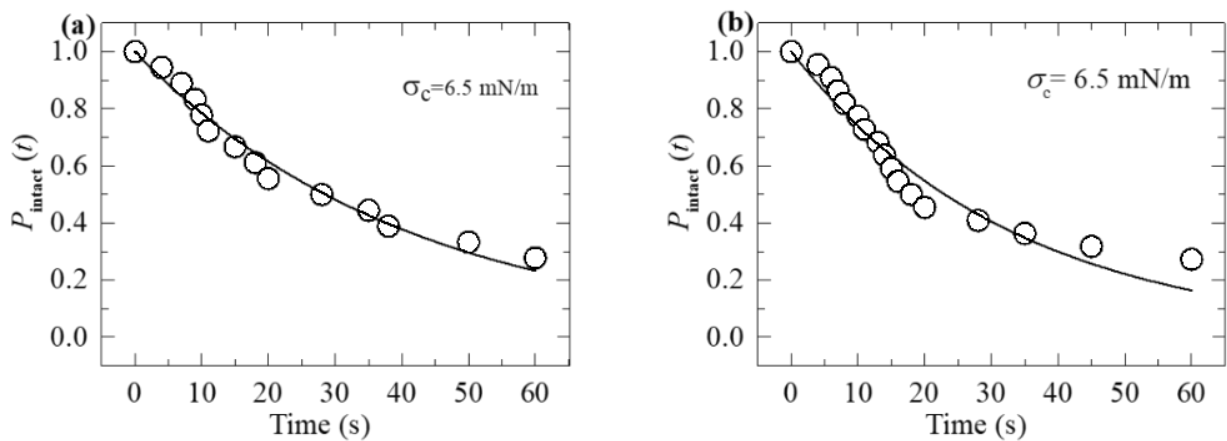


Fig. 4.6 The time course of P_{intact} for 20%DOPG/80%DOPC-GUVs at 6.5 mN/m for (a) 1st independent experiment (b) 2nd independent experiment. The solid line in (a) and (b) is the theoretical fitting equation (4.1).

Table. 4.4: Rate constant of two independent experiments at tension 6.5 mN/m for 20%DOPG/80%DOPC-GUVs.

Rate constant, k_p (s^{-1})		
1 st independent experiment	2 nd independent experiment	Average
3.01×10^{-2}	2.43×10^{-2}	$(2.7 \pm 0.3) \times 10^{-2}$

4.7 Pore Formation in 20%DOPG/80%DOPC-GUVs at 7.25 mN/m

The effect of surface charge density on the electroporation in 20%DOPG/80%DOPC GUVs is studied at 7.25 mN/m using 162 mM salt concentration. After applying tension 6.5mN/m on a single GUV and waiting for 60 s, the effect of surface charge density is observed. The GUV is shown in Fig. 4.7 (a). At 0s i.e. before applying the tension the GUV was completely intact. It maintained its shape till 7s. Then at 7.5s it suddenly lost its ruptured. At 8s it completely vanished.

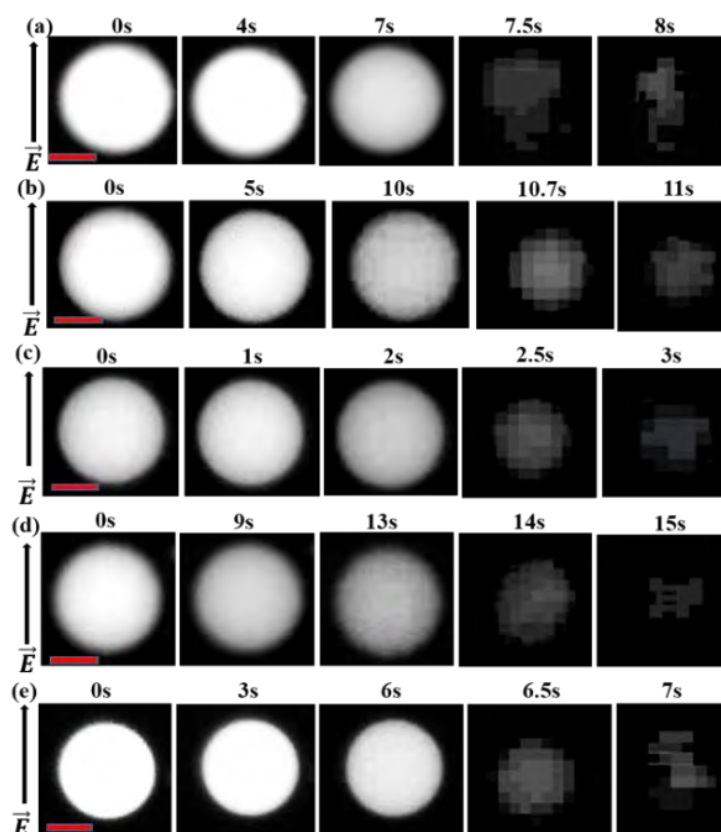


Fig. 4.7 Pore formation of (a) 1st (b) 2nd (c) 3rd (d) 4th and (e) 5th single 20%DOPG/80%DOPC-GUVs at 7.25 mN/m. Here, the scale bar corresponds to a length of 15 μ m.

Similarly, the pore formation for 2nd, 3rd, 4th and 5th GUV are observed at 11s, 3s, 15s and 7s respectively. They are shown in Fig 4.7 (b-e) respectively.

4.8 Probability of Pore Formation in 20%DOPG/80%DOPC-GUVs at 7.25 mN/m

As described in section 4.2, pore formation in the membranes of many single 20%DOPG/80%DOPC-GUVs at tension 7.25 mN/m has been investigated. By using the expression as $P_{\text{intact}}(t) = 1 - P_{\text{pore}}(t)$, which indicates the probability of pore formation, the value of the $P_{\text{pore}}(t)$ for two independent experiments are found. For example, for the first independent experiment 19 single GUV were observed at tension 7.25 mN/m in which 19 GUVs were ruptured so the $P_{\text{pore}}(t) = 1 - 0/19 = 1$ and the second independent experiment 17 single GUV were observed at tension 7.25 mN/m in which 13 GUVs were pored so $P_{\text{pore}}(t) = 1 - 0/17 = 1$. The time of pore formation for several 20%DOPG/80%DOPC-GUVs at tension 7.25 mN/m for two independent experiments is shown in table. 4.5.

Table. 4.5: Time of pore formation for several 20%DOPG/80%DOPC-GUVs at tension 7.25 mN/m for two independent experiments.

First independent experiment			Second independent experiment			
GUV-label number (n)	Times of pore formation (s)	P_{pore} (60s)	GUV-label number	Times of pore formation (s)	P_{pore} (60s)	
1	7	1	1	10	1	
2	10		2	15		
3	8		3	18		
4	7		4	5		
5	5		5	6		
6	13		6	8		
7	2		7	2		
8	14		8	9		
9	11		9	20		
10	3		10	18		
11	4		11	8		
12	9		12	15		
13	17		13	3		
14	7		14	9		
15	2		15	7		
16	9		16	7		
17	14		17	3		
18	19					

In Fig.4.8 (a) and (b) the pore formation of 18 GUVs for experiment-1 and 17 GUVs for experiment-2 at constant tension 7.25 mN/m are shown for two independent experiments. Here, the 20%DOPG/80%DOPC at salt concentration 162 mM is considered.

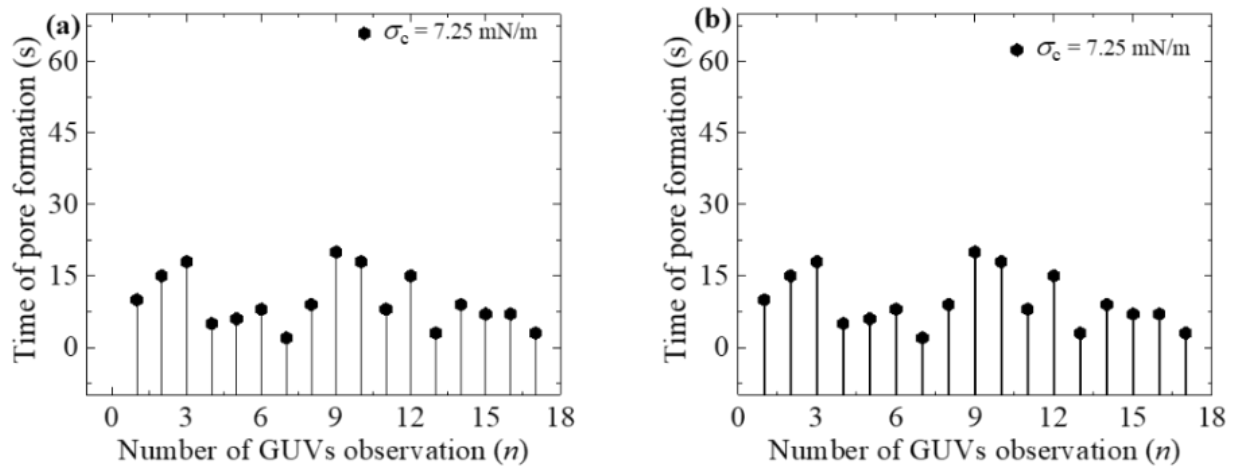


Fig. 4.8 Stochastic pore formation for 20%DOPG/80%DOPC-GUVs at 7.25 mN/m for (a) 1st independent experiment and (b) 2nd independent experiment.

4.9 Rate Constant Pore Formation in 20%DOPG/80%DOPC-GUVs at 7.25 mN/m

By using the equation 4.1 the P_{intact} can be determined for 7.25 mN/m in $C=162 \text{ mM}$ for 20%DOPG/80%DOPC-GUVs. The time course fraction of intact GUVs for two independent experiment is shown in Fig. 4.9. The rate constant for two independent experiment is shown in table. 4.6.

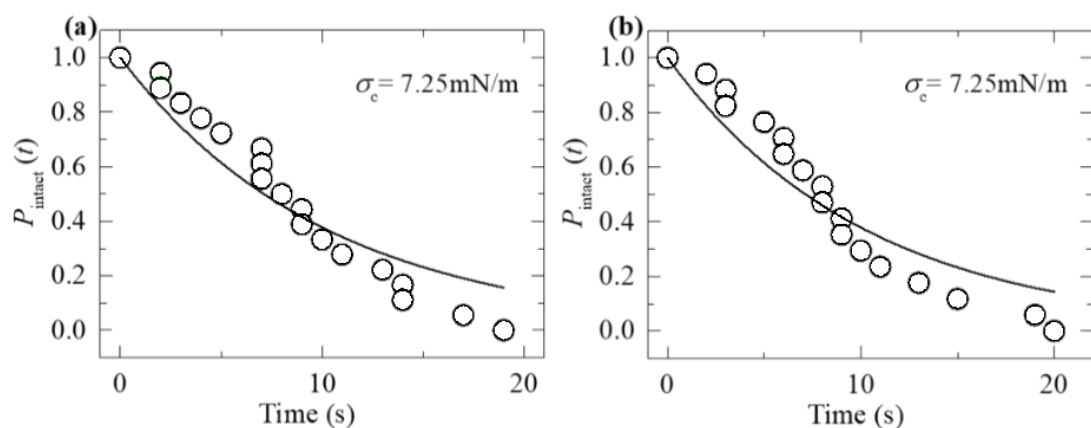


Fig. 4.9 The time course of P_{intact} at 7.25 mN/m for (a) 1st independent experiment (b) 2nd independent experiment. The solid line in (a) and (b) is the theoretical fitting equation (4.1).

Table. 4.6: Rate constant of two independent experiments at tension 7.25 mN/m for 20%DOPG/80%DOPC-GUVs.

Rate constant, k_p (s^{-1})		
1 st independent experiment	2 nd independent experiment	Average
0.98×10^{-1}	1.01×10^{-1}	$(1.0 \pm 0.01) \times 10^{-1}$

4.10 Theoretical Aspect of the Probability of Pore Formation and the Rate Constant of Pore Formation

It was studied before that, at equilibrium condition the membrane is tension free in the absence of electric field [106]. When external electric field is applied in the membrane, it induces a lateral electrical tension in the membrane ($\sigma = \sigma_c$). As a result, the membrane gets stretched. It is generally considered that the lateral density of lipid molecules in membranes is always exists due to their local thermal fluctuations. The region where the lateral density of lipid molecules is lower than the average is defined as a prepore in the membranes of GUVs [107-108]. Here the toroidal structure of a hydrophilic prepore is considered in which the outer and inner monolayers bend and merge in a pore with an inner wall composed of lipid head groups [109-110]. Hence, the surface of its wall is charged due to the presence of charged lipid head groups. If a prepore with radius r is created in the membrane, the total free energy of the system changes by an additional free energy that contains two terms: one is σ_c which favoring the expansion of a prepore, and the other is line tension (Γ) (the line energy per unit length of a prepore) which favoring the closure of a prepore. The free energy of a prepore can be expressed as [110] $U(r, \sigma_c) = 2\pi r\Gamma - \pi r^2\sigma_c$. In the presence of electrostatic interactions (B) the free energy of a prepore can be written as follows,

$$U(r, \sigma_c, B) = 2\pi \Gamma r - \pi r^2(\sigma_c + B) \quad (4.2)$$

B is defined as follow [110].

$$B \approx \left\{ 4\Omega \left[\frac{1-q}{p} + \ln(p+q) \right] \frac{k_B T}{e} - \frac{\Omega^2}{\varepsilon_w \varepsilon_0} \omega^2 \frac{h}{2} \right\} \quad (4.3)$$

where h is the height of a prepore (~ 4 nm), Ω is the membrane surface charge density, ε_w is the relative dielectric constant of water, ε_0 is the permittivity of free space,

$p = 2\pi\lambda_B X / \kappa A_0$ and $q = \sqrt{1 + p^2}$, $1/\kappa$ is the Debye length, A_0 is the cross-sectional area of DOPG under no electrical tension, λ_B is the Bjerrum length in water, $\lambda_B = e^2 / 4\pi k_B T \epsilon_0 \epsilon_W = 0.716$ nm at 25 °C, k_B is the Boltzmann constant, T is the absolute temperature, and ω is the fitting parameter which is the ratio of the surface charge density on the prepore wall to that of the GUV surface. From equation (4.2), at the critical radius of a prepore, $r = r_c = \frac{\Gamma}{\sigma_c + B}$, the energy barrier of the prepore free

$$\text{energy, } U_b(r, \sigma_c, B) = \frac{\pi\Gamma^2}{\sigma_c + B}.$$

According to the Kramers theory of Brownian motion [111-112], the expansion of a prepore is treated as a particle in stochastic motion in r -space within an asymmetric double-well potential $U(r)$. The well has an infinite barrier at $r = 0$ act as a reflecting boundary and a controlled barrier at $r = r_b$ act as an absorbing boundary. The lifetime of intact GUV, τ , is defined as the time when the particle arrives at r_b and discharges from the hole, which is determined by the mean earliest passage time method as follows [113-114]:

$$\tau = \left(\frac{1}{D_r} \right) \int_0^{r_b} \exp[U(r)/k_B T] \left\{ \int_0^r \exp[-U(z)/k_B T] dz \right\} dr \quad (4.4)$$

Where diffusion coefficient of the particle in r -phase space is D_r . After some mathematical simplifications the k_p can be expressed as follows [16,114].

$$k_p = \frac{1}{\tau} = A_F (\sigma_c + B) \exp \left[-\frac{\pi\Gamma^2}{k_B T (\sigma_c + B)} \right] \quad (4.5)$$

Where, $A_F = \left(\frac{D_r \sqrt{3}}{k_B T} \right)$ is the pre-exponential factor and A_F and Γ are the fitting parameters. By changing these two parameters, equation (4.5) is fitted to experimental rate constant data (Fig. 4.4). The fraction of GUVs with pores, among all the examined GUVs at $t = 60$ s is as follows [16]

$$P_{\text{pore}}(\sigma_c, 60 \text{ s}) = \int_0^{60} f_{\text{pore}}(t) dt = 1 - \exp(-60k_p) \quad (4.6)$$

4.11 Dependence of $P_{\text{pore}}(60 \text{ s})$ on σ_c for 20%DOPG/80%DOPC-GUVs

The probability of pore formation, $P_{\text{pore}}(t = 60 \text{ s})$, is calculated for 20%DOPG/80%DOPC-GUVs at salt concentration 162 mM by varying the σ_c . It indicates the fraction of GUVs with pores, among all the examined GUVs at a particular time (i.e. 60 s). Fig. 4.10 and table. 4.7 show the $P_{\text{pore}}(60\text{s})$ at different σ_c .

Table. 4.7: The dependence of P_{pore} on σ_c using $X = 0.20$.

DOPG mole fraction, X	Tension, σ_c (mN/m)	$P_{\text{pore}}(60\text{s})$
0.20	3	0
	4	$(0.52 \pm 0.006) \times 10^{-1}$
	4.5	$(0.69 \pm 0.028) \times 10^{-1}$
	5.0	$(1.2 \pm 0.007) \times 10^{-1}$
	5.75	$(5.4 \pm 0.087) \times 10^{-1}$
	6.5	$(8.8 \pm 0.092) \times 10^{-1}$
	7.25	1

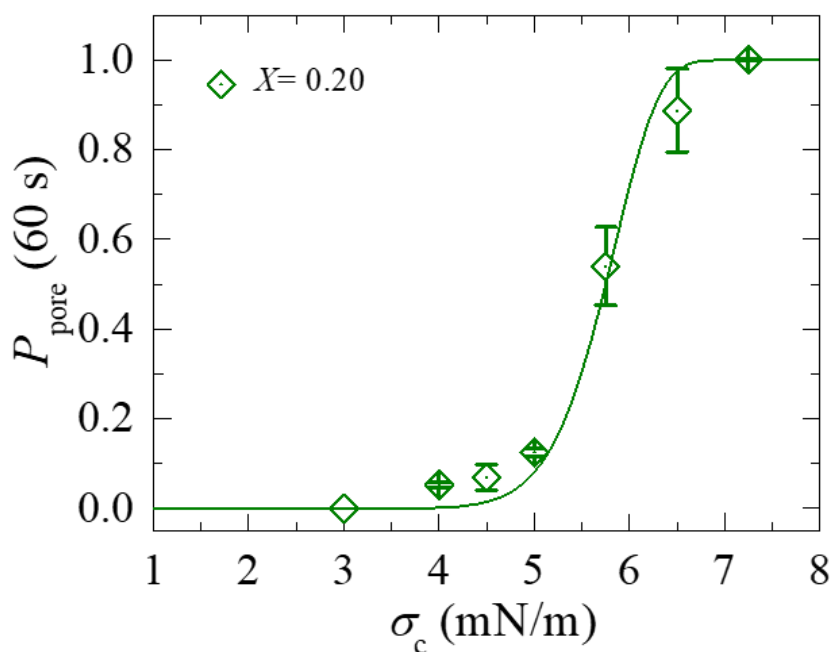


Fig. 4.10 The fitted curve for P_{pore} and σ_c at 20%DOPG/80%DOPC-GUVs. The solid lines show the best fitted theoretical curves corresponding to equation (4.6) with k_p as used in Fig. 4.11 according to equation (4.5).

4.12 Dependence of Rate Constant of Pore Formation on σ_c for 20%DOPG/80%DOPC-GUVs

Fig. 4.11 and table. 4.8 show the σ_c dependent k_p values for $C = 162$ mM using $X = 0.20$. In the systems, the value of k_p increases with the increase of σ_c . The experimental results of σ_c vs k_p is fitted with the theoretical equation (eq. 4.5) and obtained the line tension of membranes. The solid lines show the best fitted theoretical curves corresponding to equation (4.5).

Table. 4.8: The σ_c dependent k_p values using $X = 0.20$.

DOPG mole fraction, X	Tension, σ_c (mN/m)	Rate Constant, k_p (s^{-1})
0.20	5.75	$(1.1 \pm 0.2) \times 10^{-2}$
	6.5	$(2.7 \pm 0.3) \times 10^{-2}$
	7.25	$(10.1 \pm 0.01) \times 10^{-2}$

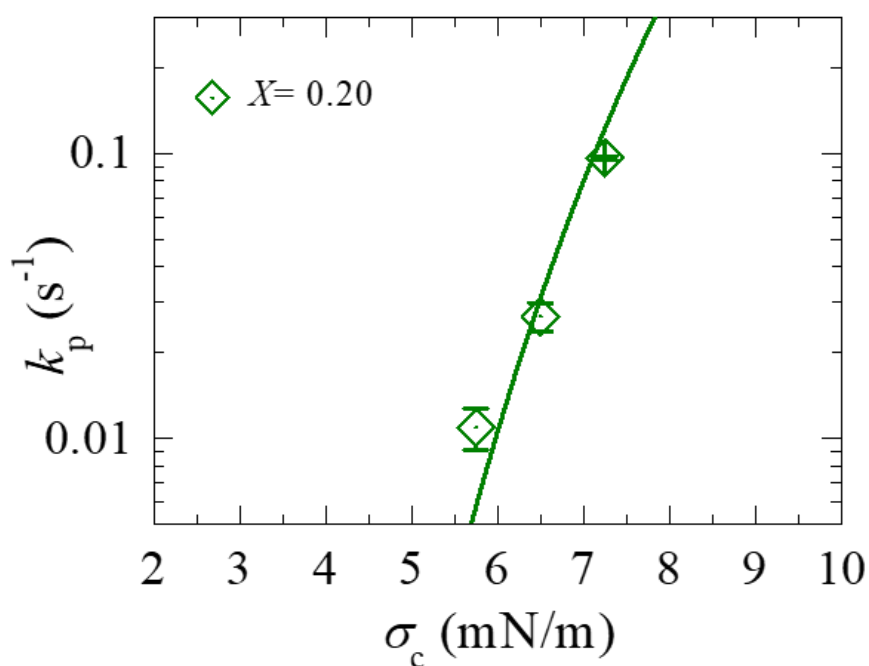


Fig. 4.11 The tension dependent k_p for 20%DOPG/80%DOPC-GUVs. The solid lines show the best fitted theoretical curves corresponding to equation (4.5).

4.13 Pore Formation in 60%DOPG/40%DOPC-GUVs at 4.5 mN/m

The electroporation in 60%DOPG/40%DOPC-GUVs was taken into consideration. The tension of the membrane, σ_c of a value of 4.5 mN/m was applied for 60s on a ‘single GUV’ and the outcome of this tension was observed. After observing for some time, it was obvious that the GUV was broken all of a sudden as shown in Fig. 4.12 (a).

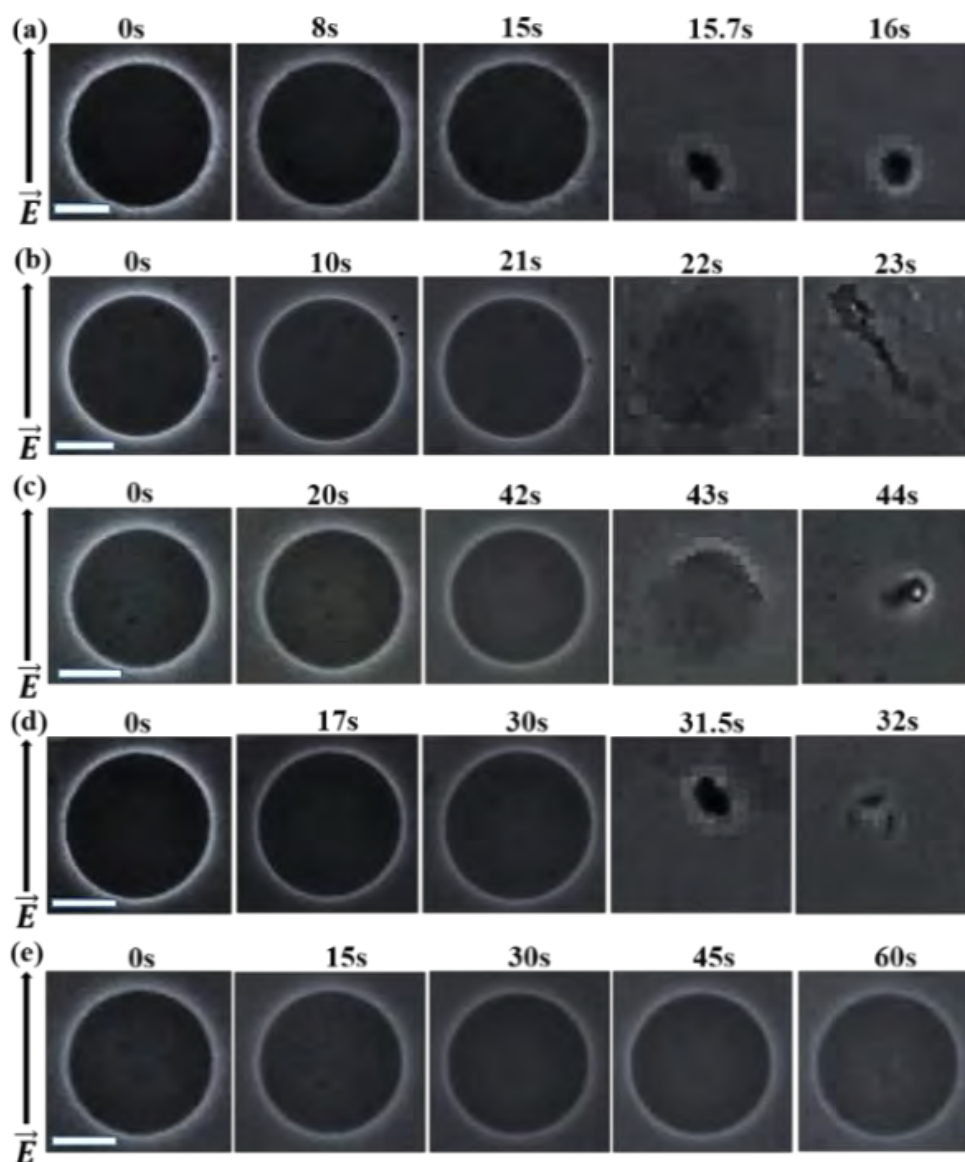


Fig. 4.12 Pore formation of (a) 1st (b) 2nd (c) 3rd (d) 4th and (e) 5th single 60%DOPG/40%DOPC-GUVs at 4.5 mN/m. Here, the scale bar corresponds to a length of 15 μm .

The contrast in the image of GUV before and after applying electrical tension can be seen in Fig.4.12 (a) at 0s. Before applying the tension, the GUV was completely intact and had a spherical shape. It can be observed from the Fig.4.12 (a) that the GUV was intact with spherical shape until time = 15 s in the presence of σ_c . But at time 15.7s the GUV started to rupture and at time 16s the GUV completely lost its spherical shape and permanently disappears.

The 2nd GUV was investigated at tension of 4.5 mN/m. In Fig. 4.12 (b) it is clear that the GUV was intact till 21s. It started losing its shape at 22s and completely vanished by 23s. The 3rd GUV taken into consideration also showed similar phenomenon. It was intact till first 42s. After 42s it gradually lost its shape at 43s and by 44s it totally lost its spherical shape and vanished. It is shown in Fig. 4.12 (c). The 4th GUV (Fig.4.12 (d)) considered for 60%DOPG/40%DOPC at a value of tension 4.5 mN/m also formed pore. It had its spherical shape till 30 sec. At 31.5s it lost its intact spherical shape and at 32s it entirely ruptured. The 5th observed GUV with the same parameters didn't rupture. This is shown in Fig. 4.12 (e).

4.14 Probability of Pore Formation in 60%DOPG/40%DOPC-GUVs at 4.5 mN/m

Pore formation in the membranes of many single 60%DOPG/40%DOPC-GUVs at tension 4.5 mN/m was investigated. The expression $P_{\text{intact}}(t) = 1 - P_{\text{pore}}(t)$, specifies the probability of pore formation. The value of the $P_{\text{pore}}(t)$ for two independent experiments are found. For example, for the first independent experiment 21 single GUV were observed at tension 4.5 mN/m in which 13 GUVs were ruptured so the $P_{\text{pore}}(t) = 13/21 = 0.62$ and the second independent experiment 19 single GUV were observed at tension 7.25 mN/m in which 12 GUVs were pored so $P_{\text{pore}}(t) = 12/19 = 0.63$. The time of pore formation for several 60%DOPG/40%DOPC-GUVs at tension 4.5 mN/m for two independent experiments are shown in table. 4.9.

Table. 4.9: Time of pore formation for several 60%DOPG/40%DOPC-GUVs at tension 4.5 mN/m for two independent experiments.

First independent experiment			Second independent experiment		
GUV-label number (n)	Times of pore formation (s)	P_{pore} (60s)	GUV-label number (n)	Times of pore formation (s)	P_{pore} (60s)
1	50	0.62	1	45	0.63
2	48		2	16	
3	Intact		3	21	
4	23		4	Intact	
5	Intact		5	Intact	
6	23		6	16	
7	Intact		7	16	
8	25		8	17	
9	56		9	18	
10	19		10	42	
11	Intact		11	50	
12	23		12	52	
13	12		13	Intact	
14	Intact		14	Intact	
15	26		15	Intact	
16	Intact		16	29	
17	28		17	21	
18	58		18	Intact	
19	35		19	Intact	
20	Intact				
21	Intact				

The time of pore formation for two independent experiment is shown in the table and Fig. 4.13 (a) and (b). Here, it is seen that the time of pore formation is different for different GUVs i.e. the pore occurs stochastically. This phenomenon is observed for 21 GUVs for 1st experiment and 19 GUVs for 2nd experiment.

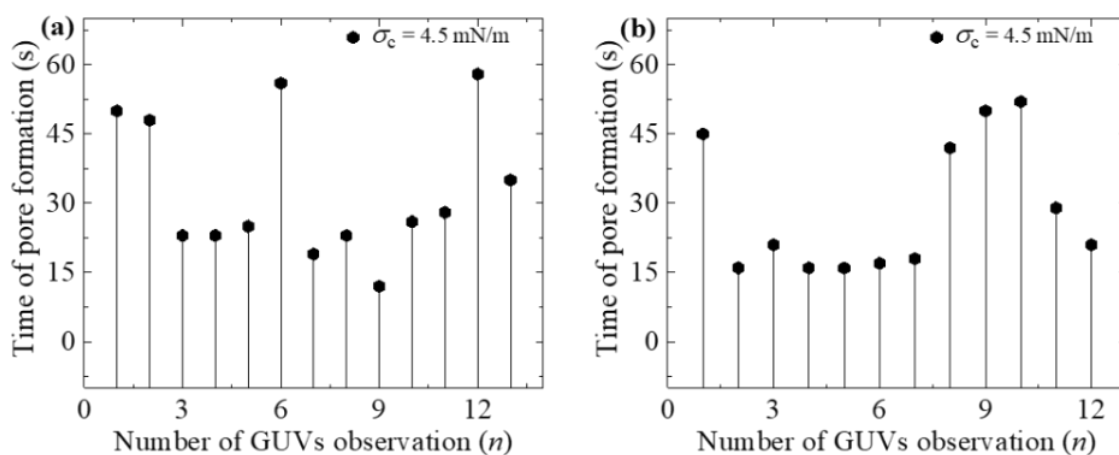


Fig. 4.13 Stochastic pore formation for 60%DOPG/40%DOPC-GUVs at 4.5 mN/m for (a) 1st independent experiment and (b) 2nd independent experiment.

4.15 Rate Constant Pore Formation in 60%DOPG/40%DOPC-GUVs at 4.5 mN/m

By using the equation 4.1 the P_{intact} can be determined for 4.5 mN/m in $C=162 \text{ mM}$ for 60%DOPG/40%DOPC. Fig. 4.14 show the P_{intact} vs time fitting curve. In table. 4.10, the rate constants for two independent experiments are shown.

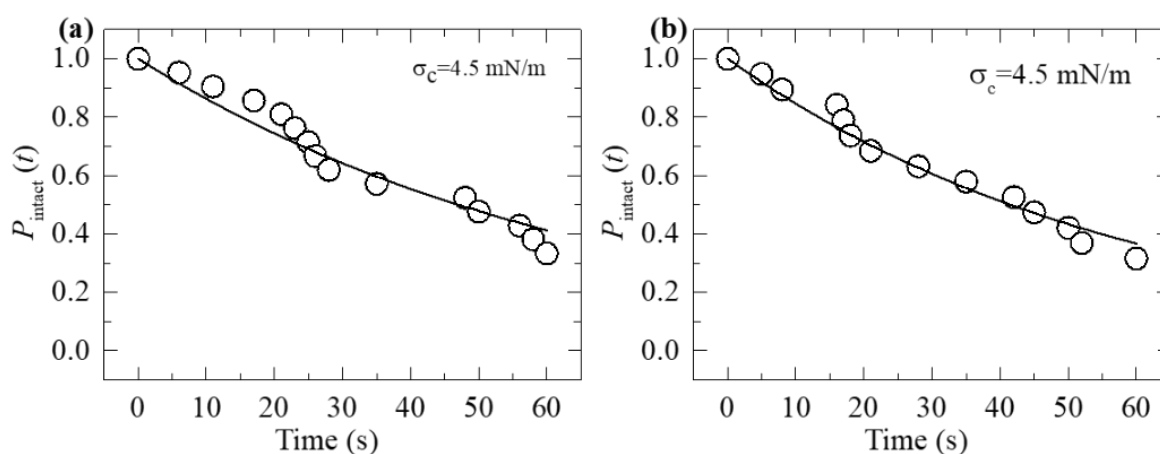


Fig. 4.14 The time course of P_{intact} for 60%DOPG/40%DOPC-GUVs at 4.5 mN/m for (a) 1st independent experiment (b) 2nd independent experiment. The solid line in (a) and (b) is the theoretical fitting equation (4.1).

Table. 4.10: Rate constant of two independent experiments at tension 4.5 mN/m for 60%DOPG/40%DOPC-GUVs.

Rate constant, k_p (s^{-1})		Average
1 st independent experiment	2 nd independent experiment	1.295×10^{-2}
1.24×10^{-2}	1.35×10^{-2}	

4.16 Pore Formation in 60%DOPG/40%DOPC-GUVs at 5.5 mN/m

Here, a single GUV was observed at first with 60%DOPG/40%DOPC concentration at 5.5 mN/m tension. Here this GUV ruptured after 15s. It was only intact for 15s after the tension was applied and lost its shape at 15.5s and by 16s it was completely gone. Here, the white bar indicates the radius of the GUV. In Fig. 4.15 (a) this process is shown.

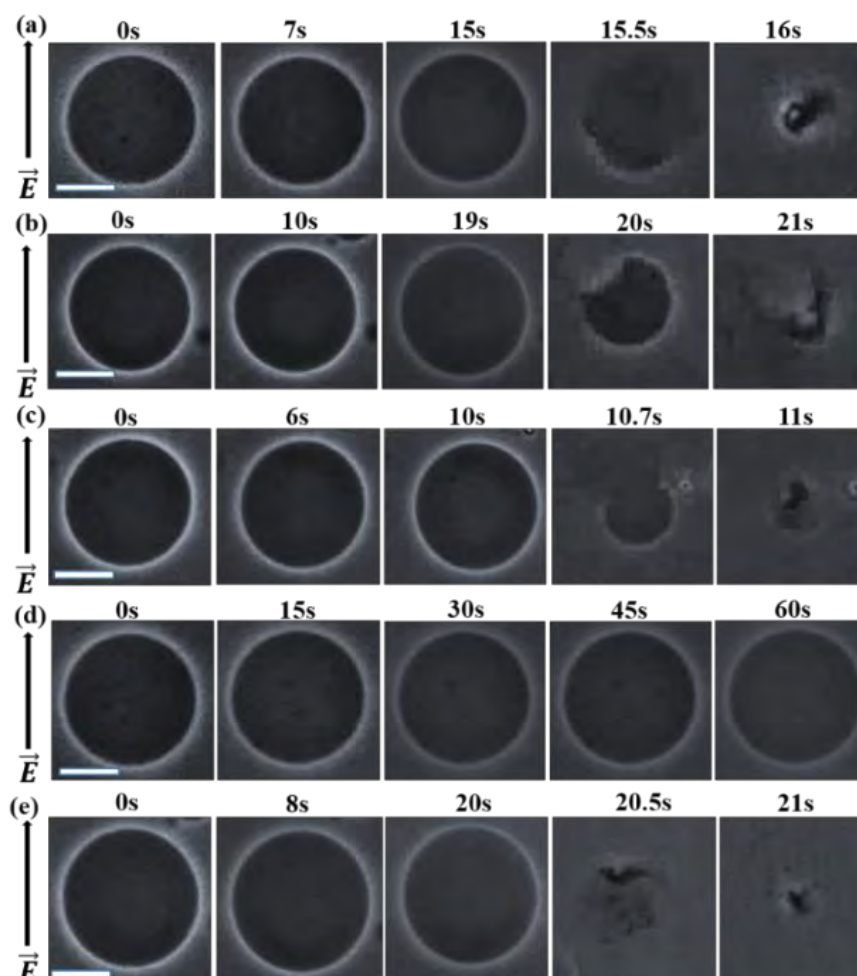


Fig. 4.15 Pore formation of (a) 1st (b) 2nd (c) 3rd (d) 4th and (e) 5th single 60%DOPG/40%DOPC -GUVs at 5.5 mN/m. Here, the scale bar corresponds to a length of 15 μm .

In a similar way, rupture for 2nd, 3rd, 4th and 5th GUV is shown in Fig. 4.15 (b-e). Among these GUVs the 4th GUV didn't rupture (Fig. 4.15 (d)). The 2nd, 3rd and 5th GUV ruptured at 21s, 11s and 21s respectively.

4.17 Probability of Pore Formation in 60%DOPG/40%DOPC-GUVs at 5.5 mN/m

Pore formation in the membranes of many single 60%DOPG/40%DOPC-GUVs at tension 5.5 mN/m was studied. The expression $P_{\text{intact}}(t) = 1 - P_{\text{pore}}(t)$, specifies the probability of pore formation. The value of the $P_{\text{pore}}(t)$ for two independent experiments are found. For example, for the first independent experiment 18 single GUV were observed at tension 5.5 mN/m in which 15 GUVs were ruptured so the $P_{\text{pore}}(t) = 1 - 3/18 = 0.83$ and the second independent experiment 20 single GUV were observed at tension 5.5mN/m in which 15 GUVs were pored so $P_{\text{pore}}(t) = 1 - 5/20 = 0.75$.

Table. 4.11: Time of pore formation for several 60%DOPG/40%DOPC-GUVs at tension 5.5 mN/m for two independent experiments.

First independent experiment			Second independent experiment		
GUV-label number (n)	Times of pore formation (s)	P_{pore} (60s)	GUV-label number (n)	Times of pore formation (s)	P_{pore} (60s)
1	8	0.83	1	8	0.75
2	8		2	10	
3	25		3	12	
4	Intact		4	2	
5	7		5	5	
6	Intact		6	10	
7	7		7	19	
8	8		8	4	
9	9		9	51	
10	11		10	Intact	
11	10		11	20	
12	3		12	Intact	
13	10		13	16	
14	53		14	9	
15	13		15	14	
16	6		16	18	
17	Intact		17	4	
18	13		18	Intact	
		19	Intact		
		20	Intact		

The time of pore formation for two independent experiment is shown in the table. 4.11 and Fig. 4.16 (a) and (b). Here, it is seen that the time of pore formation is different for different GUVs i.e. the pore occurs stochastically. This phenomenon is observed for 18 GUVs for 1st experiment and 20 GUVs for 2nd experiment.

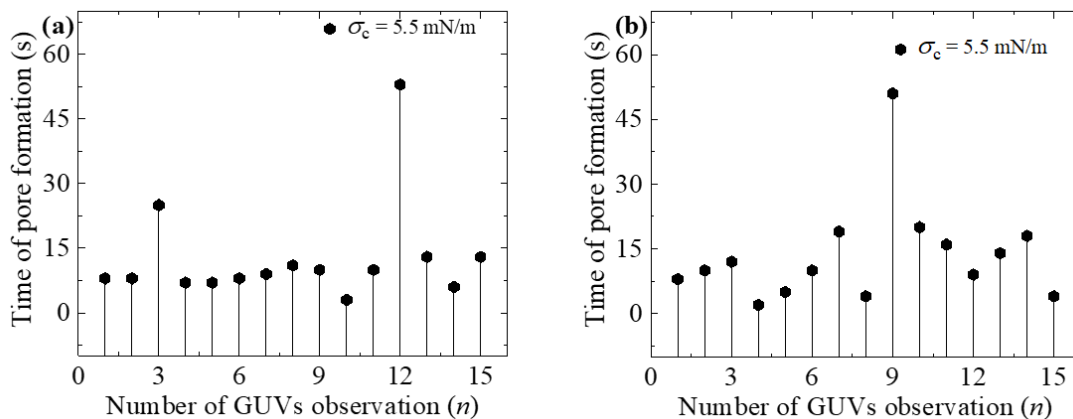


Fig. 4.16 Stochastic pore formation in 60%DOPG/40%DOPC-GUVs at 5.5 mN/m for (a) 1st independent experiment and (b) 2nd independent experiment.

4.18 Rate Constant Pore Formation in 60%DOPG/40%DOPC-GUVs at 5.5 mN/m

By using the equation 4.1 the P_{intact} can be determined for 5.5 mN/m in $C=162$ mM for 60%DOPG/40%DOPC. The fitting curve of P_{intact} for two independent experiment is shown in Fig. 4.17. The rate constant of two independent experiments at tension 5.5 mN/m for 60%DOPG/40%DOPC-GUVs is shown in table. 4.12.

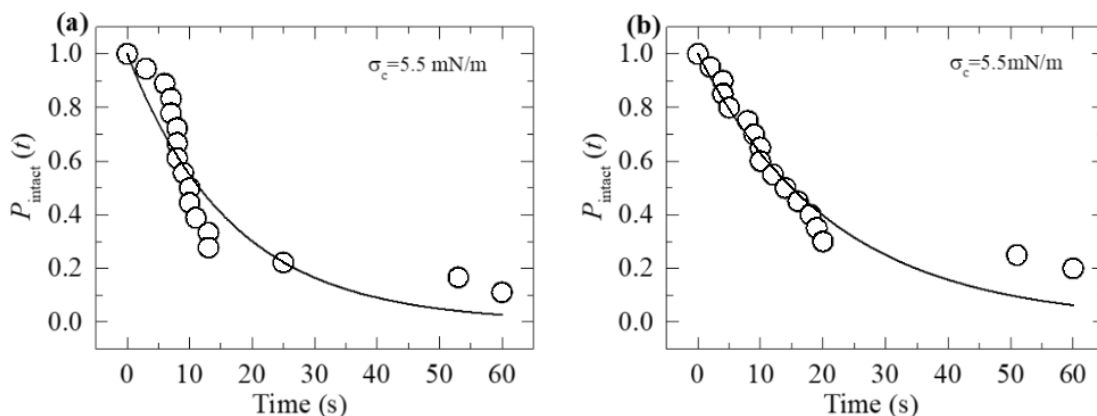


Fig. 4.17 The time course of P_{intact} in 60%DOPG/40%DOPC-GUVs at 5.5 mN/m for (a) 1st independent experiment (b) 2nd independent experiment. The solid line in (a) and (b) is the theoretical fitting equation (4.1).

Table. 4.12: Rate constant of two independent experiments at tension 5.5 mN/m for 60%DOPG/40%DOPC-GUVs.

Rate constant, k_p (s^{-1})		Average
1 st independent experiment	2 nd independent experiment	5.72×10^{-2}
5.81×10^{-2}	5.63×10^{-2}	

4.19 Pore Formation in 60%DOPG/40%DOPC-GUVs at 6.0 mN/m

By using the phase contrast microscope, the process of pore formation for a single GUV at 60%DOPG/40%DOPC at 6.0 mN/m tension is observed. It was intact till 5s. At 6s it ruptured and at 7s it was completely destroyed. This is shown in Fig. 4.18 (a). The white bar indicates the radius of the GUV.

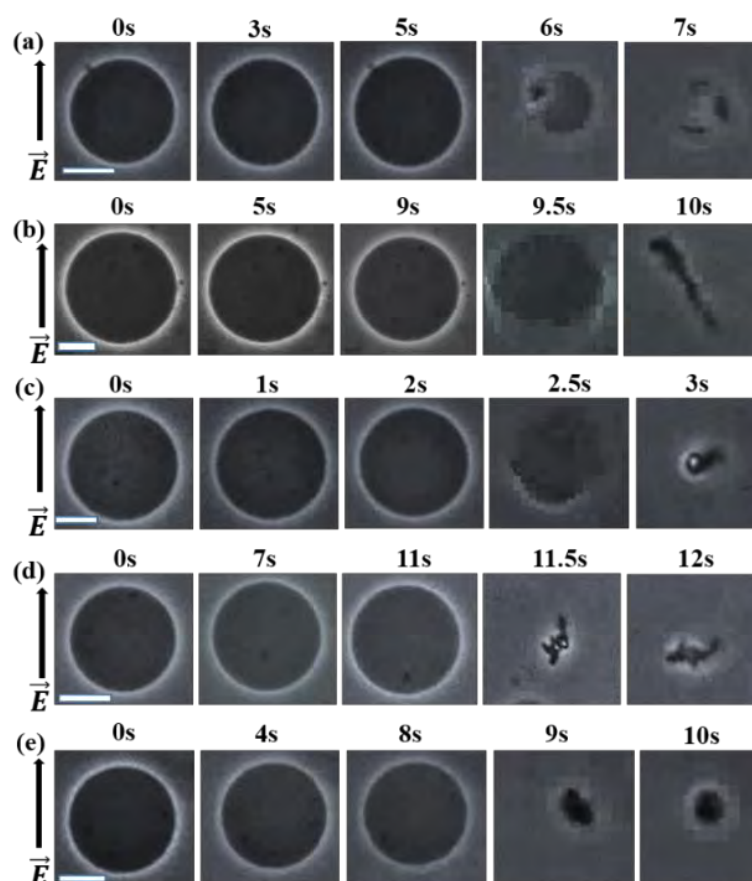


Fig. 4.18 Pore formation of (a) 1st (b) 2nd (c) 3rd (d) 4th and (e) 5th single 60%DOPG/40%DOPC-GUVs at 6.0 mN/m. Here, the scale bar corresponds to a length of 15 μm .

Similarly, the 2nd, 3rd, 4th and 5th GUV ruptured at 10s, 3s, 12s and 10s respectively as shown in Fig. 4.18 (b-e). For 6mN/m tension at 60%DOPG/40%DOPC all the observed GUVs ruptured. And they ruptured within 20s.

4.20 Probability of Pore Formation in 60%DOPG/40%DOPC-GUVs at 6.0 mN/m

Pore formation in the membranes of 60%DOPG/40%DOPC-GUVs for many single GUVs at tension 5.5 mN/m was studied and shown in table. 4.13. The expression $P_{\text{intact}}(t) = 1 - P_{\text{pore}}(t)$, specifies the probability of pore formation. The value of the $P_{\text{pore}}(t)$ for two independent experiments are found. For example, for both independent experiments 17 single GUVs were observed at tension 6.0 mN/m in which 17 GUVs were ruptured so the $P_{\text{pore}}(t) = 1 - 0/17 = 1$

Table. 4.13: Time of pore formation for several 60%DOPG/40%DOPC-GUVs at tension 6.0 mN/m for two independent experiments.

First independent experiment			Second independent experiment		
GUV-label number (n)	Times of pore formation (s)	P_{pore} (60s)	GUV-label number (n)	Times of pore formation (s)	P_{pore} (60s)
1	8	1	1	3	1
2	5		2	5	
3	7		3	13	
4	10		4	15	
5	9		5	4	
6	3		6	8	
7	12		7	2	
8	6		8	12	
9	10		9	9	
10	9		10	19	
11	19		11	4	
12	4		12	9	
13	2		13	6	
14	15		14	7	
15	3		15	11	
16	7		16	17	
17	11		17	12	

Here the time of pore formation for 17 GUVs is shown. [It can be seen that, the GUVs from pore at different time. But in this case no GUV is intact after 60s. That's due to

high tension applied to the GUVs.

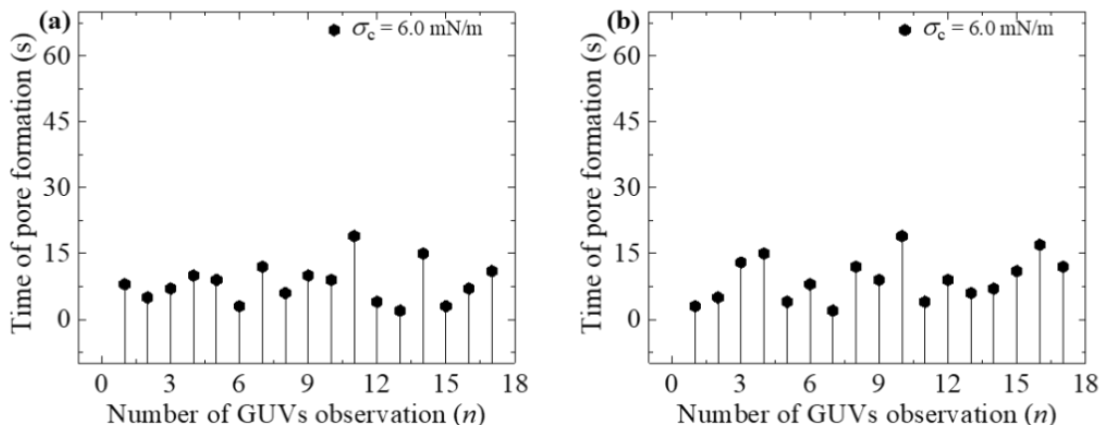


Fig. 4.19 Stochastic pore formation for 60%DOPG/40%DOPC-GUVs at 6.0 mN/m for (a) 1st independent experiment and (b) 2nd independent experiment.

4.21 Rate Constant Pore Formation in 60%DOPG/40%DOPC-GUVs at 6.0 mN/m

By using the equation 4.1 the P_{intact} can be determined for 6.0 mN/m in $C = 162$ mM for 60%DOPG/40%DOPC-GUVs. The fitting curve for time course of P_{intact} for two independent experiment is shown below. The value of rate constant for these two independent experiments are shown in the table. 4.14.

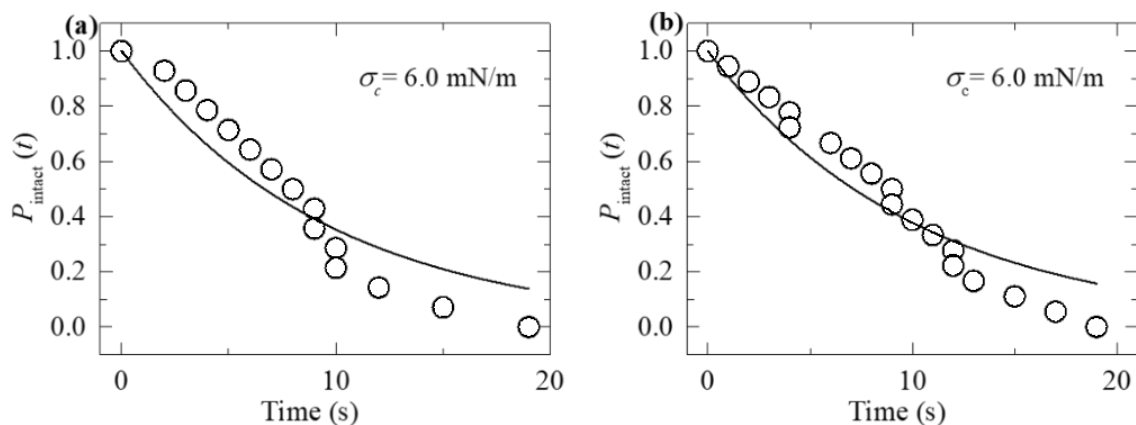


Fig. 4.20 The time course of P_{intact} at 6.0 mN/m for (a) 1st independent experiment (b) 2nd independent experiment. The solid line in (a) and (b) is the theoretical fitting equation (4.1).

Table. 4.14: The value of rate constant for two independent experiments at tension 6 mN/m for 60%DOPG/40%DOPC-GUVs.

Rate constant, k_p (s^{-1})		Average
1 st independent experiment	2 nd independent experiment	13.09×10^{-2}
12.4×10^{-2}	13.5×10^{-2}	

4. 22 Dependence of $P_{\text{pore}}(60 \text{ s})$ on σ_c for 60%DOPG/40%DOPC-GUVs

The probability of pore formation, $P_{\text{pore}}(t = 60 \text{ s})$, is calculated for surface charge density of 60%DOPG at salt concentration 162 mM by varying the σ_c . It indicates the fraction of GUVs with pores, among all the examined GUVs at a particular time (i.e. 60 s). Fig. 4.21 and table. 4.15 show the dependence of $P_{\text{pore}}(60 \text{ s})$ with σ_c for $C = 162 \text{ mM}$ using $X = 0.60$. The value of $P_{\text{pore}}(60 \text{ s})$ increases with the increase of σ_c and $P_{\text{pore}}(60 \text{ s}) = 1.0$ at and above $\sigma_c = 6.0 \text{ mN/m}$.

Table. 4.15: The dependence of P_{pore} on σ_c using $X = 0.60$.

DOPG mole fraction, X	Tension, σ_c (mN/m)	$P_{\text{pore}}(60\text{s})$
0.60	2	0
	2.5	$(0.91 \pm 0.005) \times 10^{-1}$
	3	$(1.3 \pm 0.093) \times 10^{-1}$
	4	$(3.8 \pm 0.071) \times 10^{-1}$
	4.5	$(6.7 \pm 0.008) \times 10^{-1}$
	5.5	$(8.2 \pm 0.012) \times 10^{-1}$
	6.0	1

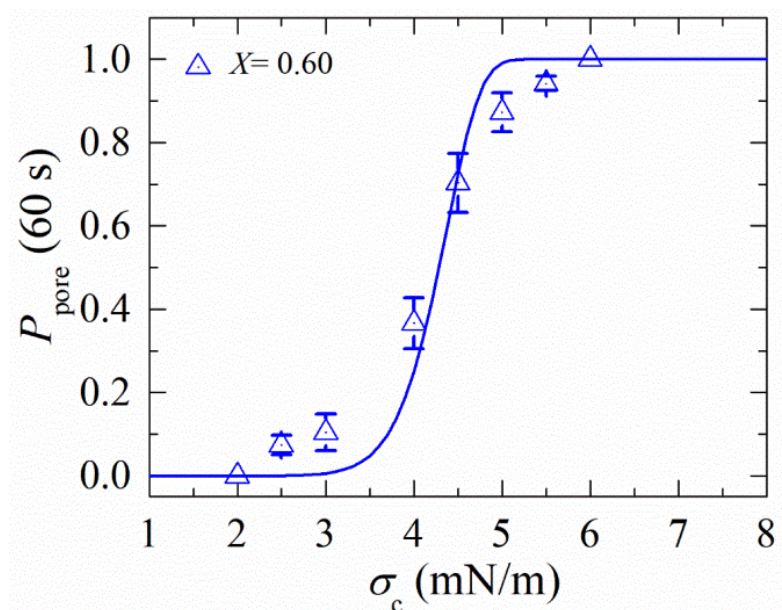


Fig. 4.21 The fitted curve of P_{pore} and σ_c for 60%DOPG/40%DOPC-GUVs. The solid lines show the best fitted theoretical curves corresponding to equation (4.6) with k_p as used in Fig. 4.22 according to equation (4.5).

4.23 Dependence of Rate Constant of Pore Formation on σ_c for 60%DOPG/40%DOPC-GUVs

Fig. 4.22 and table. 4.16 show the σ_c dependent k_p values for $C = 162$ mM using $X = 0.60$. In the systems, the value of k_p increases with the increase of σ_c . The experimental results of σ_c vs k_p is fitted with the theoretical equation (eq. 4.5) and obtained the line tension of membranes. It is now interesting to see how line tension changes for electrostatic effects.

Table. 4.16: The σ_c dependent k_p values using $X = 0.60$

DOPG mole fraction, X	Tension, σ_c (mN/m)	Rate constant, k_p (s^{-1})
0.60	4.5	$(1.3 \pm 0.2) \times 10^{-2}$
	5.5	$(5.7 \pm 0.1) \times 10^{-2}$
	6	$(14.02 \pm 0.2) \times 10^{-2}$

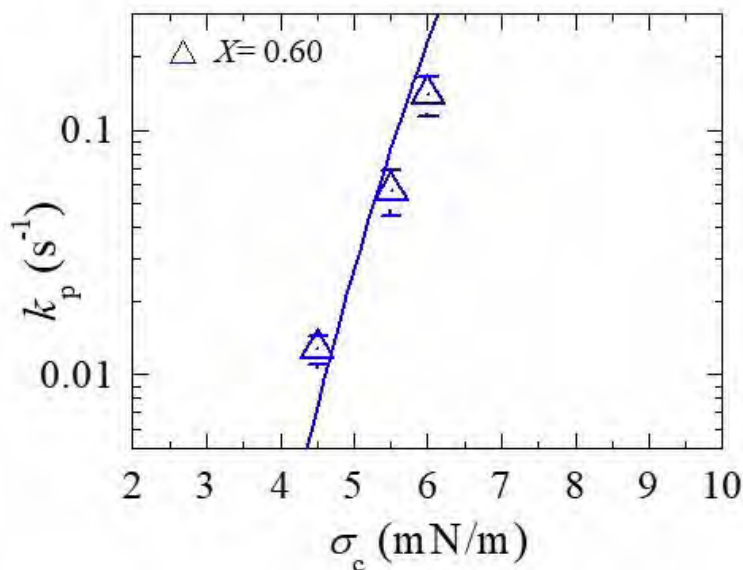


Fig. 4.22 The tension dependent k_p for 60%DOPG/40%DOPC-GUVs. The solid lines show the best fitted theoretical curves corresponding to equation (4.5).

4.24 Dependence of P_{pore} (60 s) on σ_c at Various DOPG/DOPC- GUVs

The probability of pore formation also depends on the surface charge density. The surface charge density (determined by X) of vesicles was varied and their effect on probability of pore formation (P_{pore}) was determined. At a constant salt concentration ($C=162$ mM), the P_{pore} in GUVs were investigated for $X = 0.60, 0.40, 0.20$ and 0.10 . Fig. 4.23 shows the dependence of P_{pore} (60 s) for $X = 0.60$ (Δ), 0.40 (\square), 0.20 (\diamond) and 0.10 (\circ) at $C = 162$ mM for various σ_c . It is observed that as the value of X decreased from 0.60 to 0.10 the tension required for the similar value of P_{pore} (60 s) is larger. As an example, the value of P_{pore} (60 s) = 0.70 ± 0.07 for $X = 0.60$ at $\sigma_c = 4.5$ mN/m whereas P_{pore} (60 s) = 0.75 ± 0.08 for $X = 0.10$ at $\sigma_c = 7.0$ mN/m. From Fig. 4.23 it is very clear that the probability of pore formation not only depend on tension but also depend on surface charge density. The values of P_{pore} were calculated by observing at least 3 independent experiments and the standard deviation and average values were calculated accordingly.

Now, we discuss the electrostatic effects on the constant electrical tension-induced pore formation in GUVs.

According to equation (4.3), the values of B are obtained $2.27, 1.76, 0.65$ and 0.18 mN/m (which correspond to the best fitting parameter $\omega = 0.49$) for $X = 0.60, 0.40, 0.20$ and

0.10 at 162 mM, respectively. The values of Γ and A_F for the best fitting of σ_c dependent k_p (Fig. 4.24) data at different X are provided in the table 4.18.

The values of Γ are similar to the reported ones [16]. Taking the same values of k_p as used in Fig. 4.24, the experimental data of Fig. 4.23 were fitted using equation (4.6).

The theoretical equation is fitted well to the experimental data as shown in Fig. 4.23.

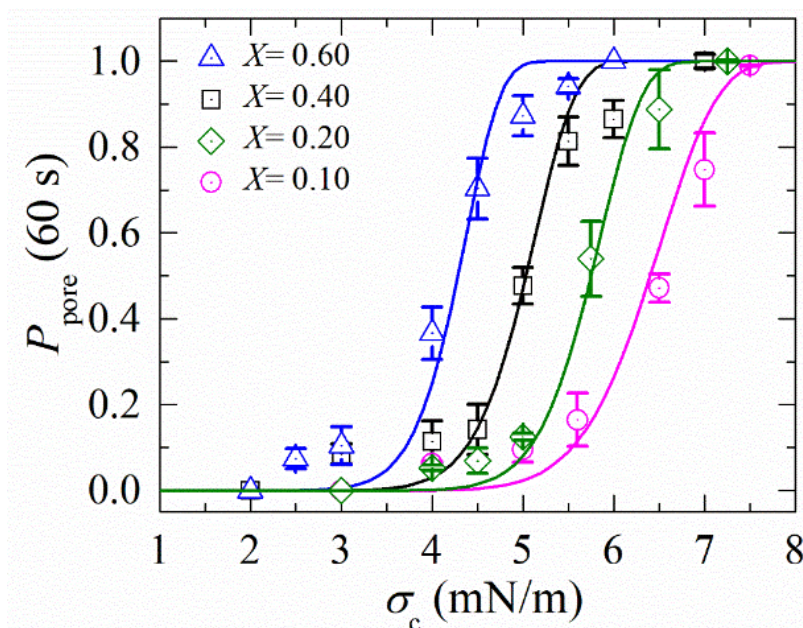


Fig. 4.23 Dependence of P_{pore} (60 s) on σ_c for various surface charge density for $X = 0.60$ (Δ), 0.40 (\square), 0.20 (\diamond) and 0.10 (\circ) at $C = 162$ mM. The average values and standard deviations of the P_{pore} (60 s) are obtained using 3 independent experiments, each with 15-24 GUVs, for each value of σ_c . The solid lines show the best fitted theoretical curves corresponding to equation (4.6) with k_p as used in Fig. 4.24 according to equation (4.5).

4.25 Dependence of Rate Constant on σ_c for Various Surface Charge Density

Fig. 4.24 shows the σ_c dependent k_p values for $X = 0.60$ (Δ), 0.40 (\square), 0.20 (\diamond) and 0.10 (\circ) at $C = 162$ mM. In both of the systems, the value of k_p increases with the increase of σ_c . The value of σ_c dependent k_p values are provided in table. 4.17. The experimental results of σ_c vs k_p is fitted with the theoretical equation (eq.4.5) and obtained the line tension of membranes. It is now interesting to see how line tension changes for electrostatic effects. The values for the best fitting of σ_c dependent k_p data (Fig. 4.24) at different X are provided in the table. 4.18. The solid lines show the best fitted theoretical

curves corresponding to equation (4.5). For various X , at different σ_c the rate constants were obtained. It's because at higher X , pore formation will be observed at lower tension.

Table. 4.17: Surface charge dependent average k_p at various σ_c .

DOPG mole fraction, X	Tension, σ_c (mN/m)	Rate constant, k_p (s^{-1})
0.60	4.5	$(1.3 \pm 0.2) \times 10^{-2}$
	5.5	$(5.7 \pm 0.1) \times 10^{-2}$
	6.0	$(14.02 \pm 0.2) \times 10^{-2}$
0.40	5.0	$(0.9 \pm 0.02) \times 10^{-2}$
	6.0	$(4.0 \pm 0.5) \times 10^{-2}$
	7.0	$(14.10 \pm 0.1) \times 10^{-2}$
0.20	5.75	$(1.1 \pm 0.2) \times 10^{-2}$
	6.5	$(2.7 \pm 0.3) \times 10^{-2}$
	7.25	$(10.1 \pm 0.01) \times 10^{-2}$
0.10	6.5	$(1.1 \pm 0.06) \times 10^{-2}$
	7.0	$(2.3 \pm 0.3) \times 10^{-2}$
	7.5	$(8.0 \pm 0.2) \times 10^{-2}$

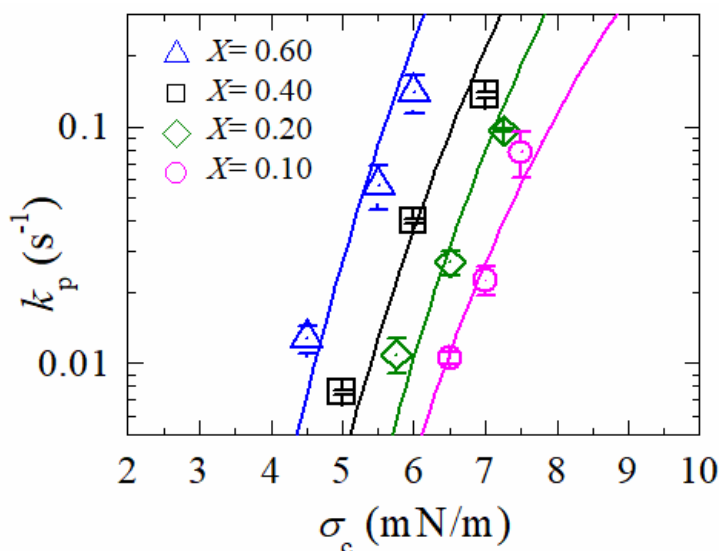


Fig. 4.24 The tension dependent k_p for different surface charge densities. The σ_c dependent k_p for $X = 0.60$ (Δ), 0.40 (\square), 0.20 (\diamond) and 0.10 (\circ) at $C = 162$ mM. Average values and standard deviations of k_p for each tension are determined for 3 independent experiments, each with 18-24 GUVs, for each value of σ_c . The solid lines show the best fitted theoretical curves corresponding to equation (4.5).

Table. 4.18: DOPG mole fraction dependent average Γ .

X	Γ (pN)	A_F (m ² s ⁻¹ J ⁻¹)	R^2
0.60	13.1 ± 0.4	7.5 × 10 ⁷	0.28
0.40	12.1 ± 0.1	8.4 × 10 ⁶	0.36
0.20	11.2 ± 0.3	3.7 × 10 ⁶	0.47
0.10	10.1 ± 0.1	2.1 × 10 ⁵	0.74

4.26 Determination of Critical Tension by Changing Mole Fraction and Its Theoretical Aspects

The effect of anionic lipid on the electroporation in DOPG/DOPC-GUVs was studied at $C = 162$ mM (Debye length, $1/\kappa = 0.304/\sqrt{C}$ [M] = 0.76 nm. Firstly, the electroporation in 40%DOPG/60%DOPC-GUVs was considered. A value of $\sigma_c = 5.0$ mN/m was applied on a ‘single GUV’ for maximum 60 s. As time passed away the observed GUV is abruptly destroyed as shown in Fig. 4.25(a). Before applying the electrical tension (i.e. 0 s in 2a), the GUV was intact and spherical, and had a high contrast between the inside and the outside of GUV in a phase contrast image. The GUV was intact with spherical shape until time = 29.0 s in the presence of σ_c . At time = 30 s, the GUV starts rupturing and at time = 40 s the GUV breaks completely as the structure of GUVs is permanently disappeared. The rupture of GUV is detected when the radius of nano-sized pore rises quickly to infinity [106]. The beginning time of pore specifies the time of pore formation. Pore formation occurs stochastically for several ‘single GUVs’ (the number of examined GUVs $n = 15-24$) at a particular σ_c , which suggests that electroporation occurs at different times though the value of σ_c is constant. If several σ_c are applied to many ‘single GUVs’, the similar stochastic pore formation are also observed in each σ_c . Fig. 4.25(b) and 4.25(c) show the stochastic pore formation of several ($n = 18$) single 40%DOPG/60%DOPC-GUVs and 10%DOPG/90%DOPC-GUVs, respectively at $\sigma_c = 6.5$ mN/m. The bars in the bar chart indicate the GUV label number at a particular time. For the case of 40%DOPG/60%DOPC-GUVs, pore was formed in 16 GUVs out of 18 GUVs (i.e. number of without pore formed GUVs was 2) until the observation time (i.e. 60 s). On the other hand, pore was formed in 10 GUVs

out of 18 GUVs (i.e. number of without pore formed GUVs was 8) until the observation time for the case of 10%DOPG/90%DOPC-GUVs. The cross mark (×) above the bars in the bar chart indicates the GUV label number which was intact until 60 s. These results clearly indicate that the average time of pore formation was much higher for 10%DOPG/90%DOPC-GUVs compared to 40%DOPG/60%DOPC-GUVs at $\sigma_c = 6.5$ mN/m. Therefore, the average time for pore formation is changed amongst the varying amounts of X_{DOPG} in the membranes of GUVs at a particular tension. As X is decreased in the membranes, the time for pore formation tends to increase.

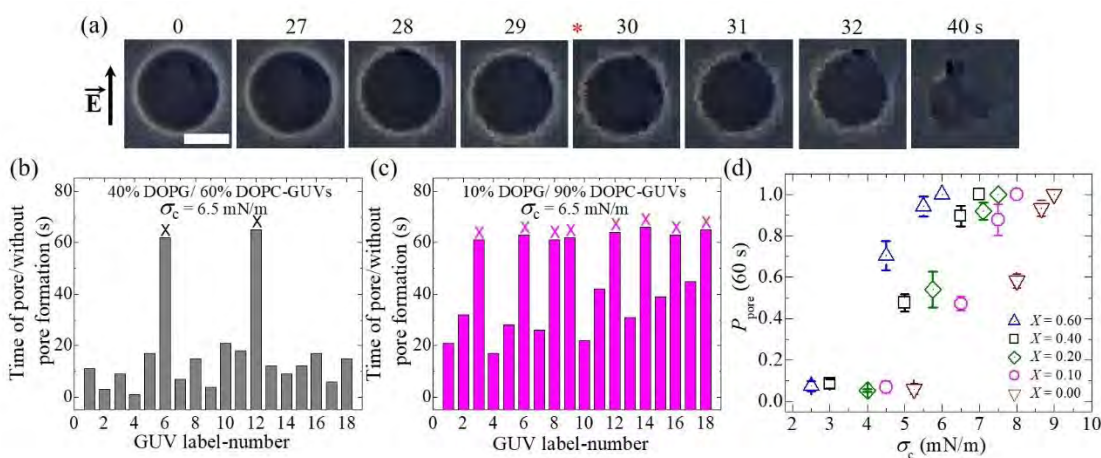


Fig. 4.25 Phase contrast images of pore formation in a ‘single GUV’, the time of pore/without pore formation of several single GUVs and the dependence of probability of pore formation in GUVs on σ_c at different X . (a) Phase contrast images of pore formation of a ‘single 40%DOPG/60%DOPC-GUV’ using $\sigma_c = 5$ mN/m. The field direction is shown with an arrow in the left side. The numbers above in each image show the time in seconds after the application of σ_c due to E . White bar corresponds to the length of $15 \mu\text{m}$. (b) Dependence of $P_{\text{pore}}(60 \text{ s})$ on σ_c for $X = 0.60$ (Δ), 0.40 (\square), 0.20 (\diamond), 0.10 (\circ) and 0.00 (∇) at $C = 162$ mM. The average values and standard deviations of $P_{\text{pore}}(60 \text{ s})$ are obtained using 3 independent experiments, each with 15-24 GUVs, for each value of σ_c .

In order to observe the effect of anionic lipid in electroporation of vesicles the experimental results were investigated quantitatively. The probability of pore formation, $P_{\text{pore}}(t = 60 \text{ s})$, is calculated for several σ_c . $P_{\text{pore}}(t)$ specifies the fraction of GUVs with pores, among all the observed GUVs at a specific time (i.e. 60 s). As for example, if 20

single GUVs are measured at $\sigma_c = 5.0$ mN/m in which 10 GUVs are formed pore within 60 s, $P_{\text{pore}}(t = 60 \text{ s}) = 10/20 = 0.5$. Fig. 4.25(d) and table. 4.19 Show the dependence of $P_{\text{pore}}(60 \text{ s})$ with σ_c for $X = 0.40$ (\square). Consequently, the value of $P_{\text{pore}}(60 \text{ s})$ increases with the increase of σ_c for $X = 0.40$ (\square). It is to be eminent that the critical tension of electroporation in GUVs, σ_c^{crit} , is defined as the least tension needed to obtain $P_{\text{pore}}(60 \text{ s}) = 1.0$. For the case of $X = 0.40$, we get $\sigma_c^{\text{crit}} = 7.0$ mN/m.

Table. 4.19: The dependence of P_{pore} on σ_c using $X = 0.40$.

DOPG mole fraction, X	Tension, σ_c (mN/m)	$P_{\text{pore}}(60\text{s})$
0.40	2	0
	3	0.09 ± 0.02
	5	0.48 ± 0.04
	6.5	0.90 ± 0.05
	7	1

In order to obtain the values of critical tension at various other X such as 0.60, 0.20, 0.10 and 0.0 as shown in Fig. 4.26(b), the $P_{\text{pore}}(60 \text{ s})$ was investigated. It is perceived that as the value of X rises from 0 to 0.60, the σ_c^{crit} for $P_{\text{pore}}(60 \text{ s}) = 1.0$ is reduced. These results show that the mechanical strength of membranes significantly drops with the rise of anionic lipid in the membranes of GUVs. As for example, the value of $\sigma_c^{\text{crit}} = 9.0$ mN/m for $X = 0$ whereas $\sigma_c^{\text{crit}} = 6.0$ mN/m for $X = 0.60$. From the bar chart presented in Fig. 4.26(a) and table. 4.14 of X dependent σ_c^{crit} , it is evident that σ_c^{crit} declines with the increase of X . Then it was normalized that the value of σ_c^{crit} with respect to the critical tension needed to the form rupture in neutral membrane, σ_c^{N} (where $\sigma_c^{\text{N}} = 9.0$ mN/m). The X dependent $\sigma_c^{\text{crit}} / \sigma_c^{\text{N}}$ is shown in Fig. 4.26 (b) and table. 4.20.

Table. 4.20: The critical tensions for various surface charge density

DOPG mole fraction, X	Critical tension, σ_c^{crit} (mN/m)
0	9.0 ± 0.3
0.10	8.5 ± 0.4
0.20	7.25 ± 0.2
0.40	7.0 ± 0.4
0.60	6.0 ± 0.3

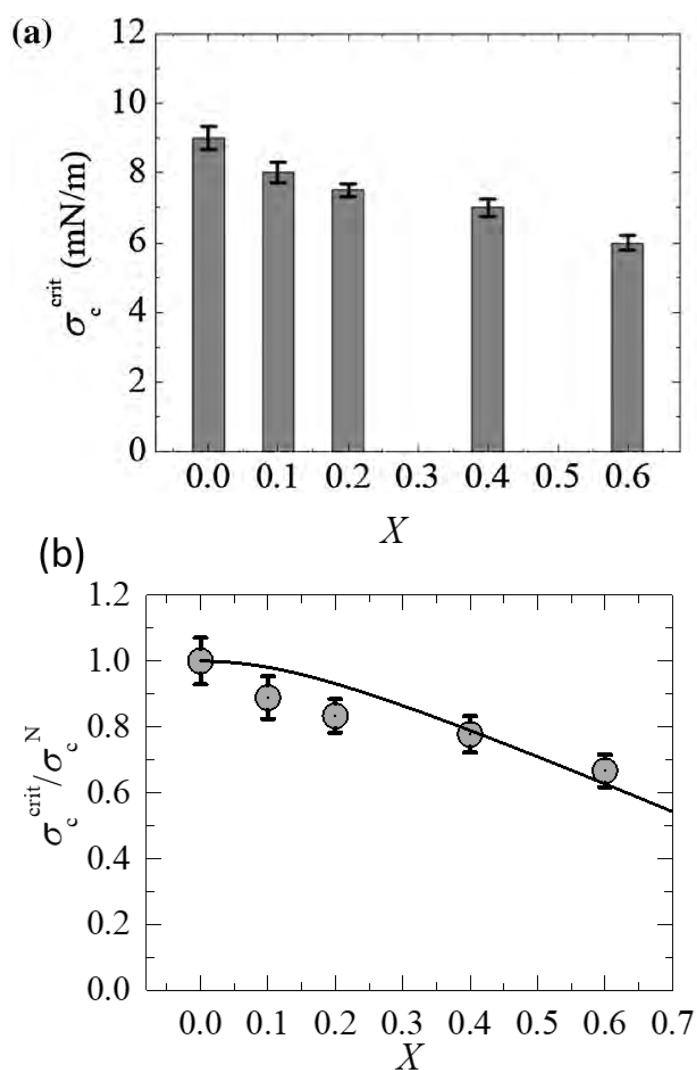


Fig. 4.26 The X dependence (a) bar chart of the critical tension of electroporation and (b) the normalized critical tension of electroporation in GUVs. The solid red line of (b) shows the best fitting theoretical curve of equation (4.12) to the experimental data.

4.27 Theoretical Aspect of Critical Tension

To evaluate the effective tension due to anionic charge in the membranes of GUVs, we calculate the free energy of electrostatic interactions of the monolayer of a bilayer from Gouy-Chapman theory [107]. The free energy of electrostatic interactions due to double electric layer is considered as follows [108-109].

$$g^{\text{el}} = 2k_{\text{B}}TX \left[\frac{1-q}{p} + \ln(p+q) \right] \quad (4.7)$$

where $p = 2\pi\lambda_{\text{B}}X/\kappa A$ and $q = \sqrt{1+p^2}$, Bjerrum length in water $\lambda_{\text{B}} = e^2/4\pi k_{\text{B}}T\epsilon_0\epsilon_{\text{W}}$ = 0.716 nm at 25 °C, ϵ_{W} (= 78.3) is the relative dielectric constant of water, and ϵ_0 (= $8.854 \times 10^{-12} \text{ F}\cdot\text{m}^{-1}$) is the permittivity of free space, k_{B} is the Boltzmann constant, T is absolute temperature, the cross sectional area (A) of DOPG (or DOPC) lipid is $72.5 \text{ \AA}^2/\text{molecule}$ [109]. According to Gouy-Chapman-Stern electrostatic theory, surface charge is set by the fraction of anionic lipid in the membranes and the extent of ion-lipid binding [110]. The effective anionic lipid fraction after binding can be described by the Langmuir-type equilibrium as follows [111-112]:

$$X^{\text{eff}} = K \frac{X}{1 + BC \exp(-e\psi_{\text{surf}}/k_{\text{B}}T)} \quad (4.8)$$

where K is a fitting parameter, B is a first-order binding constant between the anionic membrane and the ions in electrolyte solution and the exponential function accounts for the accumulation of cations at the interface due to electrostatic attraction. The surface potential of the charged membranes, ψ_{surf} , can be estimated theoretically at 25 °C using the Graham equation as follows [111]:

$$\begin{aligned} \psi_{\text{surf}} &= \frac{2k_{\text{B}}T}{e} \sinh^{-1} \left(\frac{\Omega}{\sqrt{8\epsilon_{\text{W}}\epsilon_0 k_{\text{B}}T}} \right) \\ &= 51.4 \sinh^{-1} \left(\frac{\Omega}{0.117\sqrt{C}} \right) [\text{mV}] \end{aligned} \quad (4.9)$$

The surface charge density in the membranes of vesicles is defined as $\Omega = eX/A$ where e is the electronic charge and hence the value of ψ_{surf} depends on the value of X . The charge density given by anionic lipid assuming that the acidic lipid is equally distributed

between the outer and inner monolayer of the GUVs regardless of X . The effective electrostatic tension in the membranes can be expressed as follows.

$$\sigma_c^{\text{el}} = -\frac{dg^{\text{el}}}{dA} = 2 \frac{2k_B T X^{\text{eff}}}{A} \left(\frac{q-1}{p} \right) \quad (4.10)$$

Where the factor of 2 accounts for the two monolayers of bilayer. The critical tension for the rupture of anionic vesicles can be expressed as follows.

$$\sigma_c^{\text{crit}} = \sigma_c^{\text{N}} - \sigma_c^{\text{el}} = \sigma_c^{\text{N}} - \frac{4k_B T X^{\text{eff}}}{A} \left(\frac{q-1}{p} \right) \quad (4.11)$$

After normalization the equation (4.11) can be written as follows.

$$\sigma_c^{\text{crit}} / \sigma_c^{\text{N}} = 1 - \frac{4k_B T X^{\text{eff}}}{\sigma_c^{\text{N}} A} \left(\frac{q-1}{p} \right) \quad (4.12)$$

Where σ_c^{N} is the critical tension required to the formation of rupture in neutral membrane (i.e. DOPC-GUVs).

We have fitted the theoretical equation (4.12) to the experimental data on the X dependent $\sigma_c^{\text{crit}} / \sigma_c^{\text{N}}$ (Fig. 4.26b). The theoretical equation (solid line) is fitted well to the experimental data. The best fit was evaluated from the value of the coefficient of determination, R^2 , which was 0.70. From the fitting curve, we obtain the binding constant of $B = 0.75 \text{ M}^{-1}$ for $\text{PG}^-:\text{Na}^+$ using $K = 0.35$. Recently, the critical tension has been obtained by measuring the area compressibility moduli of membranes using the micropipette aspiration technique [110]. In this investigation, the GUVs were prepared by a mixture of anionic lipid phosphatidylglycerol (POPG) and neutral lipid phosphatidylcholine (POPC) in the potassium chloride (KCl) (moderate ion-lipid binding) and tetramethylammonium chloride (TMA) (low ion-lipid binding) solutions. The critical tension varied from 7.1 ± 1.6 to 2.3 ± 0.9 mN/m for the inclusion of anionic lipid fraction from 0.04 to 0.4 in POPG/POPC-GUVs at KCl buffer. Similarly, the critical tension varied from 7.2 ± 1.0 to 1.7 ± 0.7 mN/m for the inclusion of anionic lipid fraction from 0.04 to 0.3 in POPG/POPC-GUVs at TMA buffer. The values of B for $\text{PG}^-:\text{K}^+$ and $\text{PG}^-:\text{TMA}^+$ were reported 0.80 and 0.40 M^{-1} , respectively [113]. In our investigation, the value of B is obtained 0.75 M^{-1} where NaCl in PIPES buffer is used. In the literature, the value of B is reported (0.0–1.1) M^{-1} although B is sensitive to salt

concentration [112-114]. Therefore, the estimated value of B in this investigation is supported to the reported ones.

It is well reported that the ions of NaCl in colloidal systems shield the surface charges of membrane. Such ions bind the anionic surface of membrane lipids. The higher the anionic lipid in membranes, the stronger the electrostatic effects in the system [112,115]. Again, as the surface charge density in membrane increases the repulsive force between the lipid molecules also increases and hence increase the electrostatic effects [112,115]. These statements support our investigations that as the anionic lipid in the membranes increases the probability of electroporation increases. Therefore, the results presented in Fig. 4.26 indicate that anionic charge in the membranes plays an important role for the destabilization of vesicles. Recent report on mechanical tension-induced pore formation in GUVs indicated that lower tension induced faster rate constant of pore formation in the membranes of GUVs as the electrostatic interaction effects increased [116]. This result suggests that the critical tension for the formation of pores increased with the increase of anionic lipid in membranes. The above discussions support our investigations.

The probability of electroporation can be explained based on the classical theory of pore formation in which the free energy of a prepore and can be expressed as follows [16,110].

$$U(r, \sigma_c, B_{EL}) = 2\pi \Gamma r - \pi r^2 (\sigma_c + B_{EL}) \quad (4.13)$$

Where, Γ is the line energy per unit length of a prepore, r is the radius of a prepore. This was discussed before in section 4.10 and the equations 4.2 but this is where B_{EL} comes for the anionic lipid in the membranes and is defined as follows [115].

$$B_{EL}(X) \approx \left\{ 4\Omega \left[\frac{1-q}{p} + \ln(p+q) \right] \frac{k_B T}{e} - \frac{\Omega^2}{\epsilon_w \epsilon_0} \omega^2 \frac{h}{2} \right\} \quad (4.14)$$

Where h is the height of a prepore (~ 4 nm), ω is the fitting parameter which is the ratio of the surface charge density on the prepore wall to that of the GUV surface, and it was evaluated 0.49 [16]. From equation (4.13), at the critical radius of a prepore $r_c = \frac{\Gamma}{\sigma_c + B_{EL}}$,

the energy barrier of a prepore free energy $U_b(r, \sigma_c, B_{EL}) = \frac{\pi \Gamma^2}{\sigma_c + B_{EL}}$. According to equation

(4.14), for a fixed value of Γ and σ_c , the value of U_b depends on the value of B_{EL} which is a function of X . Fig. 4.27 shows an example of the prepore free energy profile for various X . As the value of X increases from 0 to 0.6, the value of U_b decreases from 12.8 to 9.8 $k_B T$ and as a result the probability of electroporation increases. Hence, these explanations support our investigations.

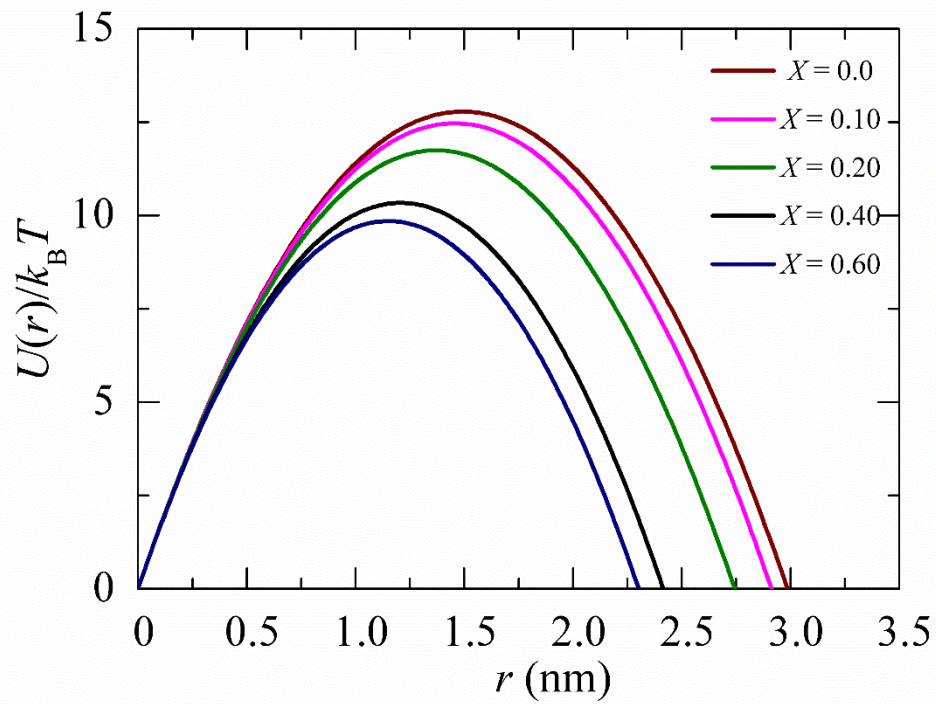


Fig. 4.27 Prepore free energy profile (Eq. 9) for different values of X using $\sigma_c = 7.5$ mN/m and $\Gamma = 11.2$ pN.

CHAPTER: 5

CONCLUSIONS

We have investigated some fundamentals behind the IRE effects under constant electrical tension on biological membranes, using simple DOPG/DOPC phospholipid mixtures with different surface charge densities. In order to investigate the effects of surface charge density, GUVs were prepared using a mixture of DOPG and DOPC with different mole fractions of DOPG (i.e. X) in a buffer containing 150 mM NaCl with 0.10 M sucrose. The values of X in the DOPG/DOPC (60/40), DOPG/DOPC (40/60), DOPG/DOPC (20/80) and DOPG/DOPC (10/90) - GUVs are 0.60, 0.40, 0.20 and 0.10 respectively. The natural swelling method is used to prepare the GUVs. The GUV images were recorded at 25fps using a digital camera connected to the microscope.

The MOSFET based IRE device produces a pulsating DC of frequency 1.1 kHz. At first, the probability of pore formation, P_{pore} ($t=60\text{s}$) was calculated for different surface charge densities by varying the σ_c . At least two independent experiments were completed for each surface charge density. The P_{pore} (60 s) in GUVs was investigated for $X = 0.60, 0.40, 0.20$ and 0.10 at $C = 162$ mM. For $X = 0.60$ the value of P_{pore} (60 s) = 0 at $\sigma_c = 2.0$ mN/m, P_{pore} (60 s) = 0.13 ± 0.093 at $\sigma_c = 3.0$ mN/m, P_{pore} (60 s) = 0.70 ± 0.07 at $\sigma_c = 4.5$ mN/m, P_{pore} (60 s) = 0.82 ± 0.012 at $\sigma_c = 5.5$ mN/m and P_{pore} (60 s) = 1.0 was obtained for various σ_c . Again for $X = 0.40$ the value of P_{pore} (60 s) was 0 at $\sigma_c = 2.0$ mN/m, 0.13 ± 0.03 at $\sigma_c = 4.0$ mN/m, 0.49 ± 0.041 at $\sigma_c = 5.0$ mN/m, 0.87 ± 0.02 at $\sigma_c = 6.0$ mN/m and 1.0 at $\sigma_c = 6.5$ mN/m. The observed value of P_{pore} (60 s) for $X = 0.20$ was 0 for $\sigma_c = 2.0$ mN/m, 0.04 ± 0.003 for $\sigma_c = 3.0$ mN/m, 0.54 ± 0.023 for $\sigma_c = 5.75$ mN/m, 0.80 ± 0.41 for $\sigma_c = 6.5$ mN/m and 1.0 for $\sigma_c = 7.25$ mN/m. Finally the values obtained for of P_{pore} (60 s) for $X = 0.10$ was 0 for $\sigma_c = 3.0$ mN/m, 0.07 ± 0.004 for $\sigma_c = 4.0$ mN/m, 0.13 ± 0.031 $\sigma_c = 5.0$ mN/m, 0.48 ± 0.02 for $\sigma_c = 6.0$ mN/m, 0.75 ± 0.08 for $\sigma_c = 7$ mN/m and 1.0 for $\sigma_c = 7.5$ mN/m. It was observed that as the value of X decreased from 0.60 to 0.10 the tension required for the similar value of P_{pore} (60 s) is greater. As an example, the value of P_{pore} (60 s) = 0.70 ± 0.07 for $X = 0.60$ at $\sigma_c = 4.5$ mN/m whereas P_{pore} (60 s) = 0.75 ± 0.08 for $X = 0.10$ at $\sigma_c = 7.0$ mN/m.

We have also investigated the rate constant of pore formation for different surface charge densities at various values of σ_c . In order to determine the rate constant of pore formation in the membranes of vesicles, firstly the time course of the fraction of intact GUVs without pore formation among all of the examined GUVs, $P_{\text{intact}}(t)$, is determined. It is basically indicating the fraction of GUVs that are still intact after time " t ". The $P_{\text{intact}}(t)$ vs time graph is well fitted by a single-exponential decay function $P_{\text{intact}}(t) = \exp(-k_p t)$. Here, k_p indicates the rate constant for pore formation in the membranes of GUVs and t is the duration of time for applying the electric pulses in GUVs (tension was started at $t = 0$). Next, we investigated the time dependent $P_{\text{intact}}(t)$ for different surface charge densities (i.e. $X = 0.60, 0.40, 0.20$ and 0.10) for a fixed salt concentration (i.e. $C = 162$ mM). The time dependent value of $P_{\text{intact}}(t)$ is fitted with a single exponential decay equation and obtained the values k_p of $1.5 \times 10^{-2} \text{ s}^{-1}$, $4.5 \times 10^{-2} \text{ s}^{-1}$ and $12.02 \times 10^{-2} \text{ s}^{-1}$ for $\sigma_c = 4.5, 5.5$ and 6.0 mN/m, respectively at $C = 162$ mM using $X = 0.60$. Again, the values of k_p were $0.9 \times 10^{-2} \text{ s}^{-1}$, $4.0 \times 10^{-2} \text{ s}^{-1}$ and $14.10 \times 10^{-2} \text{ s}^{-1}$ for $\sigma_c = 5.0, 6.0$ and 7.0 mN/m, respectively at $C = 162$ mM using $X = 0.40$. Using $X = 0.20$ at $C = 162$ mM, the values of k_p were $1.1 \times 10^{-2} \text{ s}^{-1}$, $2.7 \times 10^{-2} \text{ s}^{-1}$ and $10.1 \times 10^{-2} \text{ s}^{-1}$ for $\sigma_c = 5.75, 6.5$ and 7.25 mN/m, respectively. Again, the values of k_p were $1.1 \times 10^{-2} \text{ s}^{-1}$, $2.3 \times 10^{-2} \text{ s}^{-1}$ and $8.0 \times 10^{-2} \text{ s}^{-1}$ for $\sigma_c = 6.5, 7.0$ and 7.5 mN/m, respectively at $C = 162$ mM using $X = 0.10$. The rate constant of pore formation increased with the increase of the surface charge density of membranes.

We have also studied some fundamentals behind the critical tension of IRE in anionic lipid vesicles. Here the effect of DOPG mole fraction, X , on the critical tension of electroporation in GUVs has been studied in sodium chloride containing PIPES buffer. To clearly observe the influence of anionic lipid in electroporation of vesicles the experimental results are analyzed quantitatively. The probability of pore formation, $P_{\text{pore}}(t = 60 \text{ s})$, is calculated for various σ_c . The dependence of $P_{\text{pore}}(60 \text{ s})$ with σ_c for $X = 0.40$ is obtained at $\sigma_c < 3.0$ mN/m, $P_{\text{pore}}(60 \text{ s}) \approx 0$, at $\sigma_c = 3.0$ mN/m, $P_{\text{pore}}(60 \text{ s}) = 0.09 \pm 0.02$, at $\sigma_c = 5.0$ mN/m, $P_{\text{pore}}(60 \text{ s}) = 0.48 \pm 0.04$, at $\sigma_c = 6.5$ mN/m, $P_{\text{pore}}(60 \text{ s}) = 0.90 \pm 0.05$ and at $\sigma_c = 7.0$ mN/m and above, $P_{\text{pore}}(60 \text{ s}) = 1.0$. Therefore, the value of $P_{\text{pore}}(60 \text{ s})$ increases with the increase of σ_c for $X = 0.40$. It is to be noted that the critical tension of electroporation in GUVs, σ_c^{crit} , is defined as the minimum tension required to obtain $P_{\text{pore}}(60 \text{ s}) = 1.0$. For the case of $X = 0.40$, we obtain $\sigma_c^{\text{crit}} = 7.0$ mN/m. The

P_{pore} (60 s) was investigated for other values of X such as 0.60, 0.20, 0.10 and 0.0 and obtained the values of critical tension $\sigma_c^{\text{crit}} = 6.0$ mN/m, $\sigma_c^{\text{crit}} = 7.25$ mN/m, $\sigma_c^{\text{crit}} = 8.5$ mN/m and $\sigma_c^{\text{crit}} = 9.0$ mN/m, respectively. It is observed that as the value of X increases from 0 to 0.60, the σ_c^{crit} for P_{pore} (60 s) = 1.0 is smaller. These results indicate that the mechanical stability of membranes greatly decreases with the increase of anionic lipid in the membranes of GUVs. As for example, the value of $\sigma_c^{\text{crit}} = 9.0$ mN/m for $X = 0$ whereas $\sigma_c^{\text{crit}} = 6.0$ mN/m for $X = 0.60$.

To evaluate the effective tension due to anionic charge in the membranes of GUVs, we calculate the free energy of electrostatic interactions of the monolayer of a bilayer. The higher the anionic lipid in membranes, the stronger the electrostatic effects in the system. Again, as the surface charge density in membrane increases the repulsive force between the lipid molecules also increases and hence increase the electrostatic effects. These statements support our investigations that as the anionic lipid in the membranes increases the probability of electroporation. Therefore, the results presented in this thesis specify that anionic charge or surface charge density in the membranes plays a significant part for the destabilization of vesicles. It has been developed an analytical treatment of the surface charge density on the free energy profile of a prepore in the membranes of vesicles, which explains the experimental results. The theoretical data of free energy profile also well fitted with the experimental results. We have found that the decrease in the free energy barrier of the prepore state due to surface charge density is the main factor causing an increase in the rate constant of pore formation in membranes. These investigations suggest that the mechanical stability is greatly decreased in the presence of anionic lipid membranes. This observation offers an entrancing biophysical description of the phenomenon of electroporation in vesicles together with the insight of biological consequences.

As the plasma membranes consist of 10–20% anionic lipid, the mechanical stability of membranes greatly depends on the amount of anionic lipid in membranes. Due to the presence of such anionic lipids and the charges in aqueous solution, the surface charge density has an important implication for the ablation of tumor and cancer cells using

IRE technique. Again the mechanical stability of membranes is greatly dependent on the surface charge density of membranes. As a result, the surface charge density must be taken into account for any realistic consideration such as for the ablation of tumor and cancer cells using electric field pulses. Because of the existence of such anionic lipid the critical tension has an imperative implication for the ablation of tumor and cancer cells using IRE method. Consequently, the critical tension must be taken into account for any realistic consideration such as for the ablation of tumor and cancer cells using electric field pulses.

REFERENCES

- [1] McLaughlin, S., Murray, D., “Plasma membrane phosphoinositide organization by protein electrostatics,” *Nature*, vol. 438, pp. 605–611, 2005.
- [2] Tamba, Y., Yamazaki, M., “Magainin 2-Induced pore formation in the lipid membranes depends on its concentration in the membrane interface,” *J. Phys. Chem. B*, vol. 113, pp. 4846–4852, 2009.
- [3] Zasloff, M., “Antimicrobial peptides of multicellular organisms,” *Nature*, vol.415, pp. 389–395, 2002.
- [4] Al-Sakere, B., Andre', F., Bernat, C., Connault, E., Opolon, P., Davalos, R. V., Rubinsky, B., “A study of the immunological response to tumor ablation with irreversible electroporation,” *Tech. Can. Res. Treat. (TCRT)* vol. 6, pp. 301-306, 2007.
- [5] Miller, L., Leor, J., Rubinsky, B., “Cancer cells ablation with irreversible electroporation,” *Tech. Can. Res. Treat. (TCRT)* vol.4, pp. 699–705, 2005.
- [6] Rowan, N.J., MacGregor, S.J., Anderson, J.G., Fouracre, R.A., Farish, O., “Pulsed electric field inactivation of diarrhoeagenic *Bacillus cereus* through irreversible electroporation,” *Lett. Appl. Microbiol*, vol.31, pp. 110–114, 2000.
- [7] Teissié, J., Eynard, N., Vernhes, M.C., Bénichou, A., Ganeva, V., Galutzov, B., Cabanes, P.A., “Recent biotechnological developments of electropulsation. A prospective review,” *Bioelectrochemistry*, vol. 55, pp.107–112, 2002.
- [8] Karal, MAS., Yamazaki, M., “Communication: Activation energy of tension-induced pore formation in lipid membranes,” *J Chem Phys*, vol. 143, pp. 81-103, 2015.
- [9] Karal, MAS, Levadnyy, V, Yamazaki M., “Analysis of constant tension-induced rupture of lipid membranes using activation energy,” *Phys Chem Chem Phys*, vol. 18, pp. 13487–13495, 2015.
- [10] Karal, MAS., Ahamed, MK., Rahman, M., Ahmed, M., Shakil, MM., Rabbani, KS., “Effects of electrically-induced constant tension on giant unilamellar vesicles using irreversible electroporation,” *Eur Biophys J*, vol.48, pp. 731–741, 2015(a).

- [11] Ahamed .MK., Karal. MAS., Ahmed. M., Ahammed. S., “Kinetics of irreversible pore formation under constant electrical tension in giant unilamellar vesicles,” *Eur Biophys J*, vol. 100, pp. 371-381, 2020.
- [12] Karal, M.A.S., Ahmed, M., Levadny, V., Belaya, M., Ahamed, M.K., Rahman, M., Shakil, M.M., “Electrostatic interaction effects on the size distribution of self-assembled giant unilamellar vesicles,” *Phys. Rev. E*, vol. 101, pp. 012404, 2015.
- [13] Karal, M.A.S., Islam, M.K., Mahbub, Z.B., “Study of molecular transport through a single nanopore in the membrane of a giant unilamellar vesicle using COMSOL simulation,” *Eur. Biophys. J.* vol. 49, pp. 59–69, 2020 (c).
- [14] Karal, MAS., Alam, JM., Takahashi, T., Levadny V., Yamazaki M., “Stretch-activated pore of the antimicrobial peptide, magainin 2,” *Langmuir*, vol. 31, pp.3391–3401, 2015.
- [15] Karal, M.A.S., Ahamed, M.K., Ahmed, M., Ahamed, S., Mahbub, Z.B., “Location of peptide-induced submicron discontinuities in the membranes of vesicles using image,” *J. J. Fluoresc*, vol.40, pp.735-740, 2020 (d).
- [16] Dev, S.B., Rabussay, D.P., Widera, G., Hofmann, G.A., “Medical applications of electroporation,” *IEEE Trans. Plasma Sci.* vol. 28, pp. 206–223, 2000.
- [17] Tsong, T.Y., “Electroporation of cell membranes,” *Biophys. J.*, vol. 60, pp. 297–306, 1991.
- [18] Akimov, S.A., Volynsky, P.E., Galimzyanov, T.R., Kuzmin, P.I., Pavlov, K.V., Batishchev, O.V., “Pore formation in lipid membrane II: Energy landscape under external stress,” *Sci. Rep.*, vol. 7, pp. 12509, 2017 (a).
- [19] Böckmann, R.A., de Groot, B.L., Kakorin, S., Neumann, E., Grubmüller, H., “Kinetics, statistics, and energetics of lipid membrane electroporation studied by molecular dynamics simulations,” *Biophys. J.*, vol. 95, pp.1837–1850, 2008.
- [20] Levine, Z.A., Vernier, P.T., “Life cycle of an electropore: Field-Dependent and field-independent steps in pore creation and annihilation,” *J. Membrane Biol.*, vol. 236, pp. 27–36, 2010.
- [21] Tarek, M., “Membrane Electroporation: A molecular dynamics simulation,” *Biophys. J.*, vol 88, pp. 4045–4053, 2005.

- [22] Cunill-Semanat, E., Salgado, J., “Spontaneous and stress-induced pore formation in membranes: Theory, experiments and simulations,” *J. Membrane Biol.*, vol. 252, pp. 241–260, 2019.
- [23] Koronkiewicz, S., Kalinowski, S., “Influence of cholesterol on electroporation of bilayer lipid membranes: chronopotentiometric studies,” *Biochim. Biophys. Acta (BBA) – Biomembranes*, vol. 1661, pp. 196–203, 2004.
- [24] Dimova, R., Bezlyepkina, N., Jordö, M.D., Knorr, R.L., Riske, K.A., Staykova, M., Vlahovska, P.M., Yamamoto, T., Yang, P., Lipowsky, R., “Vesicles in electric fields: Some novel aspects of membrane behavior,” *Soft Matter*, vol. 5, 3201, 2009.
- [25] Dimova, R., Riske, K.A., Aranda, S., Bezlyepkina, N., Knorr, R.L., Lipowsky, R., “Giant vesicles in electric fields,” *Soft Matter*, vol. 3, pp. 817, 2017.
- [26] Akimov, S.A., Volynsky, P.E., Galimzyanov, T.R., Kuzmin, P.I., Pavlov, K.V., Batishchev, O.V., “Pore formation in lipid membrane I: Continuous reversible trajectory from intact bilayer through hydrophobic defect to transversal pore,” *Sci. Rep.*, vol. 7, pp. 12152, 2017.
- [27] Levadny, V., Tsuboi, T., Belaya, M., Yamazaki, M., “Rate constant of tension-induced pore formation in lipid membranes,” *Langmuir*, vol. 29, 3848–3852, 2013.
- [28] Karatekin, E., Sandre, O., Guitouni, H., Borghi, N., Puech, P.-H., Brochard-Wyart, F., “Cascades of transient pores in giant vesicles: line tension and transport,” *Biophys. J.*, vol. 84, 1734–1749, 2003.
- [29] Sandre, O., Moreaux, L., Brochard-Wyart, F., “Dynamics of transient pores in stretched vesicles,” *Proc. Natl. Acad. Sci. U.S.A.*, vol. 96, pp. 10591–10596, 1999.
- [30] Evans, E., Heinrich, V., Ludwig, F., Rawicz, W., “Dynamic tension spectroscopy and strength of biomembranes,” *Biophys. J.*, vol. 85, pp. 2342–2350, 2003.
- [31] Evans, E., Smith, B.A., “Kinetics of hole nucleation in biomembrane rupture,” *New J. Phys.*, vol. 13, pp. 095010.
- [32] Rawicz, W., Olbrich, K.C., McIntosh, T., Needham, D., Evans, E., “Effect of chain length and unsaturation on elasticity of lipid bilayers,” *Biophys. J.*, vol. 79, pp. 328–339, 2020.

- [33] Shoemaker, S.D., Vanderlick, T.K., "Intramembrane electrostatic interactions destabilize lipid vesicles," *Biophys. J.*, vol. 83, pp. 2007–2014, 2002.
- [34] Yeagle, P., "The structure of biological membranes," *CRC Press, BocaRaton, FL*, 1992.
- [35] Cevc, G., "Membrane electrostatics," *Biochim Biophys Acta (BBA) - Reviews on Biomembranes*, vol. 1031, pp. 311–382, 1990.
- [36] Langner, M., Kubica, K., "The electrostatics of lipid surfaces," *Chem Phys Lipids.*, vol. 101, pp.3–35, 1999.
- [37] Diederich, A., Bähr, G., Winterhalter, M., "Influence of surface charges on the rupture of black lipid membranes," *Phys Rev E.*, vol. 58, pp. 4883–4889, 1998.
- [38] Meier W, Graff A, Diederich A, Winterhalter M., "Stabilization of planar lipid membranes: A stratified layer approach," *Phys Chem Chem Phys.*, vol. 2, pp.4559–4562, 2002.
- [39] Miklavčič, D.; Mali, B.; Kos, B.; Heller, R.; Serša, G. "Electrochemotherapy: From the Drawing Board into Medical Practice," *Bio. Med. Eng. OnLine*, vol.13 (1), pp. 29. 2014.
- [40] Mir, L. M., Orłowski, S., Belehradek, J. & Paoletti, C. "Electrochemotherapy potentiation of antitumour effect of bleomycin by local electric pulses," *Eur J. Can. Clin. Onc.*, vol. 27, pp. 68–72, 1991.
- [41] Dimova, R., Riske, K.A., Aranda, S., Bezlyepkina, N., Knorr, R.L., Lipkowsky, R. "Giant vesicles in electric fields," *Soft Matter*, vol. 3, pp 828–836, 2008.
- [42] Rubinsky, B., Onik, G. & Mikus, P. "Irreversible Electroporation: A New Ablation Modality — Clinical Implications", *Tech. Can. Res. Treat. (TCRT)*, vol. 6, pp 37–48 2007.
- [43] Al-Sakere, B., Andre', F., Bernat, C., Connault, E., Opolon, P. "Tumor ablation with irreversible electroporation," *Public Library of Science One (PLoS one)*, vol. 2(11), pp. 1135, 2007.
- [44] Riske, A., Dimova, R. "Electro deformation and poration of giant vesicles viewed with high temporal resolution" *Biophysical Journal*, vol. 88, pp 1143-1155, 2005.
- [45] Shoemaker, S.D., Vanderlick, T.K., "Intramembrane electrostatic interactions destabilize lipid vesicles," *Biophys. J.*, vol. 83, pp 2007–2014, 2002.

- [46] Karal, M. A. S., Levadnyy, V., Tsuboi, T., Belaya, M. & Yamazaki, M., "Electrostatic interaction effects on tension-induced pore formation in lipid membranes", *Physical Review*, vol. 92, pp 012404, 2015.
- [47] Rubinsky, B. "Irreversible Electroporation in Medicine," *Tech. Can. Res. Treat. (TCRT)*. vol. 6(4), pp 255-260, 2007.
- [48] Doevenspeck, H. "Influencing cells and cell walls by electrostatic impulses", *Fleishwirtschaft*. vol.13, pp 986-987, 1961.
- [49] Singer, S. J., Nicolson, Garth L. "The fluid mosaic model of the structure of cell membranes," *Membranes and Viruses in Immunopathology; Day, SB, Good, RA, Eds*, pp 7-47, 1972.
- [50] Lee, E. W., Wong, D., Prikhodko, S. V. " Electron microscopic demonstration and evaluation of irreversible electroporation-induced nanopores on hepatocyte membranes," *J. Vasc. Interv. Radiol.*, vol. 23, pp 107–113, 2012.
- [51] Almeida, P. F. F., W. L. C. Vaz., "Lateral diffusion in membranes. In Structure and Dynamics of Membranes: From Cells to Vesicles. R. Lipowski and E. Sackmann, editors," *Elsevier*, pp 305–357, 1995.
- [52] Han R, Campbell KP. "Dysferlin and Muscle Membrane Repair," *Curr Opin Cell Biol.*, vol. 19, pp 409–416, 2007.
- [53] Walde, P., Cosentino, K., Engel, H. & Stano, P. "Giant Vesicles: Preparations and Applications," *Chem Bio Chem.*, vol. 11, pp 848–865, 2010.
- [54] Kagan, B. L., Selsted, M. E., Ganz, T. & Lehrer, R. I. "Antimicrobial Defensin Peptides Form Voltage-Dependent Ion-Permeable Channels in Planar Lipid Bilayer Membranes," *Proc. Natl. Acad. Sci. U. S. A.*, vol. 87, pp 210–214, 1990.
- [55] Karal, M. A. S., Rahman, M., Ahamed, M. K., Shibly, S. U. A., Ahmed, M., Shakil, M. "Low cost non-electromechanical technique for the purification of giant unilamellar vesicles," *Eur Biophys J.*, vol.48, pp 349–359, 2019.
- [56] Vitkova, V., Mader, M. & Podgorski, T. "Deformation of vesicles flowing through capillaries," *Europhys. Lett. EPL.*, vol. 68, pp 398–404, 2004.
- [57] Tanaka, T. & Yamazaki, M. "Membrane Fusion of Giant Unilamellar Vesicles of Neutral Phospholipid Membranes Induced by La^{3+} ," *Langmuir*, vol. 20, pp 5160–5164 2004.

- [58] Pilwat, G., Zimmermann, U.: "Determination of intracellular conductivity from electrical breakdown measurements," *Biochimica et Biophysica Acta (BBA)*, vol. 820, pp 305–314, 1985.
- [59] Ivorra, A.: Annex A – "Bioimpedance monitoring for physicians: an overview, Contributions to the measurement of electrical impedance for living tissue ischemia injury monitoring," PhD Thesis. Universitat Politècnica de Catalunya, Barcelona, pp 131–176, 2005.
- [60] Grimnes, S., Martinsen, O.G. "Bioimpedance and Bioelectricity Basics," *Academic Press, London* (2000).
- [61] Toepfl, S., Mathys, A., Heinz, V. & Knorr, D. "Review: Potential of High Hydrostatic Pressure and Pulsed Electric Fields for Energy Efficient and Environmentally Friendly Food Processing," *Food Reviews International*, vol. 22, pp 405–423, 2006.
- [62] Schoenbach, K. H., Peterkin, F. E., Alden, R. W. & Beebe, S. J. "The effect of pulsed electric fields on biological cells: experiments and applications", *IEEE Trans. Plasma Sci.* 25, 284–292 (1997).
- [63] Kinosita, K.J., Tsong, T.Y., "Formation and resealing of pores of controlled sizes in human erythrocyte membrane," *Nature*, vol. 268, pp 438–441, 1977.
- [64] Joshi, R. P. and K. H. Schoenbach. "Mechanism for membrane electroporation irreversibility under high-intensity, ultrashort electrical pulse conditions", *Phys. Rev. E.* vol. 66, pp 052901, 2002.
- [65] Vernhes, M. C., Benichou, A., Pernin, P., Cabanes, P. A. & Teissié, J. "Elimination of free-living amoebae in fresh water with pulsed electric fields," *Water Research.* vol. 36, pp 3429–3438, 2002.
- [66] Lee, R. C. and M. S. Kolodney. "Electrical injury mechanisms: Electrical breakdown of cell membranes," *Plast Reconstr Surg.* Vol 80(5), pp 672-9, 1987.
- [67] Lee, R. C. "Cell Injury by Electric Forces," *Annals of the New York Academy of Sciences*, vol. 1066, pp 85-91, 2005.
- [68] Evans, E., Heinrich, V., Ludwig, F. & Rawicz, W. "Dynamic Tension Spectroscopy and Strength of Biomembranes," *Biophys. J.*, vol. 85, pp 2342–2350, 2003.
- [69] Belov, S. V. "Effects of high-frequency current parameters on tissue coagulation," *Biomed. Eng. J.*, vol. 12, pp 209-211, 1978.
- [70] Kotic, A., Janacek, K., "Membrane transport," *Akademia, Praha*, 1977.

- [71] Nagarajan, R., "Molecular packing parameter and surfactant self-assembly: the neglected role of the surfactant tail," *Langmuir*, vol. 18, pp 31-38, 2002.
- [72] Huang, L., Somasundaran, P., "Theoretical model and phase behavior for binary surfactant mixtures," *Langmuir*, vol. 1, pp 6683-81997, 1997.
- [73] Antonietti, M., Förster, S., "Vesicles and Liposomes: A Self-Assembly Principle Beyond Lipids," *Advanced Materials*, vol. 15, pp 1323-33, 2003.
- [74] De Gennes, P. G., Taupin, C., "Microemulsions and the flexibility of oil/water interfaces," *J. Phys. Chem.*, vol. 6, pp 2294-304, 1982.
- [75] Zhelev, D. V., Needham, D., "Tension-stabilized pores in giant vesicles: determination of pore size and pore line tension," *Biochimica et Biophysica Acta*, vol. 1147, pp. 89-104, 1993.
- [76] Prats, M., Teissié, J. & Tocanne, J.-F., "Lateral proton conduction at lipid-water interfaces and its implications for the chemiosmotic-coupling hypothesis," *Nature*, vol. 322, pp. 756-758, 1986.
- [77] Mashaghi, A., Partovi-Azar, P., Jadidi, T., Nafari, N., Esfarjani, K., Maass, P., Tabar, M. R. R., Bakker, H. J., Bonn, M., "Interfacial Water Facilitates Energy Transfer by Inducing Extended Vibrations in Membrane Lipids," *J. Phys. Chem. B.*, vol. 116, pp. 6455-6460, 2012.
- [78] Shen, S., Henry, A., Tong, J., Zheng, R. & Chen, G., "Polyethylene nanofibres with very high thermal conductivities," *Nat. Nanotechnol.*, vol. 5, pp. 251-255, 2010.
- [79] Israelachvili, J.N., D.J. Mitchell, and B.W. Ninham, "Theory of self-assembly of hydrocarbon amphiphiles into micelles and bilayers," *J. Chem. Soc. Faraday Trans. 2*, vol. 72, pp. 1525-1568, 1976.
- [80] Clarke, R. J., and C. Luöpfert., "Influence of anions and cations on the dipole potential of phosphatidylcholine vesicles: a basis for the Hofmeister effect," *Biophys. J.*, vol.76, pp 2614-2624, 1999.
- [81] Cevc, G., "Membrane electrostatics," *Biochim. Biophys. Acta.*, vol. 1031, pp 311-382, 1990.
- [82] Karal, M. A. S., Ahamed, K., Rahman., Ahmed, M. Shakil, Md. M., Rabbani, K.S, "Effects of Electrically-Induced Constant Tension on Giant Unilamellar Vesicles Using Irreversible Electroporation," *Biophys. J.*, vol. 48(8), pp 731-741,2019.
- [83] Fricke, H., "A mathematical treatment of the electric conductivity and capacity of disperse systems. II. The capacity of a suspension of conducting spheroids surrounded by

a non-conducting membrane for a current of low frequency," *Physical Review*, vol. 26, 1925.

[84] Fricke, H. and S, Morse., "The electric capacity of tumors of the breast," *The Journal of Cancer Research*, vol. 10(3), pp 340-376, 1925.

[85] Ivorra, A., Annex, A., "Bioimpedance monitoring for physicians: an overview, Contributions to the measurement of electrical impedance for living tissue ischemia injury monitoring," *Universitat Politècnica de Catalunya, Barcelona*, vol.4, pp 131–176, 2005.

[86] Grimnes, S., Martinsen, O.G., "Bioimpedance and Bioelectricity Basics," *Academic Press, London*, 2000.

[87] Chizmadzhev, Y.A., Zarnitsin, V.G., Weaver, J.C., Potts, R.O., "Mechanism of electro-induced ionic species transport through a multilamellar lipid system," *Biophys. J.*, vol. 68, pp 749–756, 1997.

[88] Larsen, J., Hatzakis, N. S., and Stamou, D. (2011). "Observation of inhomogeneity in the lipid composition of individual nanoscale liposomes," *J. Am. Chem. Soc.*, vol. 133, pp 10685–10687, 2011.

[89] Walde, P., Cosentino, K., Engel, H. & Stano, P., "Giant Vesicles: Preparations and Applications," *Chem Bio Chem.*, vol. 11, pp 848–865, 2010.

[90] Yamashita, Y., Masum, S. Md., Tanaka, T. & Yamazaki, M., "Shape Changes of Giant Unilamellar Vesicles of Phosphatidylcholine Induced by a De Novo Designed Peptide Interacting with Their Membrane Interface," *Langmuir*, vol. 18, pp 9638–9641, 2002.

[91] Tanaka, T., Tamba, Y., Masum, S. M., Yamashita, Y. & Yamazaki, M., "La³⁺ and Gd³⁺ induce shape change of giant unilamellar vesicles of phosphatidylcholine," *Biochimica et Biophysica Acta (BBA) – Biomembranes*, vol. 1564, pp 173–182, 2002.

[92] Sugiura, S., Kuroiwa, T., Kagota, T., Nakajima, M., Sato, S., Mukataka, S., Walde, P., Ichikawa, S., "Novel method for obtaining homogeneous giant vesicles from a monodisperse water-in-oil emulsion prepared with a microfluidic device," *Langmuir*, vol. 24, pp 4581–4588, 2008.

[93] Angelova, M. I. & Dimitrov, D. S., "Liposome electroformation," *Faraday Discuss. Chem. Soc.*, vol. 81, pp 303, 1986.

- [94] Karal, M. A. S., Alam, J. Md., Takahashi, T., Levadny, V. & Yamazaki, M., "Stretch-Activated Pore of the Antimicrobial Peptide, Magainin 2," *Langmuir*, vol. 31, pp 3391–3401, 2015
- [95] Islam, Md. Z., Alam, J. Md., Tamba, Y., Karal, M. A. S. & Yamazaki, M., "The single GUV method for revealing the functions of antimicrobial, pore-forming toxin, and cell-penetrating peptides or proteins," *Phys. Chem. Chem. Phys.*, vol. 16, pp 15752–15767, 2014.
- [96] Hasan, M., Karal, M. A. S., Levadnyy, V. & Yamazaki, M., "Mechanism of Initial Stage of Pore Formation Induced by Antimicrobial Peptide Magainin 2," *Langmuir*, vol. 34, pp 3349–3362, 2018.
- [97] Levadny, V., Tsuboi, T., Belaya, M. & Yamazaki, M., "Rate Constant of Tension-Induced Pore Formation in Lipid Membranes," *Langmuir*, vol. 29, pp 3848–3852, 2013
- [98] Tamba, Y., Terashima, H. & Yamazaki, M., "A membrane filtering method for the purification of giant unilamellar vesicles," *Chem. Phys. Lip. J.*, vol. 164, pp 351–358, 201).
- [99] Karal, M. A. S., Levadnyy, V. & Yamazaki, M., "Analysis of constant tension-induced rupture of lipid membranes using activation energy," *Phys. Chem. Chem. Phys.*, vol. 18, pp 13487–13495, 2016.
- [100] Karal, M. A. S., Levadnyy, V., Tsuboi, T., Belaya, M. & Yamazaki, M., "Electrostatic interaction effects on tension-induced pore formation in lipid membranes", *Physical Review*, vol. 92, pp 012404, 2015.
- [101] Karal, M. A. S. & Yamazaki, M., "Communication: Activation energy of tension-induced pore formation in lipid membranes," *Chem. Phys. J.*, vol. 143, pp 081103, 2015.
- [102] Baumgart, T., Hess, S. T. & Webb, W. W., "Imaging coexisting fluid domains in biomembrane models coupling curvature and line tension," *Nature*, vol. 425, pp 821–824, 2003.
- [103] Yamashita, Y., Oka, M., Tanaka, T. & Yamazaki, M., "A new method for the preparation of giant liposomes in high salt concentrations and growth of protein microcrystals in them," *Biochimica et Biophysica Acta (BBA) – Biomembranes*, vol. 1561, pp 129–134, 2002.

- [104] Karal, M. A. S., Rahman, M., Ahamed, M. K., Shibly, S. U. A., Ahmed, M., & Shakil, M. M., "Low-cost non-electromechanical technique for the purification of giant unilamellar vesicles," *Eur. Biophys. J.*, vol. 48, pp. 349–359, 2019.
- [105] Ahamed, M.K., Karal, M.A.S., Ahmed, M., Ahammed, S., 2020. "Kinetics of irreversible pore formation under constant electrical tension in giant unilamellar vesicles," *Eur. Biophys. J.*, 2020.
- [106] Hänggi, P., Talkner, P., Borkovec, M., "Reaction-rate theory: fifty years after Kramers," *Rev. Mod. Phys.*, vol. 62, pp 251–341, 1990.
- [107] Taupin, C., Dvolaitzky, M., Sauterey, C., "Osmotic pressure-induced pores in phospholipid vesicles," *Biochemistry*, vol. 14, pp 4771–4775, 1975.
- [108] Levadny, V., Tsuboi, T., Belaya, M., Yamazaki, M., 2013. "Rate constant of tension-induced pore formation in lipid membranes," *Langmuir*, vol. 29, pp 3848–3852, 2013.
- [109] Wohlert, J., den Otter, W.K., Edholm, O., Briels, W.J., 2006. "Free energy of a trans-membrane pore calculated from atomistic molecular dynamics simulations," *J. Chem. Phys.*, vol. 124, pp 154905, 2006.
- [110] Taupin, C., Dvolaitzky, M., Sauterey, C., "Osmotic pressure-induced pores in phospholipid vesicles," *Biochemistry*, vol. 14, pp 4771–4775, 1975.
- [111] Tieleman, D.P., Leontiadou, H., Mark, A.E., Marrink, S.-J., "Simulation of pore formation in lipid bilayers by mechanical stress and electric fields," *J. Am. Chem. Soc.*, vol. 125, pp 6382–6383, 2003.
- [112] Levadny, V., Tsuboi, T., Belaya, M., Yamazaki, M., 2013. "Rate constant of tension-induced pore formation in lipid membranes," *Langmuir*, vol. 29, pp 3848–3852, 2013.
- [113] Karal, M. A. S., Alam, J. Md., Takahashi, T., Levadny, V. & Yamazaki, M., "Stretch-Activated Pore of the Antimicrobial Peptide, Magainin 2," *Langmuir*, vol. 31, pp 3391–3401, 2015
- [114] Shoemaker, S.D., Vanderlick, T.K., "Intramembrane electrostatic interactions destabilize lipid vesicles," *Biophys. J.*, vol. 83, pp 2007–2014, 2002.

[115] Nagle, J.F., Tristram-Nagle, S., “Structure of lipid bilayers,” *Biochim. Biophys. Acta (BBA) - Reviews on Biomembranes*, vol. 1469, pp 159–195, 2000.

[116] Betterton, M.D., Brenner, M.P., “Electrostatic edge instability of lipid membranes,” *Phys. Rev. Lett.*, vol. 82, pp 1598–1601, 1999.

APPENDIX

Peer reviewed journal:

1. Electrostatic effects on the electrical tension-induced irreversible pore formation in giant unilamellar vesicles

Authors: Mohammad Abu Sayem Karal, *Urbi Shyamolima Orchi*, Md.Towhiduzzaman, Md. Kabir Ahamed, Marzuk Ahmed, Shareef Ahammed, Nadia Akter Mokta, Sabrina Sharmin, Malay Kumar Sarkar (First 3 authors contributed equally)

Journal: Chemistry and Physics of Lipids (Elsevier), Vol. 231, pp. 104935, 2020.

2. An investigation into the critical tension of electroporation in anionic lipid vesicles

Authors: Mohammad Abu Sayem Karal, Md. Kabir Ahamed, *Urbi Shyamolima Orchi*, Md. Towhiduzzaman, Marzuk Ahmed, Shareef Ahammed, Nadia Akter Mokta and Muhammad Samir Ullah

Journal: European Biophysics Journal (Springer Nature), Vol. 50, pp. 99-106, 2021.

Conference Presentations:

1. Urbi Shyamolima Orchi, Md. Towhiduzzaman, Marzuk Ahmed, Md. Kabir Ahamed, Shareef Ahammed and Mohammad Abu Sayem Karal: Intramembrane Electrostatic Effects on the Irreversible Electroporation induced Rate Constant of Pore Formation in the Membranes of Vesicles (*Abstract-PP-131*) *International Conference on Physics, Organised by BPS*, Dhaka, Bangladesh, 05-07 March, 2020.

2. Urbi Shyamolima Orchi, Md. Kabir Ahamed, Md. Towhiduzzaman, Shareef Ahammed, Mohammad Abu Sayem Karal: Pore Formation and Membrane Fusion of Giant Unilamellar Vesicles Using Electrically Induced Constant Tension in the Membrane (*Abstract-pp-48*) *National Conference on Electronics and Informatics, Organized by BES and BAEC*, Dhaka, Bangladesh, December, 2019.

3. Md. Towhiduzzaman, Urbi Shyamolima Orchi, Md. Kabir Ahamed, Marzuk Ahmed, Shareef Ahammed and Mohammad Abu Sayem Karal: Effects of Salt Concentration on the Irreversible Electroporation Induced Pore Formation in the Lipid Membranes of Cell Like Vesicles (*Abstract-pp-111*) *International Conference on Physics, Organised by BPS*, Dhaka, Bangladesh, 05-07 March, 2020.